AN INVESTIGATION ON IWAN MODELS FOR CAPTURING THE AMPLITUDE-DEPENDENT BEHAVIOR OF STRUCTURES WITH BOLTED JOINTS

by

Robert M. Lacayo

A thesis submitted in partial fulfillment of the requirements for the degree of

Master of Science

(Engineering Mechanics)

at the

UNIVERSITY OF WISCONSIN-MADISON

2017

Abstract

This thesis introduces the concepts and the procedures for a method of updating the parameters of an Iwan joint element in a finite element model to fit experimental measurements on the effective natural frequency and damping of the vibrational modes of a structure containing bolted joints. Evidence has shown that the presence of a bolted joint in a structure causes its natural frequencies and modal damping ratios to change in accordance with the amplitude of vibration. Linear models are incapable of reproducing this amplitude-dependence in frequency and damping, while predictive models for joint friction (e.g. the Coulomb model) are too computationally-expensive to use in iterative design updating, so a medium is sought in which the hysteresis of a joint is captured using a single Iwan element. The parameters of an Iwan element are not intuitive and must be deduced using test measurements, but it is difficult to isolate the contribution of each joint from the response of structures containing many joints. As an alternative, Segalman (Tech. Report *SAND2010-4763*, Sandia National Laboratories, 2010) introduced a framework for representing the net nonlinear effect of all joints on the modes of a structure by using modal Iwan models. Previous literature has shown that a modal Iwan model can be tuned to each mode in isolation from others in order to reproduce their change in frequency and damping with amplitude. Although it can accurately simulate the effects of bolted joint nonlinearity on a structure in some cases, it is ultimately limited by its inability to account for modal coupling.

In this thesis, the limitations of modal Iwan approach are explored by demonstrating how modal coupling affects the the amplitude-dependent natural frequency and damping of each mode. In quantifying the importance of modal coupling, it was learned that Segalman's modal

framework for updating works best if joint models are tuned to response measurements where only one mode is approximately dominant. Modal coupling can be better captured using discrete Iwan elements in a finite element model, but traditional techniques for measuring effective modal frequency and damping require dynamic simulations, which are too expensive to compute in an iterative updating routine. A solution was provided by Festjens et al. (*Journal of Sound and Vibration* 333, 2014) whereby the joint is treated as a static subcomponent in an otherwise dynamic global model. After a few modifications to their theory, an efficient quasi-static algorithm was produced for computing amplitude-dependent frequency and damping by loading the finite element model in the shape of one of its modes. This new quasi-static method was then utilized to update a set of Iwan parameters for a beam model containing three bolted joints. Although the model achieved a good fit with experiments, the Iwan model was acknowledged to have limitations of its own with regards to its inability to fit both frequency and damping measurements in other works. Iwan-type model proposed by Mignolet et al. (*Journal of Sound and Vibration* 349, 2015) showed promise in overcoming those limitations, but its amplitude behavior in a transient ring-down response was revealed to be the same as that of the original Iwan model.

Acknowledgments

This work was funded by Sandia National Laboratories. Sandia National Laboratories is a multi-mission laboratory managed and operated by National Technology and Engineering Solutions of Sandia, LLC., a wholly owned subsidiary of Honeywell International, Inc., for the U.S. Department of Energy's National Nuclear Security Administration under contract DE-NA0003525. My gratitude goes out to Rob Kuether, who was my funding supervisor during the latter half of my graduate career as well as my senior in the research group to which I belong.

A special thanks must be given to my advisor, Prof. Matthew Allen, for his preliminary work on the methodology discussed in this thesis, for his suggestions on the direction to take my research, and for his quality reviews of my current and upcoming journal publications. An equal show of thanks is given to Prof. Matthew Brake at Rice University, who was not only my funding supervisor for the first half of my graduate career, but also my mentor during our time at Sandia National Laboratories. The work I completed for the Nonlinear Mechanics and Dynamics (NOMAD) Summer Research Institute that Matthew Brake directed gave me the contextual inspiration I needed to apply the quasi-static method developed in this thesis as a model updating technique. I am aware that these two Matthews highly desired to recruit me as their PhD student, and I hope to make it up to them in some other form in the future.

Thanks is given to Daniel Segalman, Gaël Chevallier's research group, and Marc Mignolet's research group, whose works formed the theoretical foundation of my thesis.

I wish to express my appreciation to all my research colleagues, from Madison and abroad, for fun times to help unwind ourselves from the stress of research.

Finally, I thank my family for their support and for reminding me that life is more than research. Shout out to my bro who just returned from military service abroad, my two sisters who are in their undergraduate studies, and the youngest bro who is an upperclassman in high school. I love you all!

Thesis

This thesis consists of an extended summary (Chapter 1) and the following papers:

Chapter 2	R. M. Lacayo, B. J. Deaner, and M. S. Allen, "A numerical study on the limitations of modal Iwan models for impulsive excitations," *Journal of Sound and Vibration* 390, 2017, pp. 118–140.
Chapter 3	R. M. Lacayo, and M. S. Allen, "Updating structural models containing nonlinear Iwan joints using quasi-static modal analysis," Submitted for international publication, 2017.
Chapter 4	R. M. Lacayo, and M. S. Allen, "A study on the transient behavior of the five-parameter Iwan-type model in ring-up and ring-down simulations," Submitted for international publication, 2017.

The included papers were prepared in collaboration with co-authors. The author of this thesis was responsible for most of the major progress of work, i.e. planning the research, developing and carrying out the numerical implementations and simulations, performing the experiments, and writing the papers. Although the theory and methodology presented in the papers given in Chapters 2 and 3 were developed primarily by the co-authors, the paper in Chapter 4 is almost entirely the author's own work.

Contents

Chapter 1

Extended Summary

1.1 Motivation and Context

Many structures of engineering design are an assembly of smaller components that are connected to each other through bolted joints. Although bolted joints facilitate the construction and integrity of complicated and useful shapes, such as the turbofan jet engine casing shown in Fig. 1.1, they are also known to be sources of energy dissipation and stiffness loss during vibration. Furthermore, the dissipation and stiffness exhibited by a joint has been found to change with amplitude [1, 2]; as larger loads excite a bolted structure to higher vibration levels, the damping of its response tends to increase substantially whereas its natural frequencies can be seen to decrease slightly [3]. Engineers typically neglect this change in stiffness and dissipation due to joints, and they simply model the structure conservatively using linear approximations for the stiffness and damping exerted by the joint (i.e. stiffness and damping are constant). For most applications in design, such conservative estimates are sufficient.

In the aerospace industry, however, conservative designs for aircraft and spacecraft tend to add more weight to the structure than is needed. Engineers must balance the volume of material with the structural stiffness such that applied loads do not exceed the stress limits of the vehicle during operation. Bolted joints are especially crucial for meeting this criterion because they are one of the biggest sources of passive energy dissipation in aerospace structures [4, 5, 6]. Energy dissipation helps to reduce vibration amplitudes, and hence decreases the internal stresses in

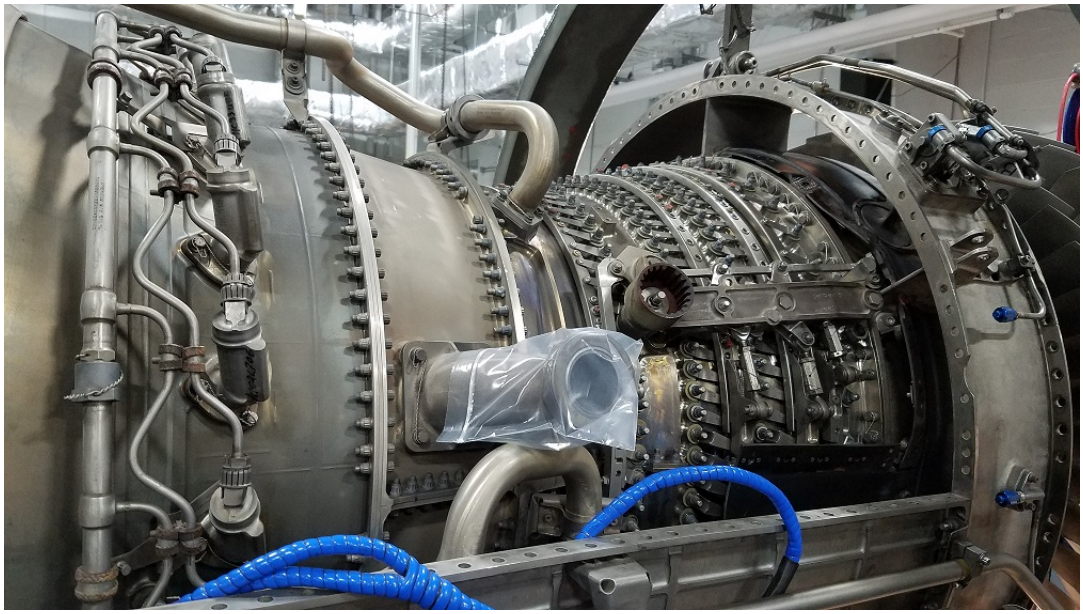

Figure 1.1: *Picture of the exterior of an F-16 turbofan engine. This structure contains hundreds of bolted connections that help to damp out vibration in the engine.*

a frame. If a more accurate estimate of a structure's capacity for energy dissipation can be computed for different levels of environment loading, then engineers can be better informed so as to create more lightweight designs for aircraft and spacecraft.

More lightweight structures lead to better fuel economy. A recent study on twelve different commercial airliners performing intercontinental flights found that, for every 100 kg of mass added to the aircraft, about 2.5 kg more in jet fuel was consumed per hour in flight [7]. In 2015, the total utilization of commercial aircraft by U.S. domestic carriers was 14.3 million hours [8], and the price of jet fuel was an average of $0.512 per kg [9], so an average of $183,000 worth of jet fuel could be saved annually for every kg of mass removed from all aircraft. Considering that the median mass of a commercial airliner is 270,000 kg [7], even half a percent in weight reduction in all aircraft creates a total savings on the order of $250 million annually in jet fuel. Thus there is an economic benefit in the ability to accurately predict the dynamic behavior of structures using models that can account for the change in stiffness and dissipation due to bolted joints.

While simple to state, to actually develop a valid dynamic model for a bolted joint has proven to be one of the grand challenges of the current state-of-the-art in structural dynamics. Part of this difficulty stems from an incomplete understanding of the tribological processes that occur in a joint interface as it undergoes dynamic flexure. The mechanics of interfacing bodies involve a number of phenomena, such as contact, friction, adhesion, and wear, a review of which are given in [10]. All of these processes occur at a length scale that is several orders of magnitude smaller than the length of the structure as a whole. Hence, as pointed out by Berger [11], analysts are faced with the additional challenge of mediating the trade-off in the spatial resolution of the nonlinear degrees of freedom within a joint interface versus the computational effort required to evaluate such a model.

For dynamic models involving bolted joints, analysts typically simplify the underlying physics by assuming that joint behavior is dominated solely by microslip friction [12]. As two mechanically-joined bodies undergo vibration (such as the two plates in Fig. 1.2a), some surface asperities near the edge of the contact area break contact with the opposite surface and undergo slipping. The act of breaking contact results in a slight reduction of the stiffness of the joint, and the friction forces induced during slip dissipate vibrational energy. A joint is said to be in microslip when such localized regions of the interface undergo slip, yet the joint as a whole remains intact due to those asperities that remain stuck closer to the center of the bolt (Fig. 1.2b). As the loading on the structure increases, and vibrational amplitudes increase, the regions of slip also grow and spread towards the center of the bolt (Fig. 1.2c), which further reduces the stiffness and dissipates more energy per cycle of vibration. When the region of slip spreads to the entire interface, the stiffness of the joint becomes compromised, and the two interfacing bodies undergo bulk motion relative to one another. In this state of relative bulk motion, the joint is said to be in macroslip. Joints are designed to maintain their integrity, so the macroslip regime is hardly reached in practice. This thesis is mainly concerned with the modeling of joint microslip, but the reader is directed to [13, 14, 15] for some reviews of

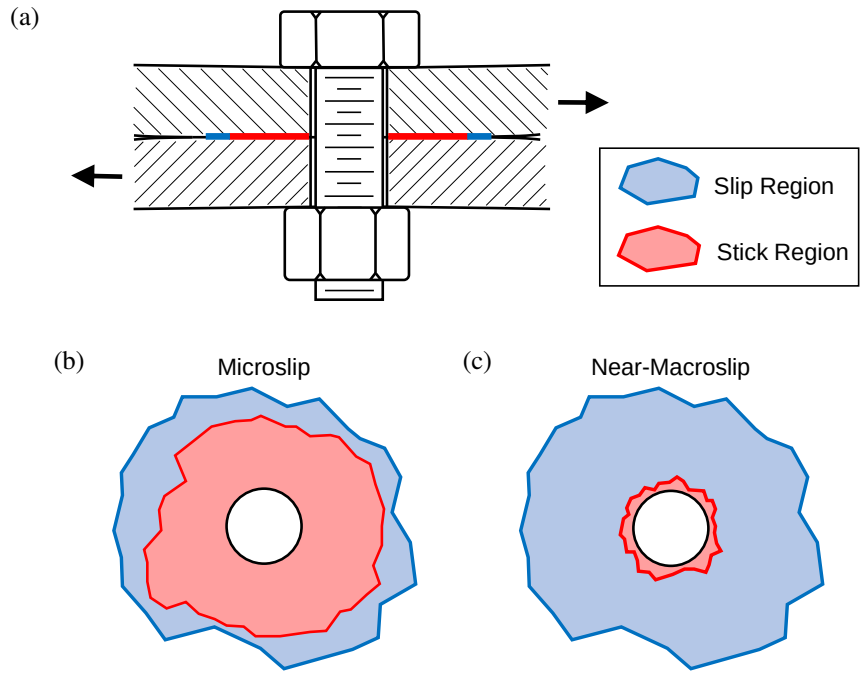

Figure 1.2: *(a) Side view and (b) top view illustrations of the locations of slip regions in a nominal contact area of a bolted lap joint undergoing microslip vibration, and (c) the encroachment of the slip region as the macroslip regime is approached.*

macroslip models.

Over the past few decades, researchers have proposed a number of different approaches for representing microslip friction behavior in a finite element model. One approach in common usage is simply to connect the coincident nodes between two identically-meshed surfaces using Coulomb friction elements [16]. Other works have proposed placing two-dimensional ”zero thickness” [17, 18, 19] or three-dimensional ”thin-layer” [20, 21, 22] continuum elements in between the two interfacing surfaces. Both of these types of elements maintain an elastic material model in the direction normal to the surfaces, but employ a stick-slip formulation in the tangential directions to model local friction behavior. In order to represent microslip friction accurately with these types of approaches, the finite element model typically requires a mesh of elements having far greater density in the region of the joint compared to the rest of the structure [23], as illustrated in Fig. 1.3.

Computationally, high-fidelity models like these may be feasible for simple structures that

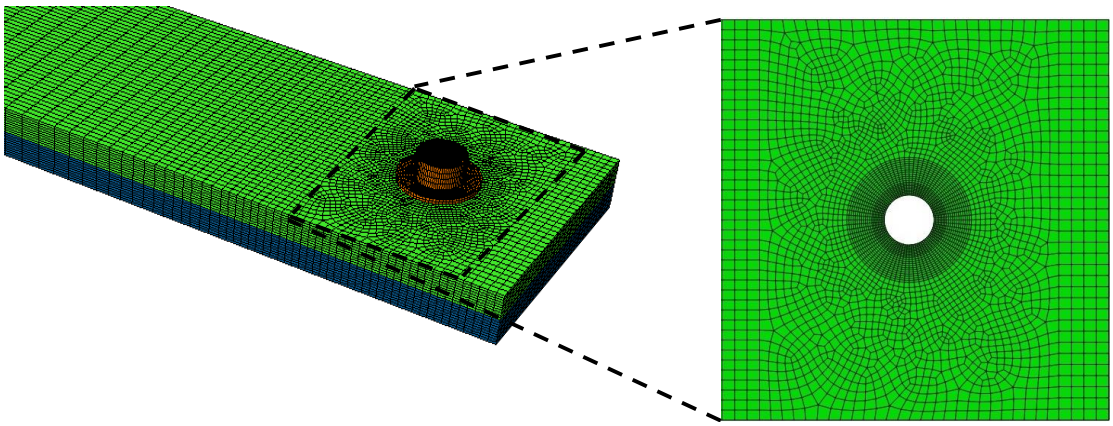

Figure 1.3: *Illustration of a typical mesh required to model Coulomb friction around a bolt hole in a joint model. Mesh density increases dramatically near the hole. The model shown is the same as that studied in [23].*

contain one or a few joints, though some simplifications may be employed to speed up the computational time such as model-order reduction of the linear domain away from the joint (e.g. component mode synthesis [24]) or an assumption of steady-state sinusoidal input (e.g. harmonic balance methods [25, 26]). Using the best of these approaches, the time required to simulate the response to a dynamic loading is still on the order of hours, and this time would stretch to weeks or months for more realistic structures, such as the turbofan jet engine shown in Fig. 1.1, which can contain hundreds of bolted joint interfaces.

To return the computational costs to more reasonable levels, Segalman used the ”whole-joint” modeling approach [27]. In a whole-joint model, the entire patch of contact surrounding the bolt is constrained so that all the nodes on each surface are made dependent on the motion of a representative (virtual) node, as represented by a spider configuration like that shown in Fig. 1.4. The definition of this constraint could connect the surface nodes to the virtual node with rigid bar elements, or a multi-point constraint could be utilized to define the motion of the virtual node as an average of the motion of the surface nodes. In either case, the degrees of freedom belonging to all nodes in a surface are reduced down to those that describe the bulk translation and rotation of that surface. The representative nodes of the two interfacing surfaces

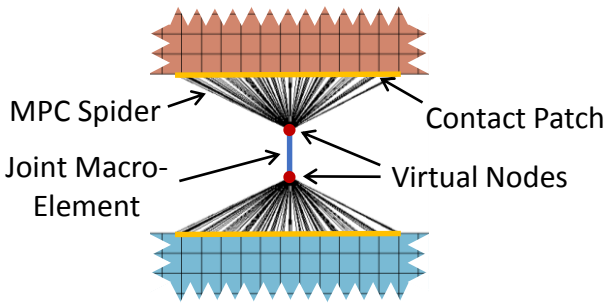

Figure 1.4: *Illustration of an exploded view of a joint spider configuration in a finite element model.*

would then be tied to each end of a macro-element that internally reproduces the microslip behavior of many elastoplastic elements (e.g. Iwan models [28]) or otherwise duplicates the constitutive hysteresis of the joint during vibration (e.g. Bouc-Wen models [29]). In such manner, the behavior of the entire joint is described by one or a few macro-elements oriented in the different coordinate directions. This approach is much more computationally manageable than one that incorporates hundreds of friction elements in each of hundreds of joints.

Despite their computational efficiency, whole-joint models do have some drawbacks. There are presently very few empirical studies that could guide an analyst to choose the parameters that would best represent any particular type of joint. Unlike the Coulomb model of friction (which has a small number of well-understood parameters may be inferred based on properties such as surface roughness, material and bolt pressure), a whole-joint model has more parameters that are less intuitive and may have additional dependencies on the joint configuration. Such dependencies may include the total area of contact, the joint geometry, the type of fastener used to bolt the joint, among others, all of which will be different from joint to joint. Thus, even if the same type of macro-element is used to represent a joint, a unique set of parameters must be deduced for every joint based on experimental data collected from the structure. Even then, there is no guarantee that the contribution of a single joint can be isolated from the data, which further inhibits the development of a valid nonlinear structural model.

Ultimately, the key interest of this thesis is to understand how all of the joints in a structure

affect the natural frequency and damping of each of its modes of vibration, and the extent to which joint nonlinearity couples those modes. An intrinsic property of all structures is that they have a ”preference” to vibrate in one or a superposition of certain shapes of deflection, which are called modes. For example, some mode shapes for beam-like structures include axial extension, twisting, and bending. Each mode shape vibrates in accordance to a simple waveform whose phase changes at a certain speed, referred to as it natural frequency, and whose amplitude decays at a rate defined by its damping ratio. Since each shape is fundamentally different, they each flex the joints in a structure to a different extent. Hence, when a structure vibrates in a the shape of one of its modes, the joints dissipate energy and lose stiffness in a manner that is unique to that mode. When the structure is excited to higher response amplitudes, the loss in stiffness and increase in energy dissipation can be observed experimentally as a decrease in the natural frequency and increase in the damping ratio, respectively, for that mode. Both the natural frequency and the damping can be retrieved for each mode using well-established experimental practices and signal processing techniques, which are reviewed in the subsequent chapters of this thesis.

To model the amplitude-dependence observed in each mode, Segalman again proposed to distribute such nonlinearities spatially over the entire structure through its vibrational modes [30]. The idea behind this approach is to characterize the amplitude-dependent nonlinearity of each mode by fitting a nonlinear, single-mass oscillator system to each modal signal in the measured response [30]. Each modal oscillator is independent from others (i.e. the modes are uncoupled), and the nonlinearity of each mode is accounted for using an Iwan model. As will be explained in the upcoming chapters, an Iwan model is a set of a large number of Jenkins elements (a spring in series with a Coulomb friction element) arranged in parallel. Each spring has the same stiffness, but the sliders have different slip force thresholds, and these thresholds can be defined in a manner that resembles joint hysteresis. Using his four-parameter formulation [31], Segalman derived analytical expressions for the effective stiffness

and energy dissipated by an Iwan model, both of which vary as power-law functions with the amplitude of oscillation. Work by Deaner et al. [32] later used these analytical expressions to help fit a modal four-parameter Iwan model to amplitude-dependent frequency and damping measurements taken from the modes of a test structure.

The versatility of these modal Iwan models was demonstrated by Deaner and other subsequent works [33, 34] where they were used to model a structure whose response consisted of multiple modes. As part of the fitting procedure, the measured response was first filtered into its component modal signals, from which the change in frequency and damping with the amplitude of modal signal could be extracted. After tuning the modal Iwan model for each mode, these works then assume that the physical response, $\mathbf{u}$, of the structure could be predicted using a linear combination of the responses, q_r, simulated with the nonlinear oscillator pertaining to each mode. That is, the principle of linear superposition of modes,

$$\mathbf{u} = \sum_r \boldsymbol{\varphi}_r q_r, \tag{1.1}$$

was assumed to hold, where $\boldsymbol{\varphi}_r$ is the shape vector for mode r. This assumption presumes that the response measured of each mode in experiment is not influenced by other modes, and the results of the author's work given in Chapter 2 quantifies the extent to which this assumption is violated for some simple structures.

1.2 Thesis Contributions

The contributions of this thesis are the following:

- This work explores the limitations of Segalman's modal Iwan approach, showing how modal coupling affects the amplitude-dependent frequency and damping of each mode and quantifying its importance.

- This work proposes and validates a quasi-static approach that can be used to simulate

a computational model containing discrete Iwan elements with such efficiency that iterative model updating becomes practical. The quasi-static approach is built upon the modal Iwan framework, so it is critical to understand the limitations and merits of the modal Iwan model in order to use the quasi-static approach properly.

- This thesis also investigates whether the five-parameter Iwan-type model developed by Mignolet et al. [35], can provide additional flexibility to realize increased damping from a joint for a given frequency shift.

Each of these points are treated separately in the upcoming chapters. The chapters in themselves are verbatim reproductions of standalone journal articles, so their connection to one another is not readily apparent. This section serves to tie those papers together and summarize their key contributions.

1.2.1 The Limitations of Modal Iwan Models

Chapter 2 uses a numerical truth model containing physical Iwan joint elements to show that the effects of coupling between modes can dramatically change how the damping and frequency of each mode vary with amplitude. Since joints act in the physical domain, their effective stiffness and energy dissipation are both functions of the physical response $\mathbf{u}$, or, equivalently, a linear combination of the modal responses, q_r, per Eq. (1.1). When the structure vibrates in the shape of a single mode, the amplitude of all other modes in the response can be considered negligible, so it becomes appropriate to use this response to tune a modal Iwan model pertaining to the mode in question. When more than one mode is dominant, the sum of their contributions in the response increases the amplitude of deflection that the physical joint experiences, and this has direct effect on the stiffness and dissipation it exerts.

Figure 1.5 illustrates the ramifications associated with the inclusion of more than one dominant mode in the response. When the response $\mathbf{u}$ only contains a signal from one mode (the

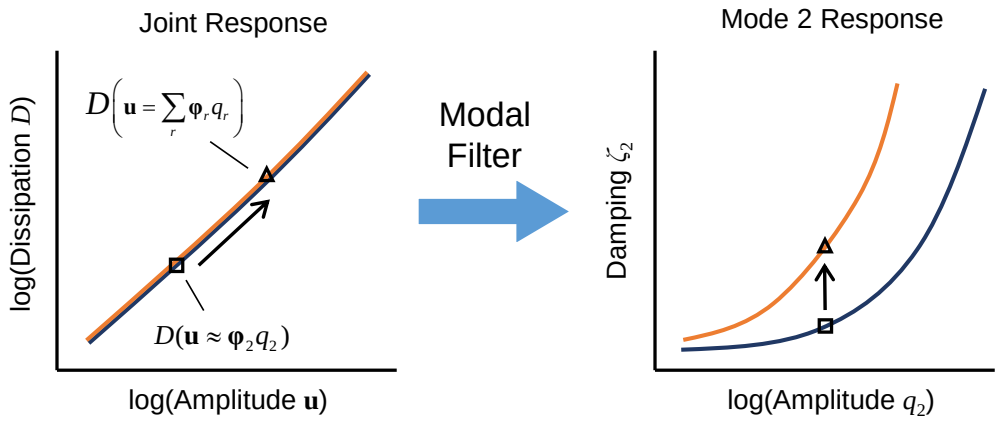

Figure 1.5: *Hypothetical plots of (left) the energy dissipated in a joint versus the amplitude of joint deflection and (right) the damping versus amplitude of a single mode isolated from the response signal. A comparison is made in damping for the case that one mode is dominant in the response (dark blue) and the case that multiple modes are dominant (light orange).*

second mode for example), the energy dissipated by the Iwan joint exhibits a power-law relationship with the amplitude of the response, which has a certain observable effect on the damping of mode 2 (given by the dark blue curve in Fig. 1.5). A modal Iwan model is fitted to this single-mode data. When more modes are used to represent the response, $\mathbf{u}$, the amplitude at a given joint will generally increase. Hence the dissipation that the joint exerts also increases, as illustrated by the shift from the square marker to the triangle marker in Fig. 1.5. Although the amplitude of $\mathbf{u}$ has increased, the amplitude of the mode 2 signal remains the same. The observed effect is that the damping of the mode 2 signal appears to increase at the same amplitude, so the relationship between damping and amplitude in mode 2 follows a different path than that predicted by the modal Iwan model. A similar consequence occurs for the natural frequency of mode 2, except that the frequency curve is lower than would be predicted by the modal Iwan model because the joint stiffness decreases with increasing amplitude. These hypothetical effects are clearly illustrated for actual systems in Chapter 2.

In the end, Chapter 2 shows that modal Iwan models will only produce a reasonable estimate of a structure's response if one mode is approximately dominant near all joints, and it

presents a means of checking that assumption. Unfortunately, the literature has not yet produced a modal model that can account for coupling between modes in an intuitive manner. However, the idea that one can tune a joint model to match the experimental amplitude-change in the natural frequency and damping of the modes is useful. Without this concept, one would have to check infinitely-many responses at infinitely-many points in time to verify that a model is accurate. The framework for model updating presented in Chapter 2 reduces the problem down to a realization of amplitude-dependent modal behavior.

1.2.2 Joint Model Updating Using Quasi-Static Modal Analysis

Chapter 3 expands on the concepts for model updating used in Chapter 2 by presenting a highly efficient method for computing the effective frequency and damping of each mode of a finite element model containing discrete joint elements. The current techniques for extracting the frequency and damping from a model are based on signal processing of the simulated response, similar to that of experiments. Both the signal processing techniques and dynamic simulations are prohibitively expensive to compute, which devalues their use in a practical model updating routine. As explained in Chapter 3, the problem of computational expense in dynamic simulations was overcome by treating the joint as a quasi-static subcomponent in an otherwise linear, dynamic global model. The groundwork for this solution was laid out in a paper by Festjens et al. [36], and, after a few modifications to their theory, a fast and efficient computational method was developed for extracting the amplitude-dependent modal properties from a finite element model. The new method, which the author terms "quasi-static modal analysis" (QSMA), estimates the effective modal natural frequency and damping from a single, static deflection in response to a monotonically-increasing load distributed over the entire structure in the shape of one of its modes. Masing's rules are then applied to the force-deflection relationship to quantify the amount of energy dissipated and stiffness lost in the all joints when the structure vibrates in the mode of interest. More details on the theory and

application of QSMA are given in Chapter 3.

The method of QSMA dramatically reduces the computational effort because the change in the natural frequency and damping of each mode with modal amplitude can be completely determined from a single set of quasi-static, monotonic loading cases. This is in stark contrast to a dynamic simulation, where the free-response history must be computed until its amplitude decays to the smallest level of interest. Furthermore, if Segalman's four-parameter Iwan elements are used to represent the joints, then Chapter 3 shows that the frequency and damping versus amplitude curves produced from QSMA are essentially the same as those obtained using signal processing on the simulated dynamic response. Thus the method of QSMA is demonstrated to be both fast and accurate in computing the amplitude-dependent modal properties of a finite element model containing Iwan elements, and this result makes QSMA ideal for use in a model updating routine.

The final section of Chapter 3 documents how QSMA was used in a Monte Carlo analysis to help deduce the parameters of several Iwan joint elements in a beam model with a lap joint. Measurements on a test article of this beam structure show that its bending modes not only exhibit amplitude-dependence in their natural frequency and damping, but the effects of modal coupling described in Chapter 2 can also be observed when the beam is struck with a hammer impact at different locations. In the Monte Carlo analysis, 100,000 permutations of Iwan element parameters were generated randomly within a plausible parameter space. For each permutation, the frequency and damping curves produced from QSMA for those bending modes were compared with those produced from measurements where the appropriate bending mode was the most dominant signal in the response. Such a selective comparison is consistent because the method of QSMA simulates the response for when the beam model is loaded in the shape of a single mode. Accordingly, after selecting a set of parameters for each of the discrete Iwan joints that produces the lowest error in both frequency and damping among the most important modes, the joint model was validated by simulating the dynamic response of

the beam for an impact that produces modal coupling. The simulated response reproduced much of the modal coupling observed in the test.

1.2.3 Investigations on the Five-Parameter Iwan-Type Model

One of the uncertainties that can arise from the use of Iwan elements in a joint model is its ability or inability to fit both the change in natural frequency and the change in the damping of a mode with amplitude. Although the author was fortunate in that the model he developed for Chapter 3 seemed capable of matching both properties from measurements, it has been found in other works that one or the other could be fitted when using the four-parameter Iwan element [35, 37]. This phenomenon was studied by Mignolet et al. [35], who found that the Iwan model has a coupled relationship between its effective stiffness and the energy it dissipates per cycle of vibration. In an effort to weaken this coupling, Mignolet allowed the friction sliders in a four-parameter Iwan element to exhibit stiction behavior. That is, in the moment that these sliders begin to slip, their coefficient of friction is instantly reduced from the static threshold down to a kinetic constant while in slip, whereas these coefficients are the same in the original four-parameter model. Mignolet assigned a fifth parameter to the model in order to control the amount of decrease in the kinetic friction coefficient. By following a similar derivation as done by Segalman, Mignolet was able to formulate analytical expressions for the effective stiffness and energy dissipated by his new five-parameter "Iwan-type" model for steady-state cyclic loading. Using these equations, he then showed that the parameters of the Iwan-type model could be tuned to fit both the measured stiffness and dissipation of a lap joint whereas Segalman's Iwan model could only fit one or the other.

Given that the five-parameter Iwan-type model is based on the original Iwan model, it seemed possible that it could be used with quasi-static modal analysis in order to fit this model to transient free-response measurements. However, Mignolet never developed a computational element for his Iwan-type model that could be used in a transient simulation, and consequently

never studied the repercussions that stiction could have in a ring-down response. The constitutive formulation that Mignolet presents for his Iwan-type model shows several fundamental differences from the four-parameter model, so there was concern about whether or not Masing's rules would hold well for his model in QSMA. These problems are addressed in Chapter 4.

In Chapter 4, an algorithm for a computational element embodying Mignolet's five-parameter Iwan-type model is presented. The element is based on the Segalman's original formulation for the discretized Iwan element, but it contains one more state variable to account for the stiction behavior. The Iwan-type element was then studied to understand how it behaves in various loading and unloading scenarios. Ultimately, it was found that its effective stiffness and dissipation has a complicated dependence on its past displacement history, particularly the largest displacement it has experienced. Even though Mignolet's derivations showed that the model could be used to decouple the stiffness from the dissipation, the study presented in Chapter 4 shows that this advantage only applies if the Iwan-type element was monotonically-loaded up to some steady-state displacement amplitude. When the vibration drops below this amplitude level, as in a transient free-response, the stiffness and dissipation both revert to the same power-law behavior as that of Segalman's four-parameter Iwan model. In the end, it seems that the five-parameter Iwan-type element holds no advantage over the four-parameter Iwan model in a transient ring-down response, so the benefit of its use does not outweigh the significantly increased complexity that the five-parameter model introduces.

1.2.4 Concluding Remarks

This thesis investigates the accuracy of Iwan models that have been updated to capture the amplitude-dependent frequency and damping of structures with bolted joints. Research is underway to try to predict the parameters of whole-joints from first principles (e.g. to quantify the joint's stiffness and damping), but progress so far shows that predictive modeling is still

a ways off. Until these challenges are addressed, the best approach to model structures with joints will continue to be to update a computational model against response measurements. This thesis presents a collection of methods that now make model updating practical. Through an understanding of modal Iwan models and their conditions for modal dominance, a quasi-static method was then developed that exploits the same mode-dominant condition. By combining the quasi-static method with the amplitude-dependent modal analysis techniques used for modal Iwan models, a new algorithm for model updating was developed that can capture nonlinear modal coupling for structures with bolted joints.

Chapter 2

A Numerical Study on the Limitations of Modal Iwan Models for Impulsive Excitations

Robert M. Lacayo, Brandon J. Deaner, Matthew S. Allen

2.1 Introduction

Mechanical joints are known to be a source of considerable energy dissipation in built-up structures [1, 4]. The presence of a joint causes the damping in the structure to show amplitude-dependent behavior [27]. That is, the apparent damping in the structure tends to increase as the excitation force increases. For years, analysts have modeled amplitude-dependent damping by tuning linear equations of motion for particular levels of excitation. In realistic settings, this method can give erroneous results because the excitations from the environment induce structural responses that cover a spectrum of amplitude levels in a short time frame. A better model is one that can account for the change in damping with amplitude.

One way to account for the change in damping is simply to represent the joint as a local nonlinearity in an otherwise linear finite element model of the structure. Ideally, the joint model would be predictive, describing the friction contact in detail and capturing deformations near the interface due to the clamping load [11, 26, 25]. Prior work has shown that, at small amplitudes, the edges of the contact begin to slide relative to one another even though most of the joint remains intact [10, 38]. This phenomenon is called microslip. In the microslip regime the stiffness of the joint decreases only slightly, but small slip displacements occur in

localized regions in the contact patch that cause significant energy loss [39]. As the excitation amplitude increases, the small slip regions expand and combine until macroslip occurs, where the stiffness of the joint is compromised and relative motion occurs between the interfacing bodies.

To model microslip-macroslip phenomena in detail is exceedingly expensive, and there is still considerable uncertainty regarding which friction models should be used for a given material interface. One alternative is to replace the contacting interfaces with a lumped, hysteresis model such as an Iwan element [28]. This work uses Segalman's four-parameter Iwan model [31], which is capable of capturing joint behavior over both the microslip and macroslip regimes. Segalman's model was developed as a result of an extensive testing campaign and theoretical studies [2], and was shown to capture the physics that were observed in metal-metal contacts. A brief theoretical treatment of the four-parameter Iwan model is given in Appendix A. The four-parameter Iwan model is not predictive, however, so experiments must be conducted to derive its parameters based on the geometry, clamping force, friction characteristics, and other properties of the joint it represents. For bolted structures containing many joints, this could be a challenging task.

In response to this problem, Segalman proposed an alternative approach, the modal Iwan model, which accounts for the net effect of all the joints on each mode of the structure [30]. In Segalman's formulation, a nonlinear single-degree-of-freedom oscillator is used to represent each modal coordinate independently. The nonlinearity is captured with a four-parameter Iwan model so that each mode can exhibit both microslip and macroslip behavior. Many other researchers have proposed similar approaches, although with very different models for each mode (see for example [40, 41]).

The key assumption made in these formulations is that nonlinear coupling between the linear modes is negligible, so the nonlinear model for each mode depends only on the native modal coordinate. Eriten et al. [41] used a complexification and averaging method to show rigorously

that this assumption holds well if the nonlinearity is weak and that the natural frequencies are neither close nor integer related. Follow-up works by Deaner et al. [32] and Roettgen and Allen [33] demonstrated experimentally that the modal Iwan model can be used to accurately describe the free response of bolted structures in microslip.

When a single mode is selectively excited (by adjusting the spatial distribution of the force or exciting at a frequency near resonance), the coupling between modes will be relatively small. Segalman used a three-degree-of-freedom mass-spring system with a single Iwan joint to show that, when a mode is selectively excited, an appropriately tuned modal Iwan model can reproduce the modal response of that mode exceptionally well [30]. Segalman did not probe the limits of this assumption, however. When a general input is applied, modal coupling may be more important. Festjens, Chevallier, and Dion began to explore this in [42], where they showed a case in which a model with uncoupled modes exhibited considerable error compared with their truth simulation. However, their study used an "Iwan joint" with only three slider elements in parallel, so it was not capable of accurately reproducing microslip behavior. This prompts the question: is modal coupling in realistic structures typically small enough to allow a modal Iwan model to be accurate over a significant range of amplitudes in the microslip regime?

This paper seeks to answer that question, exploring the extent to which a modal Iwan model can reproduce the response of a structure to discrete, impulsive excitations. Two structures are considered, a three-degree-of-freedom spring-mass system and a finite element model of a bolted beam, both of which contain discrete Iwan elements to describe joint behavior. The response of these structures is computed for various types of impulsive excitations, and then the effective natural frequency and damping of each mode is compared to that predicted by an uncoupled modal model. The following section presents an overview of the modal Iwan model, followed by a discussion of how to deduce its parameters based on transient ring-down data. The two structures are then studied, first by selectively exciting the linear modes of each

structure to deduce the parameters of an equivalent modal Iwan model. Then the effective damping and natural frequency of the modal Iwan model are compared against those that are observed when the original finite element models are subjected to impulsive excitations at various points. The results show that the modal framework can be a good approximation in the microslip region, and they highlight the path-dependent nature of the nonlinear joints.

2.2 Theoretical Background

The objectives of this study necessitate a comparison between the response simulated from a modal Iwan model with that of a realistic system that has discrete joints. In this work, the response due to bolted-joint nonlinearity is interpreted on a mode-by-mode basis, including the modal coupling that is observed. The typical effect that bolted joints have on a structure is such that, as the amplitude of excitation increases, the modal damping of the structure increases significantly and the natural frequencies decrease slightly [27]. Therefore, in addition to presenting a theoretical treatment of the modal Iwan model, this section also explains how to measure the instantaneous damping and natural frequency from a free-response signal.

2.2.1 Overview of the Modal Iwan Model

Modal Equations of Motion for Structures with Joints

Consider a finite element model of a structure whose equations of motion are

$$\mathbf{M}\ddot{\mathbf{u}} + \mathbf{C}\dot{\mathbf{u}} + \mathbf{K}_{\infty}\mathbf{u} + \mathbf{F}_{J}(\mathbf{u}) = \mathbf{F}_{\text{ext}}, \tag{2.1}$$

where $\mathbf{M}$, $\mathbf{C}$, and $\mathbf{K}_{\infty}$ are the linear mass, damping and stiffness matrices, respectively, and $\mathbf{u}$, $\dot{\mathbf{u}}$, and $\ddot{\mathbf{u}}$ are the displacement, velocity, and acceleration vectors, respectively. The vector $\mathbf{F}_{\text{ext}}$ refers to all time-dependent external loads, and $\mathbf{F}_{J}$ is the vector of joint forces due to all discrete joint elements. Here it is assumed that the constitutive models for the joint elements

depend only on displacements. A Taylor series expansion about unloaded equilibrium ($\mathbf{u} = \mathbf{0}$) is applied on $\mathbf{F}_J$,

$$\mathbf{F}_J(\mathbf{u}) = \mathbf{F}_J(\mathbf{0}) + \nabla\mathbf{F}_J(\mathbf{0})\mathbf{u} + \mathbf{F}_{\mathrm{NL}}(\mathbf{u}), \tag{2.2}$$

where $\nabla\mathbf{F}_J$ is the matrix of partial derivatives of F_J with respect to each entry in $\mathbf{u}$, and $\mathbf{F}_{\mathrm{NL}}$ is the vector of the higher-order, nonlinear terms in the Taylor series. At unloaded equilibrium, the joint elements do no exert forces on the system (i.e. pre-stress is ignored and so $F_J(\mathbf{0}) = \mathbf{0}$), but the full stiffness of each element remains intact. Therefore, $\nabla\mathbf{F}_J = \mathbf{K}_T$ is the stiffness matrix composed of only the tangent stiffness at equilibrium from each joint element in the system. Equation (2.1) becomes

$$\mathbf{M}\ddot{\mathbf{u}} + \mathbf{C}\dot{\mathbf{u}} + (\mathbf{K}_\infty + \mathbf{K}_T)\mathbf{u} + \mathbf{F}_{\mathrm{NL}}(\mathbf{u}) = \mathbf{F}_{\mathrm{ext}}. \tag{2.3}$$

Physically, $\mathbf{K}_\infty$ represents the stiffness of the structure at large displacement amplitudes, where the effective stiffness of all joint elements is zero (due to macroslip). This is in contrast to the limiting case where the amplitude approaches zero and the tangent stiffness of all discrete joint elements remain intact. A low-amplitude stiffness matrix can be formed as $\mathbf{K}_0 = \mathbf{K}_\infty + \mathbf{K}_T$ to represent an equivalent linear system where all joint elements are replaced with linear springs having the same stiffness as the tangent stiffness of the replaced element.

Using these stiffness matrices, the high-amplitude mode shape matrix $\mathbf{\Phi}_\infty$ and the low-amplitude mode shape matrix $\mathbf{\Phi}_0$ are formed from the set of mass-normalized mode shapes, $\boldsymbol{\varphi}_{\infty r}$ and $\boldsymbol{\varphi}_{0r}$, respectively, computed from the eigenvalue problems

$$\left(\mathbf{K}_\infty - \omega_{\infty r}^2\mathbf{M}\right)\boldsymbol{\varphi}_{\infty r} = \mathbf{0}, \quad \left(\mathbf{K}_0 - \omega_{0r}^2\mathbf{M}\right)\boldsymbol{\varphi}_{0r} = \mathbf{0}, \tag{2.4}$$

where $\omega_{\infty r}$ and ω_{0r} are the slip and stick natural frequencies, respectively. The modal transformation $\mathbf{u} = \mathbf{\Phi}_0\mathbf{q}$ is applied to Eq. (2.3) to establish an equation of motion for each modal

coordinate

$$\ddot{q}_r + 2\zeta_{0r}\omega_{0r}\dot{q}_r + \omega_{0r}^2 q_r + \boldsymbol{\varphi}_{0r}^{\mathrm{T}}\mathbf{F}_{\mathrm{NL}}(\boldsymbol{\Phi}_0\mathbf{q}) = \boldsymbol{\varphi}_{0r}^{\mathrm{T}}\mathbf{F}_{\mathrm{ext}}, \tag{2.5}$$

where q_r, $\dot{q}_r$, and $\ddot{q}_r$ are the modal displacement, velocity, and acceleration coordinates, respectively, governing the rth mass mass-normalized mode shape. Here it is assumed that the modal transformation diagonalizes the linear damping matrix, with ζ_{0r} as the low-amplitude critical damping ratio for the rth mode. The quantity $\boldsymbol{\varphi}_{0r}^{\mathrm{T}}\mathbf{F}_{\mathrm{NL}}$ in Eq. (2.5) is a projection of nonlinear joint forces onto the rth mode, and the joint forces are functions of all modal coordinates.

The Modal Iwan Model

In the modal Iwan model, two simplifying assumptions are made. The first is that the modes are uncoupled. This assumption is clearly reasonable if the response is composed of a single, dominant mode. Otherwise, if the response has multiple significant modes, then [41] shows that these modes will not interact significantly if their natural frequencies are not close or are not harmonics of other modes. With negligible modal coupling, $\boldsymbol{\varphi}_{0r}^{\mathrm{T}}\mathbf{F}_{\mathrm{NL}}$ becomes a function of the modal coordinate q_r of interest only.

The second simplification is that the projection of nonlinear joint forces, $\boldsymbol{\varphi}_{0r}^{\mathrm{T}}\mathbf{F}_{\mathrm{NL}}$, can be replaced with the force from an equivalent four-parameter Iwan element $\hat{F}_I$ (see Appendix A) minus the contribution of the linear, modal tangent stiffness term, $\hat{K}_T q_r$, as from Taylor series expansion. Considering that joints have hysteresis behavior that can be modeled with a collection of sliders, then it is reasonable to approximate the projection of their hysteresis onto the rth mode with a tuned Iwan element. Under these two assumptions, Eq. (2.5) simplifies to

$$\ddot{q}_r + 2\zeta_{0r}\omega_{0r}\dot{q}_r + \omega_{0r}^2 q_r + \hat{F}_I(q_r) - \hat{K}_T q_r = \boldsymbol{\varphi}_{0r}^{\mathrm{T}}\mathbf{F}_{\mathrm{ext}}. \tag{2.6}$$

Note that subtracting $\hat{K}_T$ from the low-amplitude modal stiffness, ω_{0r}^2, yields the high-amplitude

modal stiffness, $\omega_{\infty r}^2$. Equation (2.6) finally reduces to

$$\ddot{q}_r + 2\zeta_{0r}\omega_{0r}\dot{q}_r + \omega_{\infty r}^2 q_r + \hat{F}_I(q_r) = \hat{F}_r, \tag{2.7}$$

where $\hat{F}_r = \boldsymbol{\varphi}_{0r}^{\mathrm{T}}\mathbf{F}_{\mathrm{ext}}$ is the projection of external loads on the rth mode.

Equation (2.7) is the core of the modal Iwan model. In effect, the response of a jointed structure is approximated as a superposition of uncoupled, weakly-nonlinear modal coordinates, each governed by a single-mass oscillator system as shown in Fig. 2.1. The weak nonlinearity in each modal oscillator comes from a four-parameter Iwan element whose parameters $\hat{F}_S$, $\hat{K}_T$, $\hat{\chi}$, and $\hat{\beta}$ are denoted with hats (ˆ) to distinguish them from the parameters of the physical joints that will be used in the models presented in Section 2.3. This modal Iwan element is set in parallel with a linear spring of stiffness $\hat{K}_\infty = \omega_{\infty r}^2$ and dashpot with coefficient $2\zeta_{0r}\omega_{0r}$. The reader is referred to [31] for a rigorous treatment of how to calculate $\hat{F}_I$ for the four-parameter Iwan element.

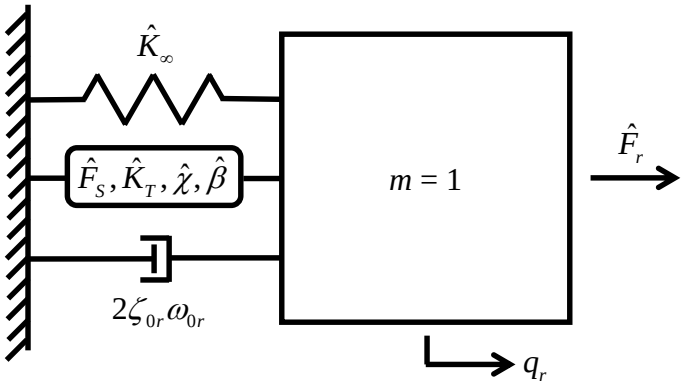

Figure 2.1: *Schematic of a unit mass oscillator representing a modal coordinate in a structure. The oscillator contains a four-parameter Iwan element in parallel with a linear spring and dashpot.*

Analytical Expressions for the Modal Damping and Natural Frequency of a Modal Iwan Model

By assuming harmonic motion, Segalman derived analytical expressions for the Iwan element's instantaneous stiffness and energy dissipated per cycle as functions of the deflection amplitude [31]. Deaner et al. reformulated the equations to apply for a modal Iwan model, expressing them in terms of the modal displacement amplitude, $|q_r|$, and added contributing terms from the linear spring and damper [32]. The analytical expressions for the instantaneous modal stiffness, $\hat{K}_{r,\mathrm{fit}}$, and dissipation, $D_{r,\mathrm{fit}}$, associated with mode r are

$$\hat{K}_{r,\mathrm{fit}} = \hat{K}_\infty + \begin{cases} \hat{K}_T \left(1 - \dfrac{|q_r|^{\hat{\chi}+1}}{\hat{\phi}_{\max}^{\hat{\chi}+1}(\hat{\chi}+1)(\hat{\beta}+1)}\right), & |q_r| < \hat{\phi}_{\max}, \quad \text{microslip}, \\ 0, & |q_r| \geq \hat{\phi}_{\max}, \quad \text{macroslip}, \end{cases} \tag{2.8}$$

$$D_{r,\mathrm{fit}} = 2\pi\zeta_{0r}\omega_{0r}\omega_{r,\mathrm{fit}}|q_r|^2 + \begin{cases} \dfrac{4\hat{R}|q_r|^{\hat{\chi}+3}}{(\hat{\chi}+3)(\hat{\chi}+2)}, & |q_r| < \hat{\phi}_{\max}, \quad \text{microslip}, \\ 4\hat{F}_S|q_r|, & |q_r| \geq \hat{\phi}_{\max}, \quad \text{macroslip}, \end{cases} \tag{2.9}$$

$$\hat{\phi}_{\max} = \frac{\hat{F}_S(1+\hat{\beta})}{\hat{K}_T\left(\hat{\beta} + \frac{\hat{\chi}+1}{\hat{\chi}+2}\right)}, \tag{2.10}$$

$$\hat{R} = \frac{\hat{F}_S(\hat{\chi}+1)}{\hat{\phi}_{\max}^{\hat{\chi}+2}\left(\hat{\beta} + \frac{\hat{\chi}+1}{\hat{\chi}+2}\right)}, \tag{2.11}$$

where $\omega_{r,\mathrm{fit}}$ is the instantaneous natural frequency of the mode, which is obtained from Eq. (2.8) through

$$\omega_{r,\mathrm{fit}} = \sqrt{\hat{K}_{r,\mathrm{fit}}}. \tag{2.12}$$

Following the derivation in Appendix B, a closed form expression for the instantaneous modal damping is found through Eq. (B.5) (with Eq. (B.6)),

$$\zeta_{r,\mathrm{fit}} = \frac{D_{r,\mathrm{fit}}}{2\pi \left(\omega_{r,\mathrm{fit}} |q_r|\right)^2}. \tag{2.13}$$

Equations (2.8) and (2.9) – and (2.12) and (2.13) by extension – have a discontinuity at $\hat{\phi}_{\max}$, the boundary between "modal microslip" and "modal macroslip." This discontinuity is a consequence of the fact that Segalman assumed micro- and macro- slip in order to derive these closed form expressions. In contrast, when the modal model in Eq. (2.7) is integrated it will show a free response that transitions smoothly from macroslip into microslip, as will be shown later (see, for example, Fig. 2.4). Due to the discontinuity, Eq. (2.12) and (2.13) are not used to represent the modal Iwan model in the comparison with the discrete measurements. Instead, the equations are used as tools to identify the six modal Iwan model parameters $[\hat{K}_\infty, \zeta_{0r}, \hat{F}_S, \hat{K}_T, \hat{\chi}, \hat{\beta}]$ that achieve a good fit with the simulated response measurements (hence the subscript "fit"). The method for extracting the instantaneous damping and natural frequency from a free response signal is discussed in Section 2.2.2

2.2.2 Quantifying Damping and Natural Frequency from Response Measurements

Measurements on the transient, free response of a structure can be processed to obtain the instantaneous damping and natural frequency data needed to fit a modal Iwan model to each mode. In practice, the measurements can be obtained either from experiments on a test structure or from truth simulations on a finite element model that uses discrete joint elements (like an Iwan element). This work uses finite element models in order to rule out model uncertainty as a cause for differences between the modal Iwan model and the truth simulations. The technique for processing the measurements is based on the Hilbert transform [43] and is an adaptation of

the method proposed by Sumali and Kellog [44] and further developed in [32, 33].

Hilbert Transform Method for Free-Response Signals

Consider a set of free-response measurements, $\dot{\mathbf{u}}(t)$, obtained from a system after subjecting it to an impact excitation. Here, it is presumed that the velocity is measured, but the procedure is easily adapted for the other states. The measurements are transformed into the modal coordinates of the low-amplitude linearized system, $\dot{\mathbf{q}}(t)$, using a modal filter

$$\dot{\mathbf{q}}(t) = \mathbf{\Phi}_0^{-1}\dot{\mathbf{u}}(t) = \mathbf{\Phi}_0^{\mathrm{T}}\mathbf{M}\dot{\mathbf{u}}(t), \tag{2.14}$$

where $\mathbf{\Phi}_0$ is computed as in Eq. 2.4 by replacing the joints with linear springs.

If the modes are sufficiently uncoupled, then each modal velocity signal $\dot{q}_r(t)$ should contain a single, decaying harmonic. The signal is then modeled with an exponential function,

$$\dot{q}_r(t) = \mathrm{Re}\left[\exp\left(\psi_1(t) + \mathrm{i}\psi_2(t)\right)\right], \tag{2.15}$$

where $\mathrm{i} = \sqrt{-1}$, and the amplitude and phase are slowly-varying functions of time governed by $\psi_1(t)$ and $\psi_2(t)$, respectively. By computing $\dot{\tilde{q}}_r(t)$, the Hilbert transform of $\dot{q}_r(t)$, Feldman [43] shows that the amplitude and phase components can be calculated as

$$\psi_1(t) = \ln\left(\sqrt{\left(\dot{q}_r(t)\right)^2 + \left(\dot{\tilde{q}}_r(t)\right)^2}\right), \tag{2.16}$$

$$\psi_2(t) = \arctan\left(\dot{\tilde{q}}_r(t)/\dot{q}_r(t)\right). \tag{2.17}$$

From these expressions, the amplitude envelope is defined as

$$|\dot{q}_r| \triangleq \exp\left(\psi_1(t)\right), \tag{2.18}$$

the instantaneous damped natural frequency is the time derivative of the phase,

$$\omega_{r,\text{meas}} \triangleq \frac{\mathrm{d}\psi_2}{\mathrm{d}t}, \tag{2.19}$$

the instantaneous critical damping ratio $\zeta_{r,\text{meas}}$ can be calculated from the time derivative of the amplitude component,

$$-\omega_n \zeta_{r,\text{meas}} \triangleq \alpha = \frac{\mathrm{d}\psi_1}{\mathrm{d}t}, \tag{2.20}$$

where ω_n is the undamped natural frequency. Using the substitution $\omega_n = \omega_{r,\text{meas}} / \sqrt{1 - \zeta_{r,\text{meas}}^2}$ in Eq. (2.20), the critical damping ratio is found to be

$$\zeta_{r,\text{meas}} \triangleq \frac{\alpha}{\sqrt{\omega_{r,\text{meas}}^2 + \alpha^2}}. \tag{2.21}$$

Equations (2.18)–(2.21) allow one to estimate the instantaneous damping and natural frequency versus modal velocity amplitude. Equations (2.12) and (2.13), however, are expressed in terms of the modal displacement amplitude. By assuming that the change in amplitude is small over one vibration cycle, Roettgen and Allen [33] derived a simple relationship between the modal displacement $|q_r|$, velocity $|\dot{q}_r|$, and acceleration $|\ddot{q}_r|$ amplitudes as

$$\omega_{r,\text{meas}} |q_r| \approx |\dot{q}_r| \approx \frac{|\ddot{q}_r}{\omega_{r,\text{meas}}}. \tag{2.22}$$

By utilizing Eq. (2.18), (2.19), and (2.21), each $|q_r|$ can be paired with a corresponding $\omega_{r,\text{meas}}$ and $\zeta_{r,\text{meas}}$ occurring simultaneously at time t. This establishes a relationship between amplitude and the measured natural frequency and damping that can be compared with Eq. (2.12) and (2.13).

Reducing Distortion in Signals Processed with the Hilbert Transform

The Hilbert transform of a finite, discrete signal is susceptible to noise as well as end effects at the beginning and tail ends of a finite time signal, which very often produces $\psi_1(t)$ and $\psi_2(t)$ signals that contain spurious oscillation. The differentiation of these signals amplifies the spurious oscillation and leads to distorted curves for the instantaneous damping and frequency. In [32, 33, 44], these oscillations were diminished by fitting polynomial functions to $\psi_1(t)$ and $\psi_2(t)$ via least-squares regression. In the authors' attempt to fit polynomials for the systems examined this work, however, low-order polynomials did a somewhat unsatisfactory job of capturing the shape of $\psi_1(t)$ and $\psi_2(t)$, and higher-order polynomials also tended to exhibit spurious oscillations that were difficult to distinguish from the true underlying function.

For this work, the signals were instead fit with piecewise-linear functions. Such a function is as simple to fit as a low-order polynomial, yet it can follow any curve provided that a sufficiently fine mesh of points is used. The downside, of course, is that the derivative is a step function, which gives the instantaneous frequency and damping curves the appearance of being discontinuous. To address this, the derivative was computed only at the midpoint of each piecewise-linear interval.

To illustrate this fitting technique, Fig. 2.2 shows the damping and natural frequency estimated from the transient response of the Sumali beam that is discussed later (simulation 5 from Table D.1). The signal shown in Fig. 2.2(a) is the absolute value of the modal velocity for mode 7 (first bending mode), which was obtained from simulation via Eq. (2.14). After computing $\psi_1(t)$ and $\psi_2(t)$ using Eq. (2.16) and (2.17), the piecewise linear functions were fitted to these signals using the efficient least-squares algorithm discussed in Allen et al. [45]. The fitting was done after truncating the signals to exclude the beginning and end of the time record so that the end effects do not distort the fitted function. The derivatives of the fitted curves (via Eq. (2.19)–(2.21)) led to the natural frequency and damping curves that are step functions as seen in Fig. 2.2(b) and (c). Only the midpoint values on each of these step functions were retained

for further processing.

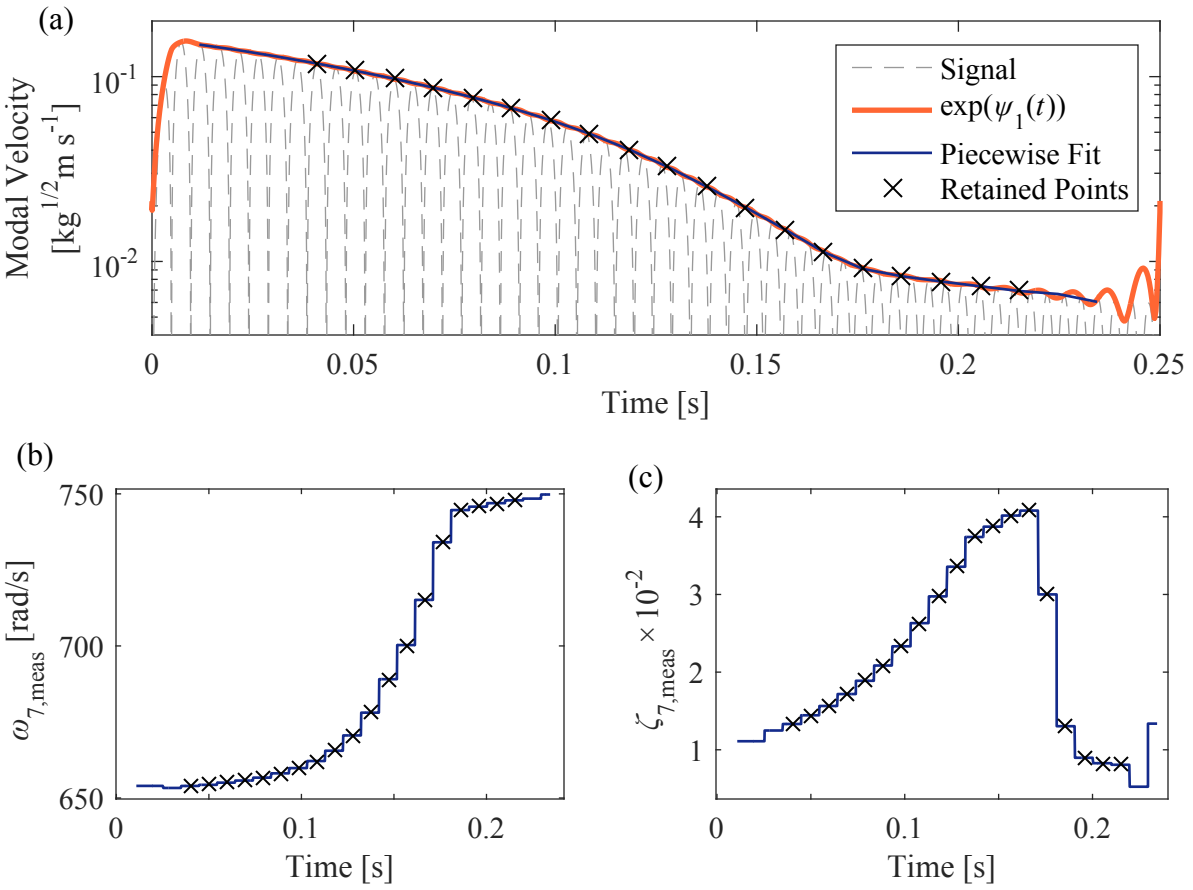

Figure 2.2: *(a) A response signal with Hilbert amplitude envelope, piecewise linear fit, and retained points, and the corresponding (b) instantaneous natural frequency and (c) instantaneous damping ratio. The data come from the response of simulation 5 from Table D.1, which excited mode 7 in the Sumali beam.*

2.2.3 Procedure for Comparison Between the Modal Iwan Model and Truth Simulations

The analysis on each of the two systems studied in this work was divided into two parts. The first part focused on fitting a modal Iwan model to each mode in the system. This part in itself was divided into several steps:

Procedure I

a) An impact force was distributed over the whole system as $\mathbf{F}_{\text{ext}} = \mathbf{M}\boldsymbol{\varphi}_{0r}$ so that only the mode of interest was excited. The response to this impact was simulated until the amplitude at the end of the history was negligible compared to that at the start.

b) A modal filter was applied on the free-response signal using Eq. (2.14) to retrieve the modal response, $q_r(t)$, of interest. The Hilbert analysis described in Section 2.2.2 was performed on the modal signal to collect $\omega_{r,\text{meas}}$, $\zeta_{r,\text{meas}}$, and $|q_r|$.

c) Steps (a) and (b) were repeated for different forcing levels, and $\omega_{r,\text{meas}}$ and $\zeta_{r,\text{meas}}$ were compiled for a wide, logarithmic range of $|q_r|$ spanning the microslip and macroslip regimes.

d) Equations (2.12) and (2.13) ($\omega_{r,\text{fit}}$ and $\zeta_{r,\text{fit}}$) were fit over the compiled $\omega_{r,\text{meas}}$ and $\zeta_{r,\text{meas}}$ by choice of the six modal Iwan model parameters $[\hat{K}_\infty, \zeta_{0r}, \hat{F}_S, \hat{K}_T, \hat{\chi}, \hat{\beta}]$.

e) All steps above were repeated for each mode of interest.

Regarding step (d), the method of fitting used in this work follows a graphical approach similar to that used by Deaner et al. whereby initial guesses are made for the six modal Iwan model parameters based on the shape of the $\omega_{r,\text{meas}}$ versus $|q_r|$ and $\zeta_{r,\text{meas}}$ versus $|q_r|$ curves [32]. The parameters were then adjusted iteratively until the same curves for Eq. (2.12) and (2.13) aligned well with the measured curves. The final values for the six parameters were then associated with the modal Iwan model for that mode.

The second part of the analysis arranged the comparison between the modal Iwan models (as tuned from Procedure I) and the truth measurements for the amplitude-dependent natural frequency and damping. This part required processing not only the response of the system when subjected to discrete impacts, but also the simulated response of the modal Iwan model. The damping and natural frequency for the modal Iwan model were obtained as follows:

Procedure II

f) Equation (2.7) was integrated numerically using the tuned parameters to simulate the free-response decay of the mode of interest to a modal impulse excitation.

g) The Hilbert analysis described in Section 2.2.2 was performed on the modal free-response signal. The instantaneous natural frequency and damping obtained with Eq. (2.19) and (2.21), respectively, were denoted as $\omega_{r,M}$ and $\zeta_{r,M}$ to distinguish them as modal Iwan model properties.

h) Steps (f) and (g) were repeated for multiple excitation levels to compile $\omega_{r,M}$ and $\zeta_{r,M}$ for a logarithmic range of $|q_r|$. These steps were again repeated for every mode with tuned parameters.

The $\omega_{r,M}$ and $\zeta_{r,M}$ versus $|q_r|$ curves were then compared against those obtained from the response of discrete impact excitations, which followed similar steps:

Procedure III

i) The system was excited with an impact applied at a single point on the structure, and the free-response decay signal was collected.

j) Equation (2.14) was applied to filter the signal into its component modes. The signals from all modes of interest were kept since a discrete impact excited more than one mode. The Hilbert analysis of Section 2.2.2 was performed to obtain $\omega_{r,\mathrm{meas}}$ and $\zeta_{r,\mathrm{meas}}$ for all modes of interest (i.e. this was performed on each linear modal coordinate, since each mode could be excited by the discrete impact).

k) Steps (i) and (j) were repeated for multiple excitation levels, and $\omega_{r,\mathrm{meas}}$ and $\zeta_{r,\mathrm{meas}}$ were compiled for each mode.

l) Steps (i) to (k) were repeated for impacts at different discrete locations on the system.

Since different points on a structure give different spatial contributions to each mode, $\omega_{r,\mathrm{meas}}$ and $\zeta_{r,\mathrm{meas}}$ were measured at different impact locations to investigate their range of scatter relative to $\omega_{r,M}$ and $\zeta_{r,M}$.

2.3 Numerical Simulation Test Models

The previous sections describe how to derive closed-form expressions for the damping and natural frequency for a modal Iwan model and fit them to the instantaneous damping and natural frequency estimated from dynamic simulations. This section demonstrates these techniques on two nonlinear models – a three-mass system and a two-beam finite element model – in order to assess the extent to which a modal Iwan model can reproduce the response of these systems.

2.3.1 Three-Mass Discrete System

The first structural model is the same three-degree-of-freedom academic model investigated by Segalman [30]. The three-mass model, as seen in Fig. 2.3, consists of three identical masses, $m = 10$, connected with linear springs of stiffness $k = 9$. A discrete four-parameter Iwan element is placed between the second and third masses with parameters $F_S = 10$, $K_T = 1$, $\chi = -0.5$, and $\beta = 5$.

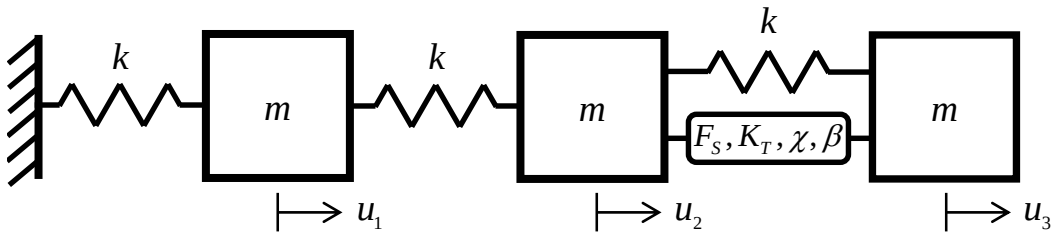

Figure 2.3: *Schematic of the three-mass system with a discrete Iwan joint model connecting the second and third masses.*

The dynamics of this system were modeled using Eq. (2.1). The mass matrix for the three-mass system is defined as

$$\mathbf{M} = \begin{bmatrix} m & 0 & 0 \\ 0 & m & 0 \\ 0 & 0 & m \end{bmatrix}, \tag{2.23}$$

and the stiffness matrices are

$$\mathbf{K}_0 = \begin{bmatrix} 2k & -k & 0 \\ -k & 2k + K_T & -k - K_T \\ 0 & -k - K_T & k + K_T \end{bmatrix}, \quad \mathbf{K}_\infty = \begin{bmatrix} 2k & -k & 0 \\ -k & 2k & -k \\ 0 & -k & k \end{bmatrix} \tag{2.24}$$

The low-amplitude, mass-normalized mode shapes $\boldsymbol{\varphi}_{0r}$ were computed with Eq. (2.4) and are shown in Table 2.1. In observing the relative displacements between the second and third masses, it is apparent that in mode 1 the Iwan joint sees almost an order of magnitude less deflection than for mode 2 or mode 3. Therefore, mode 1 was expected to exercise the Iwan joint less than mode 2 or mode 3, leading to less damping at the same magnitude.

Table 2.1: *Mass-normalized mode shapes for the three-mass system.*

DOF	$\boldsymbol{\varphi}_{01}$ ($\omega_{01} = 0.425$)	$\boldsymbol{\varphi}_{02}$ ($\omega_{02} = 1.216$)	$\boldsymbol{\varphi}_{03}$ ($\omega_{03} = 1.744$)
u_1	0.1051	0.2433	-0.1725
u_2	0.1891	0.0871	0.2380
u_3	0.2307	-0.1822	-0.1166

Each mode of the three-mass system was assigned a linear critical damping ratio of $\zeta_{0r} = 1 \times 10^{-4}$. The damping matrix, $\mathbf{C}$, is then defined as

$$\mathbf{C} = \mathbf{M}\boldsymbol{\Phi}_0 \mathrm{diag}\left[2\omega_{0r}\zeta_{0r}\right] \boldsymbol{\Phi}_0^{\mathrm{T}}\mathbf{M}, \tag{2.25}$$

with $\mathrm{diag}\left[2\omega_{0r}\zeta_{0r}\right]$ denoting a diagonal matrix where the rth diagonal entry contains the value

$2\omega_{0r}\zeta_{0r}$. Lastly, the joint force vector is defined as

$$\mathbf{F}_J = \begin{bmatrix} 0 \\ -F_I \\ F_I \end{bmatrix}, \tag{2.26}$$

where F_I is the force exerted on the system by the discrete Iwan element (see Appendix A), which depends on the relative displacement $u_3 - u_2$.

Tuning Modal Iwan Models to the Three-Mass System

The first set of simulations for the three-mass system selectively excite each of the three modes to parameterize a modal Iwan model for each mode. To excite a single mode, $\mathbf{F}_{\text{ext}}$ in Eq. (2.1) is defined as follows:

$$\mathbf{F}_{\text{ext}}(t) = p\mathbf{M}\boldsymbol{\varphi}\sin\left(\omega_{0r}t\right), \quad 0 \leq t \leq \pi/\omega_{0r}, \tag{2.27}$$

where p is a scalar multiplier used to adjust the force magnitude, and the mode shape vector $\boldsymbol{\varphi}$ is a placeholder for either $\boldsymbol{\varphi}_{0r}$ or $\boldsymbol{\varphi}_{\infty r}$. When completing the simulations, $\boldsymbol{\varphi}_{0r}$ tended to give cleaner modal coordinate signals (not contaminated by signals from other modes) when the system was excited in microslip, whereas $\boldsymbol{\varphi}_{\infty r}$ gave cleaner signals for macroslip excitations. Therefore, the two vectors were interchanged depending on the value of p. The values of p and the corresponding $\boldsymbol{\varphi}$ used in these simulations are listed in Table 2.2. Equation (2.1) was integrated numerically in MATLAB® using an iterative, average-acceleration Newmark method [46] with a time step of 2×10^{-2} for 200,000 steps in all simulations on this system.

Table 2.3 lists the modal Iwan model parameters that were estimated for each mode after following Procedure I in Section 2.2.3. Note that for all three modes, $\zeta_{0r} = 1 \times 10^{-4}$ is the same value that was prescribed for linear damping in Eq. (2.25). This makes sense because Eq. (2.5) establishes that, in the limit that displacement amplitude goes to zero, the system

Table 2.2: *The p values and $\boldsymbol{\varphi}$ vectors used in the simulations that excite each mode of the three-mass system.*

Mode 1			Mode 2			Mode 3		
Sim No.	p	$\boldsymbol{\varphi}$	Sim No.	p	$\boldsymbol{\varphi}$	Sim No.	p	$\boldsymbol{\varphi}$
1	6000	$\boldsymbol{\varphi}_{\infty 1}$	10	50,000	$\boldsymbol{\varphi}_{\infty 2}$	19	200,000	$\boldsymbol{\varphi}_{\infty 3}$
2	3000	$\boldsymbol{\varphi}_{\infty 1}$	11	10,000	$\boldsymbol{\varphi}_{\infty 2}$	20	75,000	$\boldsymbol{\varphi}_{\infty 3}$
3	1000	$\boldsymbol{\varphi}_{\infty 1}$	12	3,400	$\boldsymbol{\varphi}_{\infty 2}$	21	15,000	$\boldsymbol{\varphi}_{\infty 3}$
4	450	$\boldsymbol{\varphi}_{\infty 1}$	13	200	$\boldsymbol{\varphi}_{\infty 2}$	22	5600	$\boldsymbol{\varphi}_{\infty 3}$
5	150	$\boldsymbol{\varphi}_{\infty 1}$	14	9	$\boldsymbol{\varphi}_{02}$	23	150	$\boldsymbol{\varphi}_{\infty 3}$
6	33	$\boldsymbol{\varphi}_{01}$	15	3	$\boldsymbol{\varphi}_{02}$	24	12	$\boldsymbol{\varphi}_{03}$
7	10	$\boldsymbol{\varphi}_{01}$	16	0.8	$\boldsymbol{\varphi}_{02}$	25	2	$\boldsymbol{\varphi}_{03}$
8	3.4	$\boldsymbol{\varphi}_{01}$	17	0.2	$\boldsymbol{\varphi}_{02}$	26	0.38	$\boldsymbol{\varphi}_{03}$
9	1	$\boldsymbol{\varphi}_{01}$	18	0.4	$\boldsymbol{\varphi}_{02}$	27	0.096	$\boldsymbol{\varphi}_{03}$
–	–	–	–	–	–	28	0.192	$\boldsymbol{\varphi}_{03}$

approaches the linear extreme in which the equivalent modal damping is equal to ζ_{0r}. In other words, $\zeta_{r,\text{meas}}$ asymptotes to ζ_{0r} at low amplitudes.

Table 2.3: *Fitted modal Iwan parameters for the three-mass system.*

Parameter	Mode 1	Mode 2	Mode 3
$\hat{K}_\infty$	0.1782	1.399	2.922
ζ_{0r}	1.0×10^{-4}	1.0×10^{-4}	1.0×10^{-4}
$\hat{F}_S$	0.4462	2.877	3.278
$\hat{K}_T$	1.917×10^{-3}	7.843×10^{-2}	0.1196
$\hat{\chi}$	-0.5002	-0.5150	-0.5070
$\hat{\beta}$	5.700	5.614	4.800

Figure 2.4 plots the compiled $\omega_{2,\text{meas}}$ and $\zeta_{2,\text{meas}}$ versus $|q_2|$ data for mode 2 obtained from the simulations of Table 2.2. The data are juxtaposed with the fitted $\omega_{2,\text{fit}}$ and $\zeta_{2,\text{fit}}$ curves produced from the parameters listed in Table 2.3 and using the closed-form expressions in Eq. (2.12) and (2.13). Here it can be seen that the fitted curves follow the measured data very well in the microslip regime and in the late macroslip regime, but error can be seen in early macroslip at around $|q_2|=10^2$. This is simply an approximation error in the closed form expressions, and it can be avoided by simulating the response of the 1-DOF modal Iwan model, as explained below, rather than relying on the closed-form expressions. The frequency and damping versus

amplitude plots for the first and third modes look similar to those in Fig. 2.4, and are shown in Fig. C.1 in Appendix C.

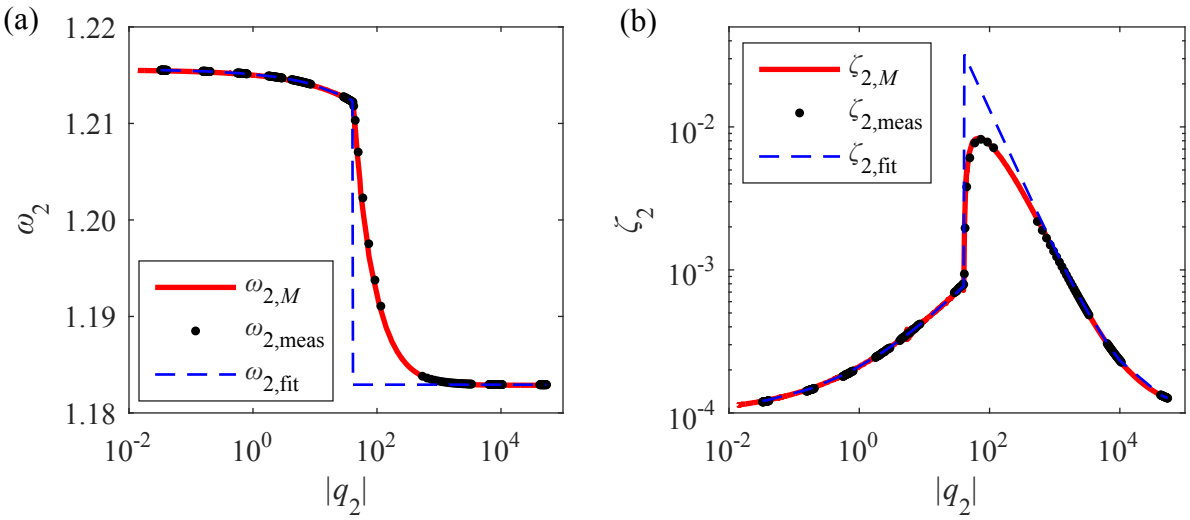

Figure 2.4: *(a) Natural frequency and (b) critical damping ratio versus modal displacement amplitude when the 2nd mode of the three-mass system is selectively excited.*

Time domain simulations on the modal Iwan model were then conducted for all three modes by following Procedure II in Section 2.2.3 using the parameters listed in Table 2.3. The modal force in Eq. (2.7) was defined as

$$\hat{F}_r(t) = p \sin(\omega_{0r} t), \quad 0 \leq t < \pi/\omega_{0r}. \tag{2.28}$$

The same number of simulations as listed in Table 2.2 were conducted using the same p values. The simulations were completed by numerically integrating Eq. (2.7) in MATLAB® using the Newmark method with a time step of 2×10^{-2} for 400,000 steps. The compiled $\omega_{r,M}$ and $\zeta_{r,M}$ versus $|q_2|$ curves from the mode 2 simulations are plotted with the measured data and fitted curves in Fig. 2.4. With selective modal excitation, one can observe that the modal Iwan model fits the measured response of each mode very well in both regimes of slip. The same conclusion can be drawn from the $\omega_{r,M}$ and $\zeta_{r,M}$ curves for modes 1 and 3 in Fig. C.1.

Of particular note for the second and third modes is that the damping in the microslip

regime increases to more than six times the low-amplitude damping as the macroslip regime is approached. Clearly, to model this system as linear with only the low-amplitude damping would result in a stark underestimation of the damping. The first mode, on the other hand, only shows a doubling of damping in the microslip regime, but this might be expected since the first mode shape barely exercises the Iwan element.

Discrete Impact Simulations on the Three-Mass System

the $\omega_{r,M}$ and $\zeta_{r,M}$ curves computed in Section 2.3.1 for the three-mass system were then tested against the measured damping and natural frequency produced from impact excitations on each mass individually. To retrieve the data, Eq. (2.1) was again integrated numerically, but the external force was computed as

$$\mathbf{F}_{\text{ext}}(t) = p\mathbf{P}\sin\left(\omega_{03}t\right), \quad 0 \leq t < \pi/\omega_{03}, \tag{2.29}$$

where $\mathbf{P}$ is a vector of zeros except for a single 1 in the entry corresponding to the mass where excitation is desired. Nine impact simulations were conducted on each mass for p equal to 150,000, 50,000, 15,000, 5000, 300, 10, 3, and 1. The same integrator settings used for the mode excitation simulations were also used for these simulations. Figures 2.5–2.7 show the $\omega_{r,\text{meas}}$ and $\zeta_{r,\text{meas}}$ versus $|q_r|$ curves for the first, second and third modes, respectively, as computed using Procedure III from Section 2.2.3.

Comparison and Results Discussion

The results in Fig. 2.5–2.7 show that the modal Iwan model does a good job of predicting the effective natural frequency and damping of the system, but there are some discrepancies that can be significant in some cases. The microslip regime (far left in each plot) is considered first as this is the regime in which joints are typically designed to function, and it is also the regime in which the modal approach is expected to be reasonably accurate.

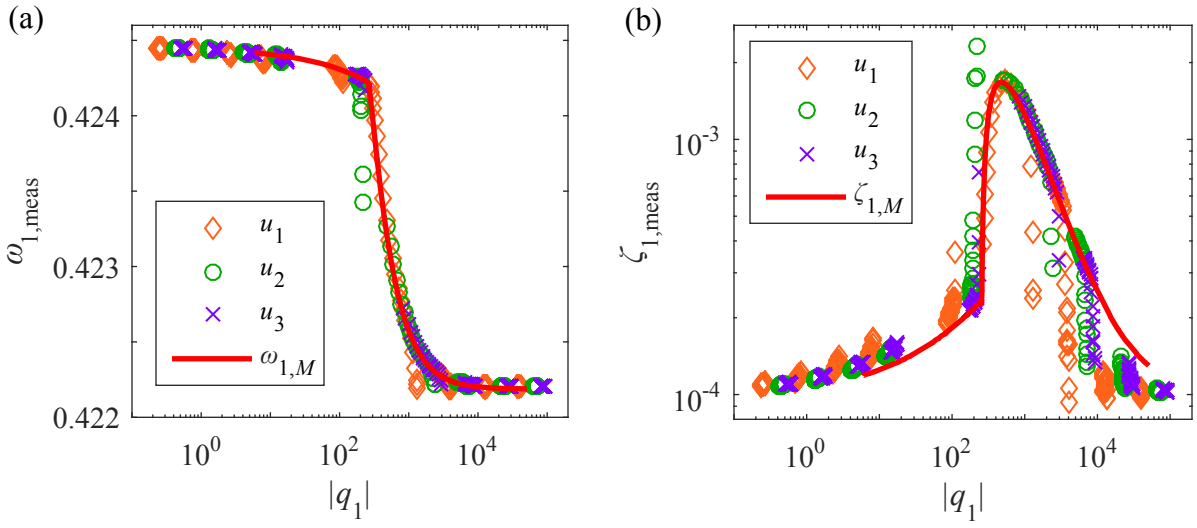

Figure 2.5: *The measured (a) natural frequency and (b) damping ratio versus modal displacement amplitude for the mode 1 response to discrete impulses on the three-mass system. Points denoted with the same marker originated from a simulation where the mass noted in the legend was excited. The $\omega_{r,M}$ and $\zeta_{r,M}$ from the modal Iwan model is overlaid for comparison.*

While the modal Iwan model is qualitatively correct in the microslip regime, it does significantly underestimate the damping in several cases. In general, the largest error in damping seems to occur when a mode is weak at the excitation point. This makes sense because the response to an impulse at that point is dominated by a different mode, so the single-mode approximation for the weak mode becomes less accurate. For example, the second mode for the three-mass system is very weak when mass u_2 is excited, and the modal Iwan model underestimates damping by as much as 67% in microslip for that case. However, with that same excitation, the first and third modes are more strongly excited, so the modal Iwan models for these modes are more accurate, underestimating damping by no more than 13% for the first mode and 17% for the third mode.

Considering now the entire plots, including the macroslip regime, the modal Iwan model seems to underestimate microslip damping yet overestimate macroslip damping in all simulations. Most striking for the second and third modes is that the modal Iwan model vastly underpredicts (by a whole order of magnitude) the simulations that occur in the early macroslip

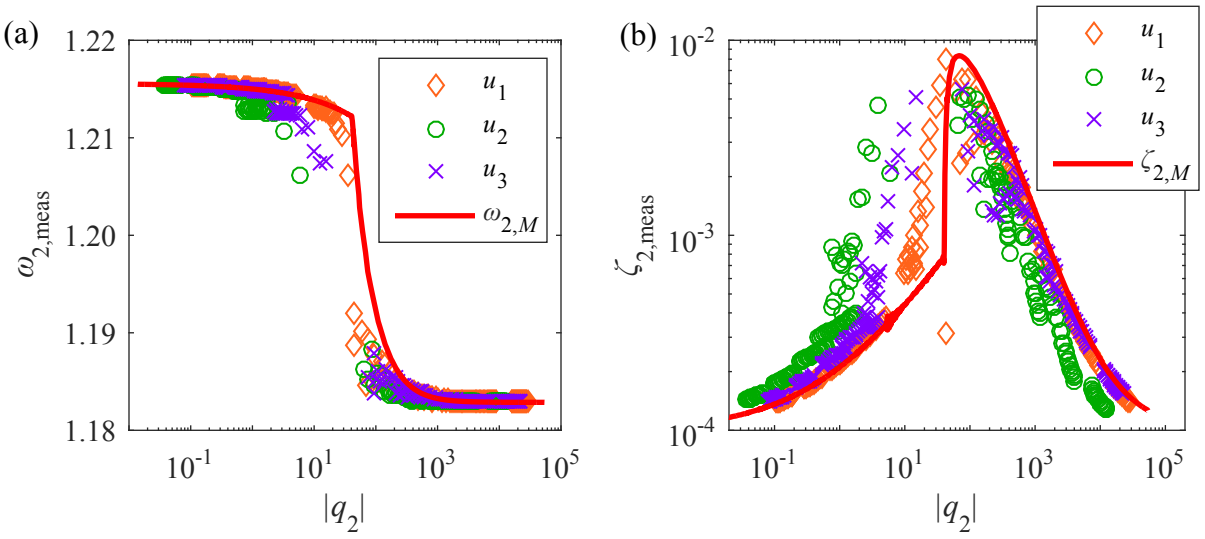

Figure 2.6: *The measured (a) natural frequency and (b) damping ratio versus modal displacement amplitude for the mode 2 response to discrete impulses on the three-mass system.*

regime and transition into the microslip regime.

Quantitatively, the cause for this apparent shift in the damping curves may be accounted for by considering nonlinear coupling between modes. Recall that the formulation for the modal Iwan model is described fundamentally by Eq. (2.7), where the modal Iwan force $\hat{F}_I$ is assumed to be a function of the native modal coordinate only. This is a simplification of $\boldsymbol{\varphi}_{0r}^{\mathrm{T}}\mathbf{F}_J$, which is a function of all modal degrees of freedom. For the three-mass system, the exact projection of joint forces onto a particular mode r is actually

$$\boldsymbol{\varphi}_{0r}^{\mathrm{T}}\mathbf{F}_J(\mathbf{u}) = \boldsymbol{\varphi}_{0r}^{\mathrm{T}}\mathbf{F}_J(\boldsymbol{\varphi}_{01}q_1 + \boldsymbol{\varphi}_{02}q_2 + \boldsymbol{\varphi}_{03}q_3). \tag{2.30}$$

When the second mode is selectively excited (as in Fig. 2.4), then q_2 is dominant in F_J and the modal Iwan assumption is reasonable. On the other hand, a force at a single point excites all modes at once. As a result, the state of the joint is governed by a linear combination of the active modal coordinates, so the damping is activated to a higher amplitude than would be expected from q_2 alone. This activation to higher amplitude is the source of the downward shift in amplitude that $\omega_{r,\text{meas}}$ and $\zeta_{r,\text{meas}}$ seem to experience relative to $\omega_{r,M}$ and $\zeta_{r,M}$ seen in Fig.

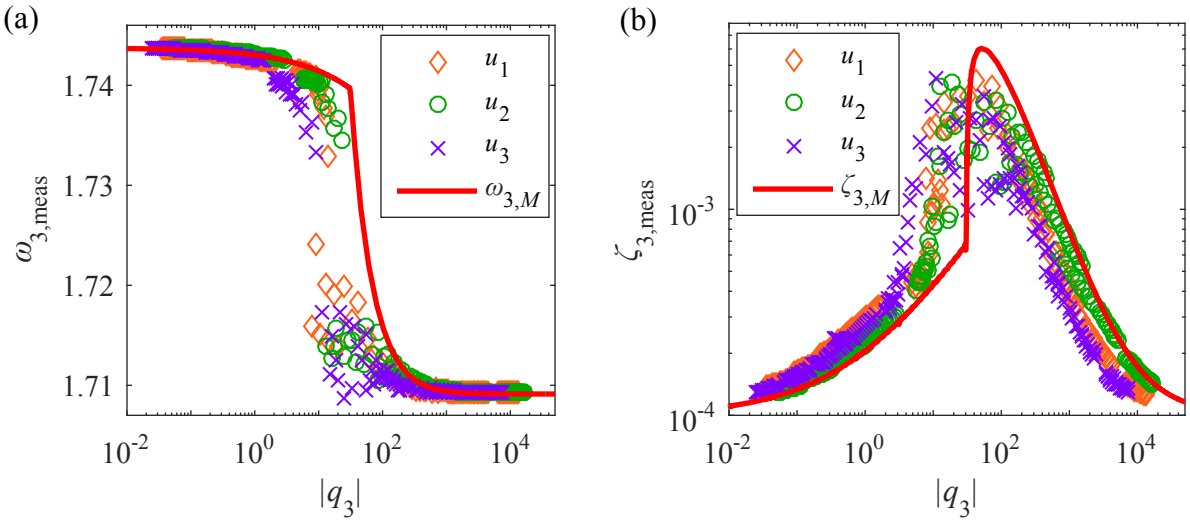

Figure 2.7: *The measured (a) natural frequency and (b) damping ratio versus modal displacement amplitude for the mode 3 response to discrete impulses on the three-mass system.*

2.5–2.7.

Figure 2.8 illustrates this effect for mode 1 using the $p = 15{,}000$ simulation for excitation at mass u_2. Figure 2.8(a) shows that the measured damping ratio for mode 1 starts at a low value, but then rises up to match the analytical curve with only slight change in modal displacement amplitude. This phenomenon appears contradictory, but the plot does not show the response of the second and third modes. If the damping curve in Fig. 2.8(a) is instead shown versus time (Fig. 2.8(b)), one notices that the damping ratio is consistent with that of the modal Iwan model for time $t > 1700$.

Figure 2.8(c) shows that the amplitude envelopes for the three modal coordinates versus time in this same simulation. It is clear that modes 2 and 3 are nearly as significant as mode 1 at the beginning of the time history. Therefore, at the beginning of the simulation, the joint forces $\mathbf{F}_J(\mathbf{u})$ produce lower damping in mode 1 than would be expected if only mode 1 were excited, and this is because the physical Iwan element is activated to a higher amplitude within macroslip. The other modes q_2 and q_3 decay rapidly until $t > 1700$, at which point they can be considered small compared to q_1. At this point, $\mathbf{F}_J$ can be considered to depend on q_1 only, so

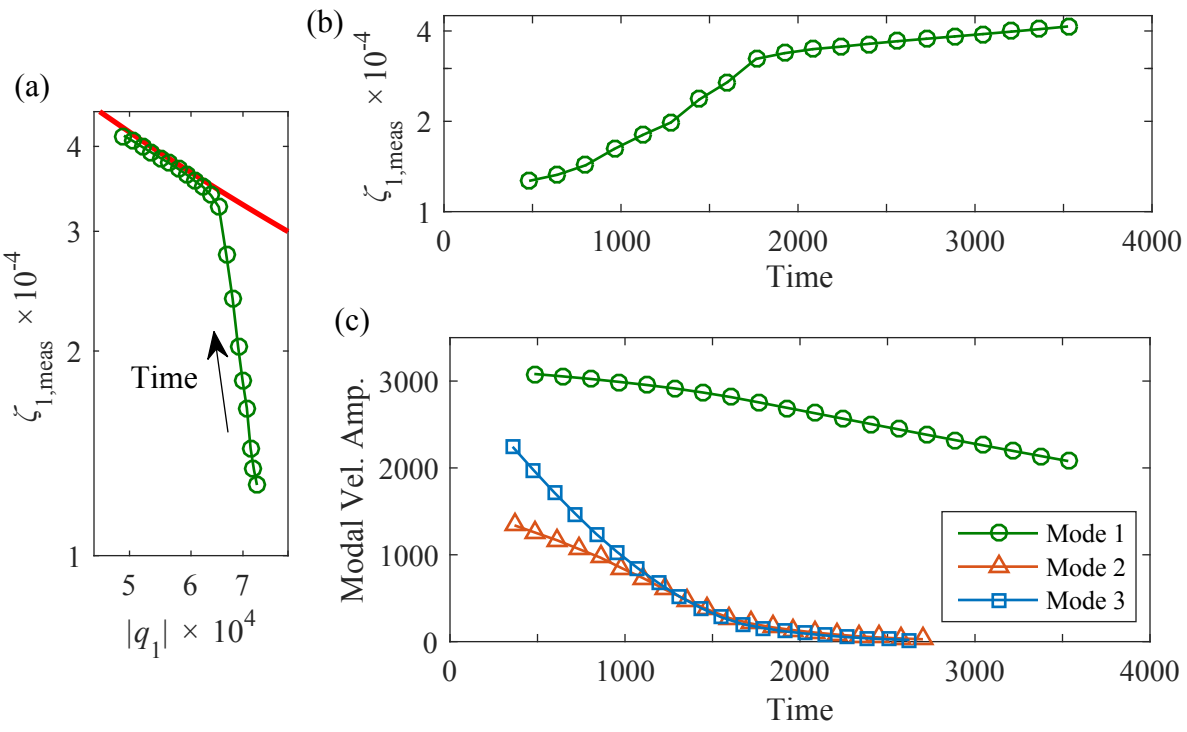

Figure 2.8: *(a) Damping versus displacement amplitude (shown with $\zeta_{1,M}$ as the thick line) and (b) damping versus time for Mode 1 response to an impulse on mass u_2, and (c) the modal velocity amplitude time histories for all three modes in the same simulation. The data are from the $p = 15{,}000$ simulation for the three-mass system. Time units are in seconds, modal displacement amplitudes are in $kg^{1/2}m$, and modal velocity amplitude units are in $kg^{1/2}m\ s^{-1}$.*

$\zeta_{1,\text{meas}}$ then follows $\zeta_{1,M}$ closely.

In summary, the error in the modal Iwan model can be accounted for by considering the neglected modal coupling. In the truth models, the coupling causes the physical joints to be activated to a higher amplitude than would be expected from a single modal coordinate in isolation. This explains why the modal Iwan model underestimates damping in microslip and overestimates damping in macroslip.

Even so, the error is not bad if the impacts excite the three-mass system to amplitudes confined well within the microslip or macroslip regimes. In microslip, the error is greatest in mode 2 where $\zeta_{1,M}$ underestimates the mass 2 impact measurements by a factor of 0.6 (67% underestimation) at amplitude $|q_2| = 0.5$. The error in macroslip is greatest for mode 1, where

an excitation on mass 1 causes $\zeta_{1,M}$ to overestimate the measurements at the beginning of the time signal by a factor of 5 (400% overestimation) at $|q_1| = 4000$. The modal signal in both of these cases, however, does not dominate the response, so although that mode's damping would not be simulated accurately, its contribution to the overall response may be neglected. For the most dominant modal signals, $\zeta_{r,M}$ underestimates the modal signals confined within microslip by an average of 5.6%, and overestimates those confined within macroslip by an average of 23%.

The modal Iwan model produces the greatest error in the late microslip region near the threshold for macroslip. Based on the amplitude of the native modal coordinate, the modal Iwan model predicts that the structure should be in "modal microslip," but in the truth models the physical joint itself has already passed the threshold for macroslip due to the added contribution from other modes. Therefore, the measured modal damping has already been pushed into the peak region of the curve, causing the modal Iwan model to underestimate the measured damping by a whole order of magnitude. This error must be accepted if one wishes to profit from the advantages of a modal Iwan model. However, there is consolation in the fact that joints are designed to operate in microslip. In fact, experimental studies have shown that it is notoriously difficult to impact a real, experimental structure with a hammer such that macroslip or transitioning behavior can be measured [32, 33]. More often than not, one desires a model that describes microslip behavior. One notable exception is the case of blast loads as experienced when stages of launch vehicles separate, so there is certainly interest in extending this work so that macroslip can be captured.

2.3.2 Sumali Beam Finite Element Model

To see whether these findings would hold for a more realistic structure, a finite element model of an assembly of two beams, here dubbed the Sumali beam, was also investigated. Deaner et al. studied this same structure in experiments and fitted modal Iwan models to their measure-

ments [32], so some effort was made to tune the finite element model so that it approximated their results.

The Sumali beam structure contains two thin, identical, stainless steel beams that overlap and are joined with four bolts, as shown in Fig. 2.9. Each beam has length 508 mm, width 50.8 mm, and thickness 6.35 mm, and the area of overlap extends 355.6 mm along the length of each beam. The four bolts are distributed in single file along the middle axis of the beam, each separated by a uniform distance of 76.2 mm.

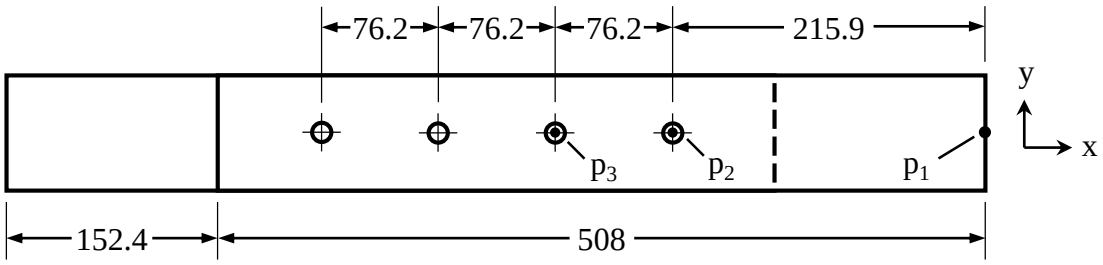

Figure 2.9: *Schematic of the Sumali beam with major dimensions. Length units are in millimeters. Figure is not drawn to scale.*

The two beams were included in the finite element model used in this analysis. Each beam was meshed with 640 8-node hexahedron elements constructed using an isotropic, elastic material model with Young's modulus 248 GPa, Poisson's ratio 0.29, and mass density 8000 kg m^{-3}. The boundary conditions were taken to be in free-free configuration to match the experimental setup.

The bolts themselves where not meshed, but were instead replaced by discrete joint models located between the beams. The forces exerted by each joint model were distributed over an area of contact surrounding the position where each bolt would be found. An illustration of each joint model is given in Fig. 2.10. On the two interfacing surfaces of the beams, all nodes within a 25.4 $\times$ 25.4 mm square contact patch surrounding a bolt were tied to a virtual node using a RBE3 element spider [47], a type of averaging multi-point constraint. This virtual node represents an average of all degrees of freedom (DOF) on the contact patch in both translation

and rotation. The six DOF from one virtual node were then coupled to the six DOF from the corresponding virtual node on the opposite surface using a joint model consisting of linear springs, Iwan elements, and rigid constraint equations, the details of which are given in Section 2.3.2.

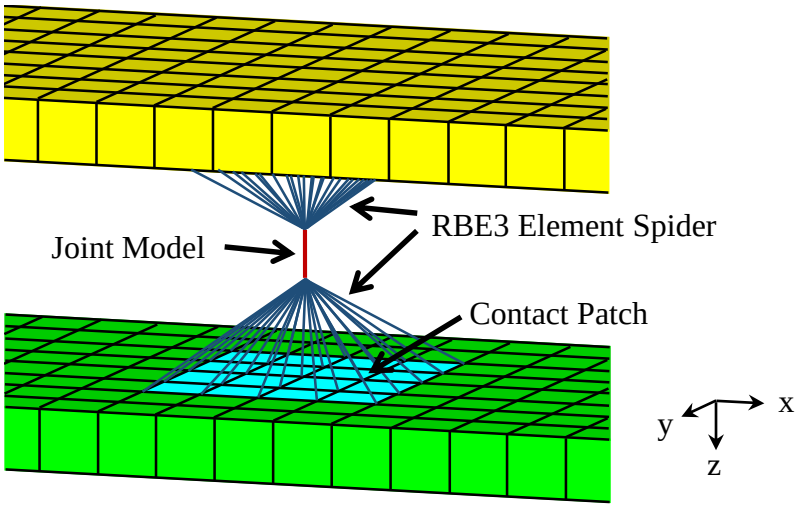

Figure 2.10: *Exploded view of a discrete joint model in the Sumali beam finite element model.*

To speed up computation time for simulation, the mass and stiffness matrices produced from this finite element model (sans the joint models) were reduced using the Craig-Bampton reduction technique [48]. The eight joint virtual nodes (six DOF each) were retained as the interface in the Craig-Bampton model, along with point p_1 (three translational DOF) shown in Fig 2.9, so there were a total of 51 constraint modes. Of the resulting fixed-interface modes, only the first ten were kept to include the first torsion and the first three bending modes. The reduction was performed internally within SIERRA/SD [47], a structural dynamics solver for finite element models developed by Sandia National Laboratories. The reduced mass and stiffness matrices were then imported into MATLAB®, where the joint models were added and the response of the assembly was simulated.

Joint Model Characterization

Deaner et al. [32] measured the natural frequencies and modal Iwan parameters for the first three modes of the Sumali beam at three different bolt torque values. The measurements pertaining to the torque of 3.39 N m were used to tune the model for this work. An independent set of parameters for each of the four joint models cannot be determined from the provided experimental data, so all joint models were simply assumed to have the same parameterization.

For simplicity, a single Iwan element was oriented in the x-translation direction in each joint model since it was assumed that the first few bending modes exercise friction in this direction the most. In a first pass, though, only linear springs were attached to each translational and rotational DOF (except z-rotation to allow out-of-plane rotation), and the stiffness of each spring was then adjusted iteratively until the linear natural frequencies of the beam matched (as closely as possible) the low-amplitude natural frequencies measured in [32]. In this iterative process, it was found that adjusting the stiffness of the z-translation, and x and y-rotation springs, did not affect the natural frequencies significantly. Those DOF were instead rigidly coupled using a constraint equation to further reduce the total number of DOF to 49.

As a result of the updating steps described above, the natural frequencies of the first and second bending modes matched the experimentally-derived values well (at low amplitude excitation). The stiffness of the x-translation spring was then decreased until the linear natural frequencies closely matched the high-amplitude natural frequencies reported in [32]. The amount of decrease in the stiffness of the x-translational spring became the value of the tangent stiffness parameter, K_T, for the discrete Iwan models. The other three parameters, F_S, χ, and β, were simply taken as the geometric mean of the modal Iwan values reported for the first three bending modes [32]. While this updating procedure had not resulting in a model that rigorously matched the dynamic response that was measured, it was thought nonetheless to be a feasible truth model, and it showed ample joint energy dissipation for the study that follows.

The final elements used for all four joint models are a linear spring with stiffness 5.3×10^7

N m^{-1} oriented in the x-translation direction, a linear spring with stiffness 5.25$\times$10^8 N m^{-1} oriented in y-translation, and an Iwan element with parameters $F_S = 30.7$ N, $K_T = 4.73\times10^8$ N m^{-1}, $\chi =$ -0.23, and $\beta = 0.46$ oriented in x-translation in parallel with the spring. The natural frequencies of the assembly can then be computed with and without the joints present, and Table 2.4 lists the final low and high-amplitude natural frequencies (computed from Eq. (2.4)) for the Sumali beam with free-free boundary conditions. The first six modes are rigid body modes, while modes 7, 8, and 9 are the first, second and third bending modes, respectively.

Table 2.4: *Comparison between finite element model and experiment for low-amplitude natural frequencies, ω_0, and high-amplitude natural frequencies, ω_∞, of the Sumali beam.*

Mode	Model ω_0 (rad s^{-1})	Deaner [32] ω_0 (rad s^{-1})	Error	Model ω_∞ (rad s^{-1})	Deaner [32] ω_∞ (rad s^{-1})	Error
7	759.3	759.6	0.04%	652.2	664.1	1.79%
8	1345	1350	0.37%	1297	1145	13.3%
9	3185	2976	7.02%	2713	2739	0.95%

Tuning Modal Iwan Models to the Sumali Beam System

As was done for the three-mass system, modal Iwan models were tuned for the Sumali beam system first by exciting the system using the force defined in Eq. (2.27), and the response was found by integrating Eq. (2.1) using a Newmark algorithm in MATLAB®. The mass matrix $\mathbf{M}$ in this case is the reduced mass matrix from the Craig-Bampton reduction. The stiffness matrix $\mathbf{K}_\infty$ is the reduced stiffness matrix that includes coupling terms from the linear springs in the joint models, but not the stiffness contribution from the Iwan elements. The damping matrix was calculated with Eq. (2.25), again assigning $\zeta_{0r} = 1\times10^{-4}$ for all modes. The forces from all Iwan elements are summed in the $\mathbf{F}_J$ vector while following the same sign convention used in Eq. (2.26). The force magnitude p values and mode shape $\boldsymbol{\varphi}$ vectors used for excitation are listed in Table D.1 in Appendix D.

Procedure I (Section 2.2.3) was completed to retrieve $\omega_{r,\mathrm{meas}}$ and $\zeta_{r,\mathrm{meas}}$ for these modal excitation simulations and fit $\omega_{r,\mathrm{fit}}$ and $\zeta_{r,\mathrm{fit}}$ curves. The fitted modal Iwan model parameters are

listed in Table 2.5. Then Procedure II was completed to simulate the modal Iwan model, where each simulation was performed using the model parameters listed in Table 2.5, the excitation given in Eq. (2.28), and the same integrator parameters given in Table 2.5.

Table 2.5: *Modal Iwan parameters for the Sumali beam reduced-order model.*

Parameter	Mode 7	Mode 8	Mode 9
$\hat{K}_\infty$ [s^{-2}]	4.235×10^5	1.673×10^6	7.321×10^6
ζ_{0r}	1.0×10^{-4}	1.0×10^{-4}	1.0×10^{-4}
$\hat{F}_S$ [N kg$^{-1/2}$]	1.802	1.518	6.934
$\hat{K}_T$ [s^{-2}]	1.537×10^5	1.340×10^5	2.822×10^6
$\hat{\chi}$	-0.1369	-0.1620	-0.1008
$\hat{\beta}$	2.561	2.000	1.529

The measured, fitted, and modal Iwan frequency and damping curves for mode 8 are shown in Fig. 2.11. The agreement between the measured and modal Iwan curves is representative of those of mode 7 and mode 9, which are illustrated in Fig. D.1 in Appendix D. Again, the modal Iwan model reproduces the frequency and damping exceptionally well over a wide range of amplitudes. Also noted is that the damping in microslip for the second bending mode rises to a value 20 times greater than that of the low-amplitude, linear damping. For the first and third bending modes, the damping rises by a factor of almost 100. This shows, again, how modeling the system linearly with low-amplitude damping is insufficient to capture the dynamic response for a more general range of amplitudes.

Discrete Impact Simulations on the Sumali Beam System

Procedure III was implemented to acquire $\omega_{r,\mathrm{meas}}$ and $\zeta_{r,\mathrm{meas}}$ from the measured response to point impact excitations on the Sumali beam. Three impact locations were investigated, corresponding to points p_1, p_2, and p_3 shown in Fig. 2.9, with the force oriented along the z direction. Point p_1 is a node located midway along the edge of the beam. Points p_2 and p_3 are bolt locations, but in the finite element model the force is actually applied on the coordinate governing the z-translation degree of freedom in the two virtual nodes at each point. The shape of the

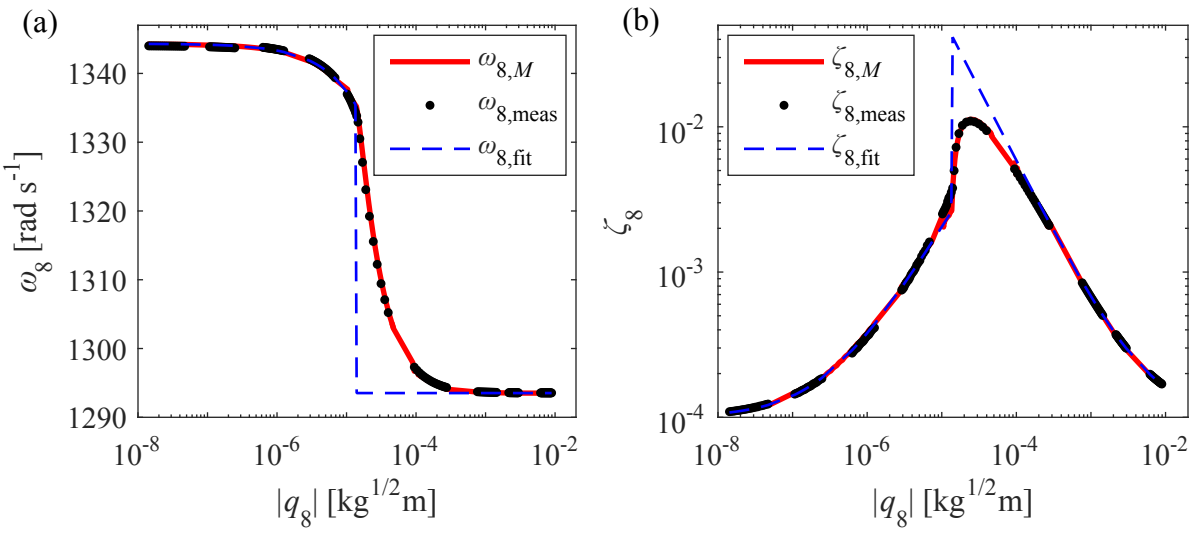

Figure 2.11: *(a) Natural frequency and (b) damping ratio versus modal displacement for selective excitation of mode 8 of the Sumali beam.*

impact force follows Eq. (2.29) except with the mode 9 natural frequency, ω_{09}, substituted in place of ω_{03}. The force multiplier p values, and other simulation parameters, are listed in Table D.2 in Appendix D. The $\omega_{r,\text{meas}}$ and $\zeta_{r,\text{meas}}$ curves for all three excitation points are compared with $\omega_{r,M}$ and $\zeta_{r,M}$ obtained from Section 2.3.2 in Fig. 2.12 (mode 7), Fig. 2.13 (mode 8), and Fig. 2.14 (mode 9).

Sumali Beam Results Discussion

Similar to the three-mass system, the modal Iwan models do well in maintaining the shape of the frequency and damping curves for the seventh and eighth modes. However, the models are in error for the same reasons regarding modal coupling discussed in Section 2.3.1.

In the seventh mode, for example, $\zeta_{7,M}$ underestimates the measured damping for the impulse response at point p_2 (least dominant modal signal) by an average of 68% near the late microslip regime. This discrepancy decreases to a 44% underestimation at lower amplitudes. In mode 8, $\zeta_{8,M}$ maintains an average underestimation of 66% of the measured damping for the point p_3 simulations in all of the microslip regime. Besides these cases, impulsive excitations

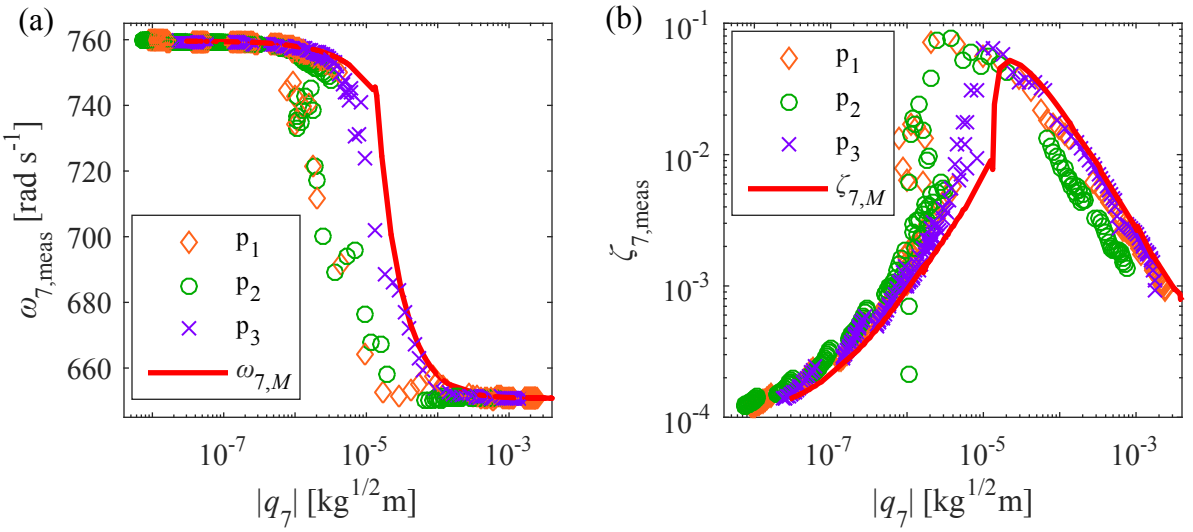

Figure 2.12: *The measured (a) natural frequency and (b) damping ratio versus modal displacement amplitude for the mode 7 response to discrete impulses on the Sumali beam system. Points denoted with the same marker originated from a simulation where the same point was excited. The $\omega_{r,M}$ and $\zeta_{r,M}$ from the modal Iwan model are overlaid for comparison.*

at other points produce damping curves that are closer to the modal Iwan model for these two modes. The modal Iwan model generally underestimates the measured damping for the most dominant modal signals by an average of 40% at large microslip amplitudes, and this error decreases to 25% at lower amplitudes. In macroslip, $\zeta_{r,M}$ generally overestimates those measured by an average of 60% in the seventh and eighth modes.

As seen for the three-mass system, $\zeta_{r,M}$ in the late microslip regime for modes 7 and 8 underpredicts, by an order of magnitude, the damping measured from simulations transitioning from macroslip to microslip. In these simulations, the amplitude of the physical response is such that one or more of the physical Iwan elements enters macroslip. Hence, the measured damping reflects that of the peak region in the early macroslip regime. When the response is filtered into its component modes, however, the amplitude of each modal signal is such that its corresponding modal Iwan model predicts damping in the late microslip. It is because the measured damping for macroslip is attributed to the modal amplitude corresponding to microslip that there results an order-magnitude of difference between the measured and predicted

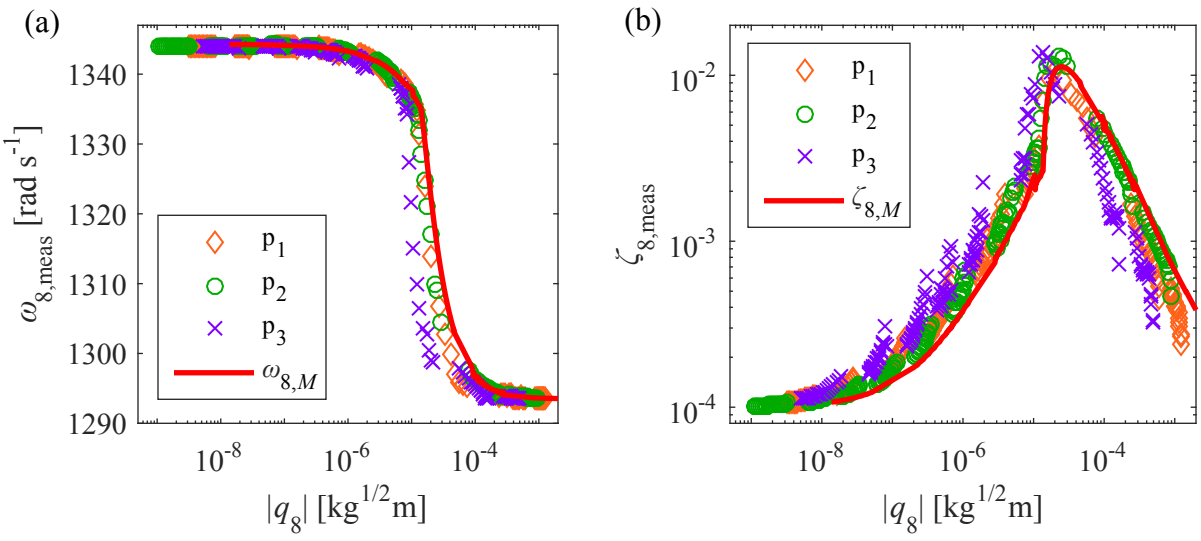

Figure 2.13: *The measured (a) natural frequency and (b) damping ratio versus modal displacement amplitude for the mode 8 response to discrete impulses on the Sumali beam system.*

damping. As explained in the final paragraph of Section 2.3.1, joints are generally designed to maintain their integrity and remain well within microslip, so it is not likely that this region of amplitude would be reached in practice.

In contrast to the seventh and eighth modes, the damping of the modal Iwan model for the ninth mode is in considerable disagreement with those of simulations (up to 300% estimation in microslip). This, in addition to the curves with the largest deviations in modes 7 and 8, is again accounted for by other significant modes in the response. Looking specifically at the results of simulation 6 in Table D.2 (third smallest excitation of point p_1 in microslip), it can be seen from Fig. 2.15 that the ninth modal coordinate decays rapidly compared to the seventh and eighth coordinates, which decay at about the same rate. As discussed earlier, this increases the measured damping in mode 9 such that it deviates further from the modal Iwan model as time advances. However, one should note that the ninth mode is weakly excited from this input, so its contribution to the response may not be important. The damping for the seventh and eighth modes also show noticeable deviations, and both of these modes are important to the response. However, overall, the modal Iwan model is still very appealing because it does a good job of

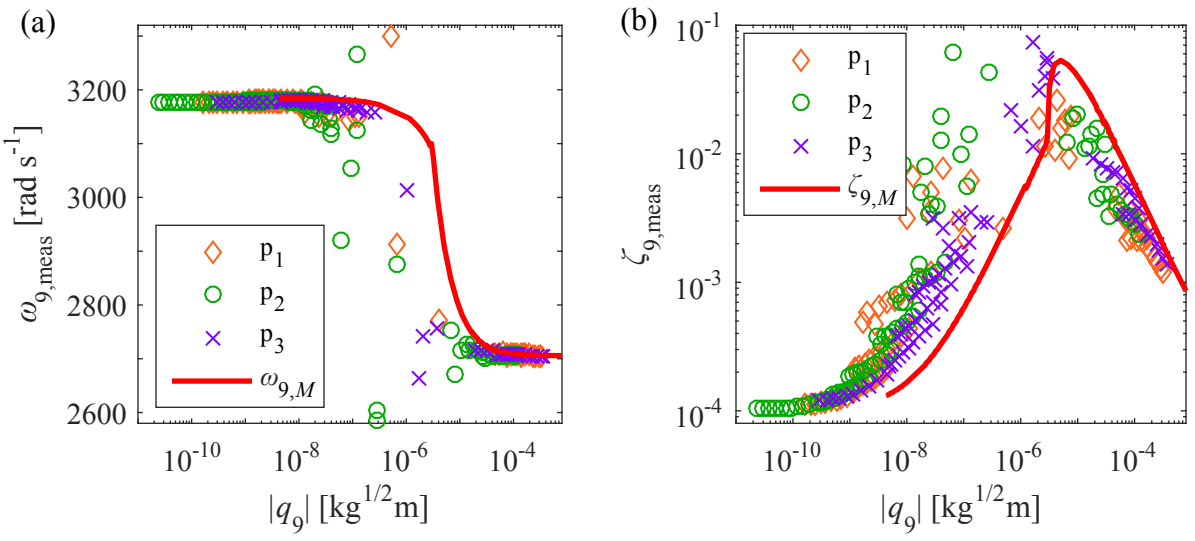

Figure 2.14: *The measured (a) natural frequency and (b) damping ratio versus modal displacement amplitude for the mode 9 response to discrete impulses on the Sumali beam system.*

capturing the damping in the system, both qualitatively and quantitatively, yet it is far simpler and more efficient to use than the fully coupled, nonlinear model.

2.4 Conclusion

The key assumption of the modal Iwan model is that the modes of a structure are uncoupled, which allows each mode to be treated independently from others when calculating nonlinearity. If such an assumption is true, then if follows that a modal Iwan model can be tuned by selectively exciting each mode in turn and studying the change in the natural frequency and effective damping with amplitude. In a general response, however, all modes in a structure are excited to varying extent, so this work examines the degree to which a modal Iwan model could still sufficiently capture the response of impulse-type excitations. Two numerical models – a three-mass system and the Sumali beam finite element model – were studied to identify the differences in the amplitude-dependent damping and natural frequency when the modes of the structure were selectively-excited, as compared to when the structure was excited with impulses at discrete points.

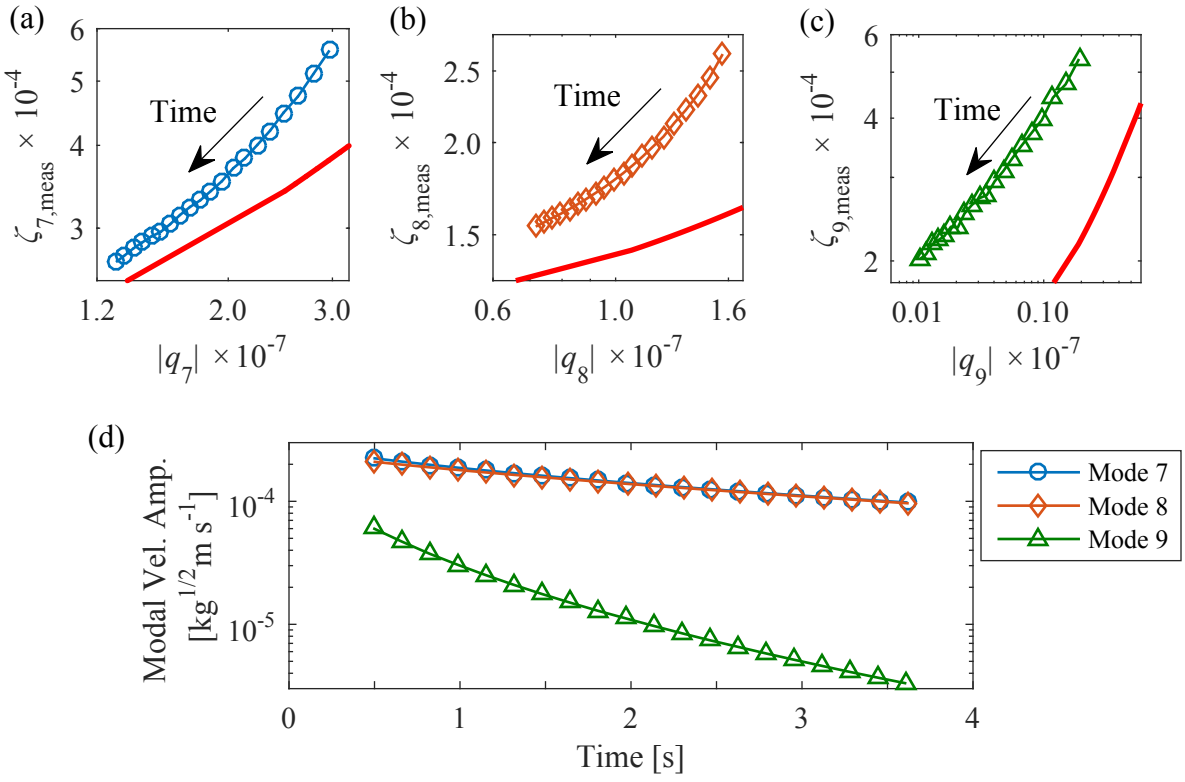

Figure 2.15: *Damping versus displacement amplitude for the (a) mode 7, (b) mode 8, and (c) mode 9 response to an impulse on the Sumali beam, and (d) time histories of the velocity amplitude for the three modes. The data are from simulation 6 in Table D.2, and are shown with the modal Iwan model curves ($\zeta_{r,M}$) as the thick red curve. The modal displacement amplitude units are kg$^{1/2}$ m.*

The results show that the modal Iwan models reproduce the effective natural frequency and damping of the system quite well provided that the mode in question is dominant in the response. For the two systems studied in this work, the effective damping produced by the modal Iwan model accurately fits that of the measured response if the measured response contains one dominant mode (as by selective excitation). If more than one mode is dominant, then the damping predicted by the modal Iwan models for the two systems typically exhibited less than 40% error in microslip and less than 60% error in macroslip. This error increases and can become as large as 400% if a mode is not dominant in the response, although in that case the response of such mode can probably be neglected. In many applications, these errors may

be acceptable considering the computational savings and easy parameter identification that the modal Iwan model provides.

The alternative is to use a different nonlinear model that accounts for coupling between the modes, such as one developed by Festjens, Chevallier, and Dion [42]. In this case, one would have to assess whether the increase in computational cost from a coupled model is worth relinquishing the simplicity of the uncoupled modal Iwan models, which in themselves still account for the change in modal damping and natural frequency with amplitude. Furthermore, to identify the parameters of such a model is not a trivial task because there are typically more unknown quantities than available data. Until a systematic methodology is developed by which a model can be identified that includes modal coupling, the modal Iwan approach may be the best available alternative.

Chapter 3

Updating Structural Models Containing Nonlinear Iwan Joints Using Quasi-Static Modal Analysis

Robert M. Lacayo, Matthew S. Allen

3.1 Introduction

Much of the uncertainty in finite element models for built-up structures comes from the interfaces (e.g. lap joints, riveted connections, press-fits, etc.). The nonlinearities they exhibit, in addition to an incomplete understanding of their underlying mechanisms, have made the modeling of interfaces challenging. See [5, 10, 49] for a review of these issues. Current modeling methods typically attribute joint nonlinearity to microslip friction [1, 12], or the partial slipping between the interfacing surfaces near the edges of contact. Hence, they employ a combination of discrete contact elements and friction elements located at the interfaces between otherwise linear finite element model components. For example, the Penalty and Lagrange methods are available for simulations in Abaqus [50], although they have never been thoroughly validated for structural dynamic simulations of bolted joints and, in any case, are too computationally expensive to be used to compute dynamic response. Harmonic balance methods have also been developed to compute a structure's frequency response using a harmonic representation of the nonlinear forces exerted by the friction elements [25, 26]. Other works have proposed 2-D zero-thickness elements [17, 19] or 3-D thin-layer elements [20, 51], both of which implement a tangential stick-slip condition in a continuum element. In order to model microslip behavior

accurately, such models typically require hundreds of friction elements per interface [52]. In dynamic simulations on models containing multiple joint interfaces, or in model updating procedures that require many simulations on different joint design iterations, the computational expense associated with so many nonlinear elements can become exorbitant.

It is certainly important to be able to develop high-fidelity models that can capture the physics occurring in a joint interface, especially for model verification purposes, but in many cases the objectives of the analysis may not require such detail. Joints are often only one small part of a complicated, assembled structure, and yet they are of interest because they have measurable nonlinear effects on the stress or vibration of the structure. Hence, the modeling of the mechanics occurring in the joint takes secondary importance compared to its contribution to the stiffness and energy dissipation of the structure as a whole. Various experimental studies have shown that the presence of one or more bolted joints induces a slight softening in the natural frequencies, yet a comparatively large growth in the damping, as the structure is excited to higher response amplitudes [3, 52, 53, 54, 55]. It seems logical, then, seek joint models that, when inserted into a global structural model, produce the correct amplitude-dependent response while simplifying the representation of the joint (and the associated computational cost) as much as possible.

As an example of such a simplification, the nonlinear degrees of freedom belonging to a joint model can be reduced by constructing a joint macro-model. As opposed to enforcing friction contact between individual nodes or element faces belonging to two opposing surfaces, those degrees of freedom can instead be tied (e.g. by multi-point constraints) to two ends of a single nonlinear element whose constitutive formulation is designed to reproduce microslip behavior internally. Such a modeling approach is the premise of Segalman's "whole-joint" model [27], and the nonlinear element is typically a hysteresis model such an Iwan [28, 31] or a Bouc-Wen [29] model. Unfortunately, no methods exist in literature that can help predict the parameters of these hysteresis elements based on joint geometry, surface roughness, material,

etc. Until this link is provided in research, a different approach is to take response measurements from a prototype structure and then solve the inverse problem to tune the parameters of a whole-joint model. This paper presents an improved method for doing this.

The validation of a nonlinear structural model against amplitude-dependent data is a well-established concept within the joints community. The typical practice has been to reproduce the instantaneous frequency and damping measured from a free-response ring-down (in transient methods) [32, 33, 56, 57] or to match the resonance peaks of a forced frequency response function taken at different excitation levels (for harmonic balance methods) [26, 52, 58]. Again, these works rely on simulating the dynamic response of the model in order to compare with experiments, and this is computationally expensive to implement within a model updating loop.

As an alternative, various studies by the contact mechanics community present many cases where jointed structures exhibit amplitude-dependent nonlinearities under quasi-static loading [59, 60, 61]. A quasi-static computation would certainly run faster than a dynamic one, but there has been a disconnect between the quasi-static behavior of joints and its effect on the dynamic response of the structure. A recent work by Festjens, Chevallier, and Dion [36] sought to close this gap by enforcing the modal motion of the entire structure as a boundary condition on a nonlinear, quasi-static model of the region near the joints. They proposed a method that could be used to adjust the mode shapes near the joint as amplitude increases in order to account for the slight softening that occurs in the joints during vibration. They evaluated their methodology by using it to predict the instantaneous natural frequency and damping ratio for the first mode of a finite element model of a cantilever beam containing a bolted joint near the fixed end. Their predictions were validated by comparing them to the transient response computed via integrating the full-order nonlinear finite element model, one that includes the preload in the fastener and the resulting Coulomb friction between the contacting surfaces. Their methodology was found to provide good estimates of the effective damping and natural frequency.

In this work, the quasi-static method introduced by Festjens et al. was modified to create a highly efficient tool, for extracting the amplitude-dependent natural frequency and damping from a finite element model containing discrete (localized) nonlinearities. The tool, here referred to as the method of quasi-static modal analysis (QSMA), was then used to update the nonlinear parameters of a model whose joints are represented by Iwan elements (which are found to have very good compatibility with the quasi-static method). Different from the work of Festjens, the updated model was then validated using transient measurements taken from a experimental test structure. The amplitude-dependent frequency and damping seen in those measurements were correlated to those of the finite element model using the proposed approach.

3.2 The Method of Quasi-Static Modal Analysis

The method of quasi-static modal analysis (QSMA) implemented in this work is a modification on the method developed by Festjens, Chevallier, and Dion [36]. In their work, Festjens et al. represent the motion of the domain surrounding a joint using a set of basis vectors. They treat the modal motion of the linear domain away from the joint as a boundary condition applied on the joint region. Then they solve for the static deflection of the joint by employing a convergence loop that updates the joint basis vectors with the amplitude of deflection. For this work, a similar effect is achieved by applying the shape of the linear normal modes as a static load distributed over the entire structure as opposed to just the boundary around the joint. Because a force is applied rather than a displacement, the structure is free to adjust quasi-statically in response to small changes in the stiffness of the joint. As a result, it becomes unnecessary to update the basis vectors associated with those small changes in the displacement field near the joint (provided that the joint does not slip completely). Joints are typically designed to retain their integrity, so even though this is a minor limitation it does simplify the method considerably.

3.2.1 Derivation of the Quasi-Static System

First consider a finite element model of a jointed structure in which the joints are represented with discrete, force-constitutive models. The unloaded equations of motion for such a system can be represented as

$$\mathbf{M}\ddot{\mathbf{u}} + \mathbf{K}\mathbf{u} + \mathbf{f}_J(\mathbf{u}) = \mathbf{0}, \tag{3.1}$$

where $\mathbf{M}$ and $\mathbf{K}$ are the mass and stiffness matrices, respectively, $\mathbf{u}$ and $\ddot{\mathbf{u}}$ are, accordingly, the displacement and acceleration vectors, and $\mathbf{f}_J$ is a vector of joint forces, which are assumed to depend nonlinearly on the displacements only. The system represented by Eq. (3.1) can be a full-order or a reduced-order system.

At small-displacement amplitudes about an equilibrium position $\mathbf{u}_0$, Eq. (3.1) can be represented by an equivalent linear system,

$$\mathbf{M}\ddot{\mathbf{u}} + \mathbf{K}_0\mathbf{u} = \mathbf{0}, \tag{3.2}$$

in which the full stiffness of the joint models remains intact. Here, $\mathbf{K}_0$ is the low-amplitude stiffness matrix at this equilibrium position, which can be computed through

$$\mathbf{K}_0 = \mathbf{K} + \left.\frac{\partial \mathbf{f}_J}{\partial \mathbf{u}}\right|_{\mathbf{u}_0}, \tag{3.3}$$

where $\partial \mathbf{f}_J / \partial \mathbf{u}$ is matrix of partial derivatives of $\mathbf{f}_J$ with respect to each coordinate of $\mathbf{u}$. A normal mode basis can be formed from this linearized system by solving the eigenvalue problem

$$\left(\mathbf{K}_0 + \omega_{0,r}^2 \mathbf{M}\right) \boldsymbol{\varphi}_r = \mathbf{0}. \tag{3.4}$$

This gives a set of natural angular frequencies $\omega_{0,r}$ and mode shapes $\boldsymbol{\varphi}_r$.

At this point, Festjens et al. [36] use matrix partitioning to divide Eq. (3.1) into a nonlinear

domain a near the joint and a linear domain b away from the joint,

$$\begin{bmatrix} \mathbf{M}_{aa} & \mathbf{M}_{ab} \\ \mathbf{M}_{ba} & \mathbf{M}_{bb} \end{bmatrix} \begin{bmatrix} \ddot{\mathbf{u}}_a \\ \ddot{\mathbf{u}}_b \end{bmatrix} + \begin{bmatrix} \mathbf{K}_{aa} & \mathbf{K}_{ab} \\ \mathbf{K}_{ba} & \mathbf{K}_{bb} \end{bmatrix} \begin{bmatrix} \mathbf{u}_a \\ \mathbf{u}_b \end{bmatrix} + \begin{bmatrix} \mathbf{f}_J(\mathbf{u}_a) \\ \mathbf{0} \end{bmatrix} = \begin{bmatrix} \mathbf{0} \\ \mathbf{0} \end{bmatrix}. \tag{3.5}$$

The vectors $\boldsymbol{\varphi}_r$ are similarly partitioned so that a single modal coordinate q_r can be represented in the physical space using the transformation $[\mathbf{u}_a, \mathbf{u}_b]^{\mathrm{T}} = [\boldsymbol{\varphi}_{ar}, \boldsymbol{\varphi}_{br}]^{\mathrm{T}} q_r$. With regards to the top set of Eq. (3.5) belonging to the joint domain, Festjens et al. neglect the mass coupling term ($\mathbf{M}_{ab} \approx \mathbf{0}$), and assume harmonic motion in the shape of the rth mode so that the substitutions $\mathbf{M}\ddot{\mathbf{u}}_a = -\omega_r^2 \mathbf{M}\boldsymbol{\varphi}_{ar} q_r$ and $\mathbf{u}_b = \boldsymbol{\varphi}_{br} q_r$ can be applied. After some rearranging, the top set of Eq. (3.5) becomes the quasi-static system

$$\mathbf{K}_{aa}\mathbf{u}_a + \mathbf{f}_J(\mathbf{u}_a) = \left(\omega_r^2 \mathbf{M}_{aa}\boldsymbol{\varphi}_{ar} - \mathbf{K}_{ab}\boldsymbol{\varphi}_{br}\right) q_r. \tag{3.6}$$

Note that the right-hand side contains two forcing terms: $\mathbf{M}_{aa}\boldsymbol{\varphi}_{ar} q_r$, which is the inertial force that the nonlinear domain a experiences due to vibration in mode r, and $\mathbf{K}_{ab}\boldsymbol{\varphi}_{br}$, the static force on domain a that results when domain b is deformed into the r mode shape. The coordinate q_r is a scalar multiplier that sets the level of the displacement in mode r and, hence, the force exerted on the joint. With the forcing now defined, Eq. (3.6) becomes a nonlinear quasi-static problem involving only the displacements $\mathbf{u}_a$ of the nodes near the joint. This equation can be solved at a reduced cost using standard approaches. In their formulation, Festjens et al. assume that $\boldsymbol{\varphi}_{br}$ remains unchanging with amplitude due to the weak nonlinearities exerted by the joint, but that $\boldsymbol{\varphi}_{ar}$ must be updated as q_r increases. Hence, they implement a convergence routine that simultaneously solves for the displacements $\boldsymbol{\varphi}_{br} = \mathbf{u}_b$ and $\boldsymbol{\varphi}_{ar} = \mathbf{u}_a$ as the strain energy of the system increases [36].

This work avoids the convergence routine by making a few modifications to Eq. (3.6). First, the joint domain is extended over the entire structure. This removes the boundary load

term $\mathbf{K}_{ab}$, and returns the joint domain partitions $\mathbf{K}_{aa}$, $\mathbf{M}_{aa}$, $\mathbf{u}_a$, and $\boldsymbol{\varphi}_{ar}$ to their full matrix representations $\mathbf{K}$, $\mathbf{M}$, $\mathbf{u}$, and $\boldsymbol{\varphi}_r$. Secondly, the linear mode shapes, $\boldsymbol{\varphi}_r$, are assumed to remain constant with amplitude. This assumption can be checked easily by examining the relative strength of other modes, and this work shows that superb results are still obtained using this assumption. Although the shape updating approach taken by Festjens et al. is more broadly valid, joints are typically designed to maintain their integrity, so their effect on the mode shapes of the structure should be minimal if not negligible while the joint remains in microslip. This is evidenced by the tiny shifts in the natural frequencies seen in various experimental studies [32, 33, 53, 55] in addition to the success of [32, 33, 57] in employing the linear modes assumption to characterize joint nonlinearity. Furthermore, one can check whether slip in the joints has caused the mode shapes to become statically coupled, as detailed in Section 3.3.3.

In addition, note that a unit modal force on mode r can be represented in the physical domain as $\mathbf{M}\boldsymbol{\varphi}_r$ (if $\boldsymbol{\varphi}_r$ is mass-normalized), which has the same form as the inertia term on the right-hand side of Eq. (3.6). Therefore, the load $\omega_r^2\mathbf{M}\boldsymbol{\varphi}_r q_r$ has the effect of distributing a force in the shape of mode r over the entire structure. For simplicity, the quantity $\omega_r^2 q_r$ is redefined as α to represent the load amplitude.

After applying the stated modifications, Eq. (3.6) reduces to

$$\mathbf{K}\mathbf{u} + \mathbf{f}_J(\mathbf{u}) = \alpha\mathbf{M}\boldsymbol{\varphi}_r, \tag{3.7}$$

from which $\mathbf{u}$ may be solved at different amplitude levels of α. Friction models are usually path-dependent, so α would be ramped incrementally from zero up to some maximum amplitude level of interest in a quasi-static simulation.

3.2.2 The Quasi-Static System for Unconstrained Models

It is often the case that the system of interest is suspended in an unconstrained, or free-free, configuration. Equation (3.7) therefore yields a singular result due to the rigid body modes, so the rigid body modes must be constrained beforehand. This is done using a null-space transformation on the system equations of motion. Let

$$\tilde{\mathbf{M}}\ddot{\tilde{\mathbf{u}}} + \tilde{\mathbf{K}}\tilde{\mathbf{u}} + \mathbf{f}_J(\tilde{\mathbf{u}}) = \mathbf{0} \tag{3.8}$$

represent the unconstrained equations of motion, and let $\tilde{\mathbf{\Phi}}_{\mathrm{R}}$ be the matrix composed of all rigid body mode shapes (mass-normalized) for this system. The coordinates $\tilde{\mathbf{q}}_{\mathrm{R}}$ governing these modes are constrained to zero, which establishes the relationship

$$\tilde{\mathbf{q}}_{\mathrm{R}} = \tilde{\mathbf{\Phi}}_{\mathrm{R}}^{\mathrm{T}}\tilde{\mathbf{M}}\tilde{\mathbf{u}} = \mathbf{0}. \tag{3.9}$$

The non-trivial solutions for $\tilde{\mathbf{u}}$ in Eq. (3.9) consist of all vectors belonging in the null-space of $\tilde{\mathbf{\Phi}}_{\mathrm{R}}^{\mathrm{T}}\tilde{\mathbf{M}}$. Let

$$\mathbf{L} = \mathrm{null}\left(\tilde{\mathbf{\Phi}}_{\mathrm{R}}^{\mathrm{T}}\tilde{\mathbf{M}}\right) \tag{3.10}$$

be the matrix of all basis vectors belonging to this null space. The transformation $\tilde{\mathbf{u}} = \mathbf{L}\mathbf{u}$ is then substituted into Eq. (3.8), and Eq. (3.8) is premultiplied by $\mathbf{L}^{\mathrm{T}}$ to obtain

$$\mathbf{M}\ddot{\mathbf{u}} + \mathbf{K}\mathbf{u} + \mathbf{L}^{\mathrm{T}}\mathbf{f}_J(\mathbf{L}\mathbf{u}) = \mathbf{0}, \tag{3.11}$$

where $\mathbf{M} = \mathbf{L}^{\mathrm{T}}\tilde{\mathbf{M}}\mathbf{L}$ and $\mathbf{K} = \mathbf{L}^{\mathrm{T}}\tilde{\mathbf{K}}\mathbf{L}$. Equation (3.11) replaces Eq. (3.1) for unconstrained systems, and the same formulation as given in Section 3.2.1 is followed to retrieve the quasi-static system. $\mathbf{K}_0$ becomes

$$\mathbf{K}_0 = \mathbf{K} + \mathbf{L}^{\mathrm{T}} \left.\frac{\partial \mathbf{f}_J}{\partial \mathbf{u}}\right|_{\mathbf{u}_0} \mathbf{L}, \tag{3.12}$$

and the final quasi-static system is

$$\mathbf{K}\mathbf{u} + \mathbf{L}^{\mathrm{T}}\mathbf{f}_J(\mathbf{L}\mathbf{u}) = \alpha\mathbf{M}\boldsymbol{\varphi}_r. \tag{3.13}$$

3.2.3 Computing Amplitude-Dependent Natural Frequency and Damping

After computing the quasi-static response $\mathbf{u}(\alpha)$ to a ramp up loading, $\mathbf{u}(\alpha)$ can be used to determine the amplitude-dependent natural frequency and damping for the mode applied to excite the structure. Festjens et al. rely on the satisfaction of Masing's rules [62] in order to determine from the ramp-up response the stiffness and energy dissipation of the joint models during cyclic loading. However, their final computation of the frequency and damping uses the updated mode shape deflections, which is not available under the formulation represented by Eq. (3.7). Hence, an alternative formulation is pursued whereby the Masing hypothesis is applied on the modal response as opposed to the joint response. The details of this new formulation are given in the following. It was also found that this formulation has a closed-form solution for damping in the case that the joints are represented by Iwan models, and the specifics for that are presented subsequently.

Frequency and Damping for General Joint Models

The original application of the Masing hypothesis was to derive a complete hysteresis loop for a single deformation mode in a plastic material based on its initial loading (virgin or "backbone") force-deflection curve [63]. Mechanical joints were found to exhibit similar hysteresis behavior that can be described by the Masing hypothesis [1, 27, 54], of which Festjens et al. took advantage in their formulation [36]. Here, the Masing hypothesis is assumed to hold for each mode of vibration. Specifically, the force-deflection hysteresis cycle for a mode of vibration is assumed symmetric about the origin whereby the following properties are assumed to

exist [62]:

- The "forward" part of the modal force-deflection curve is geometrically similar to the initial loading curve except that it has been magnified by a factor of 2 along the displacement and force axes and translated to terminate at the same point as the initial loading curve.
- The "reverse" part is the same as the forward part, but reflected along each of the displacement and force axes.

To retrieve the modal initial loading curve, Eq. (3.7) is solved for the case that the loading ramps up from zero to some maximum value, and the resulting response is mapped into the modal domain. Using mass-normalized mode shapes, the modal force is $F_r(\alpha) = \boldsymbol{\varphi}_r^{\mathrm{T}}\mathbf{M}\boldsymbol{\varphi}_r\alpha = \alpha$, and the displacement of mode r is $q_r(\alpha) = \boldsymbol{\varphi}_r^{\mathrm{T}}\mathbf{M}\mathbf{u}(\alpha)$. The modes that were not intentionally excited are also retained and can be used to assess the degree to which the modes are coupled at each load amplitude.

In a computational setting, both F_r and q_r are vectors composed of values associated with N number of discrete load steps α_j, where $j = 1..N$ is ordered from the lowest amplitude level of interest to the largest ($\alpha_N = \alpha_{\max}$). A modal force-deflection hysteresis loop is then constructed at each amplitude level using Masing's rules. Using MATLAB® vector indexing notation (where "$(1:j)$" represents the retrieval of entries 1 through j in order), the load vector for the forward force-deflection curve at amplitude level j is defined as

$$\hat{F}_1^{(j)} = 2F_r(1:j) - \alpha_j, \tag{3.14}$$

and the reverse curve is

$$\hat{F}_2^{(j)} = \alpha_j - 2F_r(j:1). \tag{3.15}$$

Note that "$(j:1)$" retrieves entries in reverse to account for the reflection about the force axis.

Lastly the displacements associated with the entries of both of these force-deflection curves is

$$\hat{q}^{(j)} = 2q_r(1:j) - q_r(\alpha_j). \tag{3.16}$$

An example hysteresis cycle computed with these curves is illustrated in Fig. 3.1. This hysteresis curve is used to estimate the stiffness and damping of mode r for the amplitude level in observance. Specifically, the slope of the secant line is used to define the stiffness (natural frequency) as

$$\hat{\omega}_r(\alpha_j) \triangleq \sqrt{\frac{\alpha_j}{q_r(\alpha_j)}}. \tag{3.17}$$

The area enclosed by the loop is the total energy dissipated $\hat{D}(\alpha_j)$ per modal cycle of vibration, which is readily obtained with trapezoidal integration of the difference $\hat{F}_1^{(j)} - \hat{F}_2^{(j)}$ with respect to $\hat{q}^{(j)}$. Then, using an energy balance between the dissipation and an equivalent viscous damper [57], the effective damping ratio can then be calculated as

$$\hat{\zeta}_r(\alpha_j) \triangleq \frac{\hat{D}(\alpha_j)}{2\pi\alpha_j q_r(\alpha_j)} \tag{3.18}$$

Equation (3.18) describes the equivalent damping contribution from the nonlinear joint elements in the finite element model, which theoretically tends to zero as amplitudes become small. The work of [32], however, shows that an experimentally-measured damping ratio approaches a constant non-zero asymptote at low-amplitudes, and it is presumed that this is the background material damping $\zeta_{0,r}$ for that mode. In general transient simulations, this low amplitude damping can be accounted for by adding a velocity term $\mathbf{C}\dot{\mathbf{u}}$ to the left side of Eq. (3.1). The damping matrix is formed as

$$\mathbf{C} = \mathbf{M}\mathbf{\Phi}\mathrm{diag}\left[2\zeta_{0,r}\omega_{0,r}\right]\mathbf{\Phi}^{\mathrm{T}}\mathbf{M}, \tag{3.19}$$

where $\mathbf{\Phi}$ is the matrix of all mode shapes $\boldsymbol{\varphi}_r$, and $\mathrm{diag}[\cdot]$ denotes a diagonal matrix where the

rth diagonal contains the entry listed in brackets. The quasi-static equation does not contain a velocity term, but this low-amplitude viscous damping can still be accounted for by adding its cyclic contribution to the modal energy dissipation [32]. In terms of amplitude-dependent damping, Eq. (3.18) becomes

$$\hat{\zeta}_r(\alpha_j) \triangleq \frac{\hat{D}(\alpha_j)}{2\pi\alpha_j q_r(\alpha_j)} + \zeta_{0,r} \tag{3.20}$$

In the case of light damping, the addition of this viscous damping should have negligible effect on $\hat{\omega}_r$.

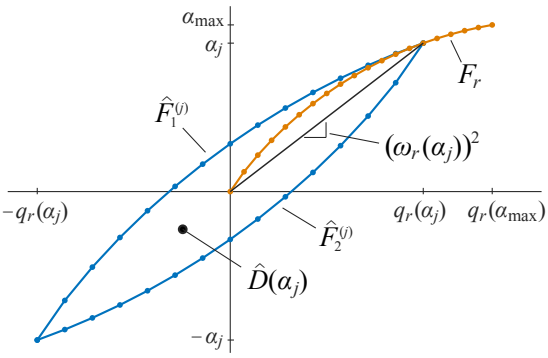

Figure 3.1: *A sample initial loading curve and a hysteresis loop derived from Masing's rules. The damping in typical structures is very light (i.e. 0.0001<ζ<0.05), so the hysteresis curve may show far less dissipation than that which is pictured here.*

Some points should be made regarding this method for computing the amplitude-dependent damping and frequency for a joint model. First, given the discretized representation of the hysteresis loop, the computation of the enclosed area for the first several amplitude levels would conceivably yield an erroneous estimation of the dissipation. In the authors' own studies, it was found that preceding the lowest amplitude level α_1 with at least 24 points, spaced uniformly between zero and α_1, would grant enough resolution in the hysteresis for a good approximation of the enclosed area. Naturally, this also means that a valid $\hat{\zeta}_r$ calculation begins at $j = 25$.

Secondly, the damping and frequency are computed by loading the structure in the shape of a single mode. In other words, the amplitude-dependence of these two properties is accurate

if the mode in question is dominant in the response, but it could be in error if more than one mode is excited at a time. The study by Lacayo et al. [57] investigates the extent of the error in damping and frequency arising from the modal coupling that a nonlinear joint model introduces. For discrete impulse excitations, they find that the amplitude-change in damping and frequency does not deviate much from the single-mode assumption if the mode in question shares dominance with another. However, the damping can be largely in error if the mode in question is weakly excited because, in that case, the energy dissipated by a joint is dominated by the motion of a different mode. The effects of modal coupling can also be seen in the experiments conducted for this work, and further details on the nature of this error in frequency and damping is given in Section 3.4.1. The important takeaway is that the method of QSMA presented here gives the most accurate results if a single mode is excited. Therefore, from a model updating standpoint, the joint models should ideally be tuned to response measurements that contain only one dominant mode, and this should be repeated simultaneously for as many other modes as measurable.

Frequency and Damping for Iwan Models

The method of quasi-static modal analysis (QSMA) relies on the satisfaction of the Masing hypothesis, and, hence, it is most accurate for nonlinear constitutive models that, in themselves, obey Masing's rules (i.e. the Masing models). As demonstrated in Fig. 3.1, Masing models have the property that each cycle of a steady-state hysteresis loop originates and terminates on the backbone curve [62]. Hence, the backbone curve for a Masing model can also be used to compute the tangential force exerted by a Masing model at a particular amplitude level in addition to its energy dissipation. If a closed-form solution for the backbone curve of a Masing model is available, then the computation of both the quasi-static response solution and the modal damping can be expedited as described below.

Masing models are typically a collection of ideal elastoplasic (Jenkins) elements. A good

example of such is the parallel-series distributed-element model developed by Iwan [28], referred to here as the Iwan model. As illustrated in Fig. 3.2, the Iwan model is a parallel-implementation of a large number of elastoplastic elements whose springs all have the same stiffness k, but whose Coulomb sliders have different slip forces. As the Iwan model displaces along u, it can be imagined that each slider begins to slip one after another as their slip thresholds are reached. In the case that the number of sliders is taken to infinity, Iwan used a statistical distribution function to describe the proportion of sliders that have a particular slip force. Segalman later reformulated Iwan's model to have the slip thresholds be defined in terms of the spring deflection limits ϕ, and accordingly redefined the distribution function $\rho(\phi)$ to describe the allotment of both the spring stiffness and slip strength [31]. Under Segalman's formulation, the force exerted by the Iwan model is a summation of the restoring forces exerted by each spring,

$$F_I(u) = \int_0^\infty \Gamma(u,\phi)\rho(\phi)\mathrm{d}\phi. \tag{3.21}$$

Here, the quantity $\rho(\phi)\mathrm{d}\phi$ assigns a differential stiffness to each spring, and Γ is the deflection of each spring, which is determined by the slip condition

$$\Gamma(u,\phi) = \begin{cases} u - x & \text{for } |u-x| < \phi \text{ (stick)}, \\ \phi & \text{for } |u-x| = \phi \text{ (slip)}, \end{cases} \tag{3.22}$$

where x is the position of the slider. Note that there is no mass between the spring and the Coulomb slider, so the slider instantly moves with u (i.e. $\dot{x} = \dot{u}$) when slip occurs and does not stick again until load reversal.

After an extensive testing campaign [2], Segalman found that jointed structures tend to exhibit energy dissipation that varies as a power of amplitude, so he defined the distribution

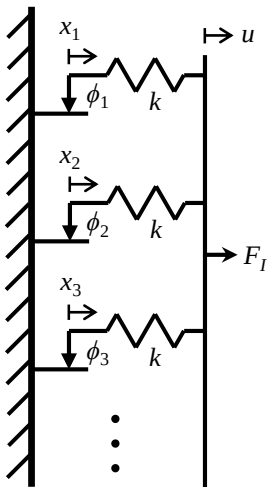

Figure 3.2: *Schematic of the parallel-series distributed-element (Iwan) model. In Segalman's formulation,* $k = 1$ *for all springs.*

function as follows [31]:

$$\rho(\phi) = R\phi^{\chi}\left[H(\phi) - H(\phi - \phi_{\max})\right] + S\delta(\phi - \phi_{\max}). \tag{3.23}$$

where $H(\cdot)$ is the Heaviside step function and $\delta(\cdot)$ is the Dirac delta. The $R\phi^{\chi}$ term, with $-1 < \chi < 0$, describes a truncated power-law decay function terminating at $\phi_{\max}$, which is the threshold of slip for the last slider (the point of macroslip). This decaying function effectively assigns a decreasing value of stiffness for springs that slip at a higher ϕ deflection. Parameter S is the strength of the Dirac delta function, and thus is the also the stiffness of the last spring to slip. Substituting Eq. (3.23) into Eq. (3.21) yields the force-constitutive function for the four-parameter Iwan model,

$$F_I(u) = \int_0^{\phi_{\max}} R\phi^{\chi}\Gamma(u,\phi)\mathrm{d}\phi + S\Gamma(u,\phi_{\max}). \tag{3.24}$$

In a general transient computation, the state x of every slider must be recorded in memory and passed between time steps, and this is difficult to implement for an infinite number of sliders. Therefore, Segalman presented a discretization of his four-parameter model for a limited

number of sliders, the details for which can be gleaned from [31].

For quasi-static simulations, on the other hand, Segalman's expressions for the backbone force-deflection curve and energy dissipation are sufficient to compute the response. If the four-parameter Iwan model is subjected to a monotonically-increasing load up to a displacement $u_0>0$, then Segalman computes the backbone curve as

$$F_0(u_0) = K_T u_0 - \frac{R u_0^{\chi+2}}{(\chi+2)(\chi+1)}, \tag{3.25}$$

where

$$K_T = \frac{R\phi_{\max}^{\chi+1}}{\chi+1} + S. \tag{3.26}$$

When the amplitude is very small, the four-parameter Iwan model exhibits a stiffness that is approximately K_T. Therefore, K_T is the linear stiffness of the Iwan model at unloaded equilibrium, and an equivalent linear system at low amplitude can be made by replacing the Iwan model with a linear spring having stiffness K_T. In effect, a four-parameter Iwan model that connects two degrees of freedom (DOF) in a finite element model would contribute the 2×2 stiffness matrix $[K_T, -K_T; -K_T, K_T]$ to $\partial\mathbf{f}_J/\partial\mathbf{u}$ in Eq. (3.3).

Furthermore, since F_0 describes the backbone curve of the four-parameter Iwan model, Eq. (3.25) can be used in the quasi-static computation (Eq. (3.7)) to retrieve its contribution to the nonlinear force $\mathbf{f}_J$. Again, if an Iwan element connects DOF a with DOF b, then the 2×1 vector contribution to $\mathbf{f}_J$ is $-F_0(u_b - u_a)$ for DOF a and $F_0(u_b - u_a)$ for DOF b. If $u_b - u_a$ is negative, then its absolute value is taken and the sign of F_0 is switched. The advantage of this computation is that the states of the sliders do not need to be tracked; the nonlinear force is then an analytical function of the modal displacement, so Eq. (3.7) can be solved inexpensively.

After computing the displacement solution from Eq. (3.7) for a particular load level α_j, the energy dissipated by the Iwan element at that load level can be computed. A closed-form

expression for dissipation per cycle is, again, provided by Segalman [31] as

$$E_{\text{dis}}(u_0) = \frac{4Ru_0^{\chi+3}}{(\chi+3)(\chi+2)}. \tag{3.27}$$

To connect this energy dissipation to $\hat{D}$, the energy dissipated per cycle of vibration in the rth mode, an assumption must be made that, because the structure is loaded in the shape of a particular mode, all of the energy dissipated by the Iwan element is allocated to that mode's energy dissipation ($\hat{D} = E_{\text{dis}}$). This assumption is clearly reasonable if the mode shapes do not change much with amplitude, but extent of modal coupling is a concern since the linear mode shapes never exactly match the amplitude-dependent mode shapes. Again, a check is provided in Section 3.3 to test this assumption.

As before, after obtaining the quasi-static solution, the displacements are mapped into the modal domain using $q_r(\alpha_j) = \boldsymbol{\varphi}_r^{\mathrm{T}}\mathbf{M}\mathbf{u}(\alpha_j)$, whereby the amplitude-dependent natural frequency is computed using Eq. (3.17). For the damping calculation, Eq. (3.27) can be used in place of $\hat{D}$ in Eq. (3.20). For models that contain more than one Iwan element, $\hat{D}$ is a summation of E_{dis} from every Iwan element. In this way, any numerical inaccuracies associated with trapezoidal integration of the modal hysteresis curve can be avoided, and the energy dissipation can be calculated accurately for all amplitude levels without having to precede α_1 with a couple dozen load steps.

3.3 Validation of QSMA with a Test Model

In this section, the method of QSMA is validated by examining the extent of the modal coupling that occurs when the linear mode shapes are used to excite a structure. The results in this section also demonstrate that the amplitude-dependent frequency and damping acquired through the quasi-static simulations are the same as those obtained from a dynamic simulation.

3.3.1 The Test Model

A finite element model (FEM) was set up as an exercise to validate the proposed methodology. The FEM, shown in Fig. 3.3, depicts the Brake-Reuß beam [55], a prismatic structure composed of two separate beam components that are bolted together in the middle of the structure. The three bolt assemblies were each modeled as a single, homogeneous mesh, even though each represents a bolt, nut, and washers. The beam components and bolt assemblies both consisted entirely of 8-node hexahedron elements formed with a linear-elastic, isotropic material model having Young's modulus 200 GPa and Poisson's ratio 0.29 (stainless steel). All mesh components were uncoupled from each other except at the interface between the top surface of component B, which was welded to the underside surface of the bolt-cap washers, and the bottom surface of component A was welded to the overside surface of the nut washers. These interfaces were welded as it was expected that these surfaces would not slip appreciably under dynamic loading [16]. An experimental Brake-Reuß beam was weighed, and its mass was divided by the volume of this finite element model to retrieve a mass density 7735 kg m^{-3}. The finite element model was taken to be in an unconstrained (free-free) configuration.

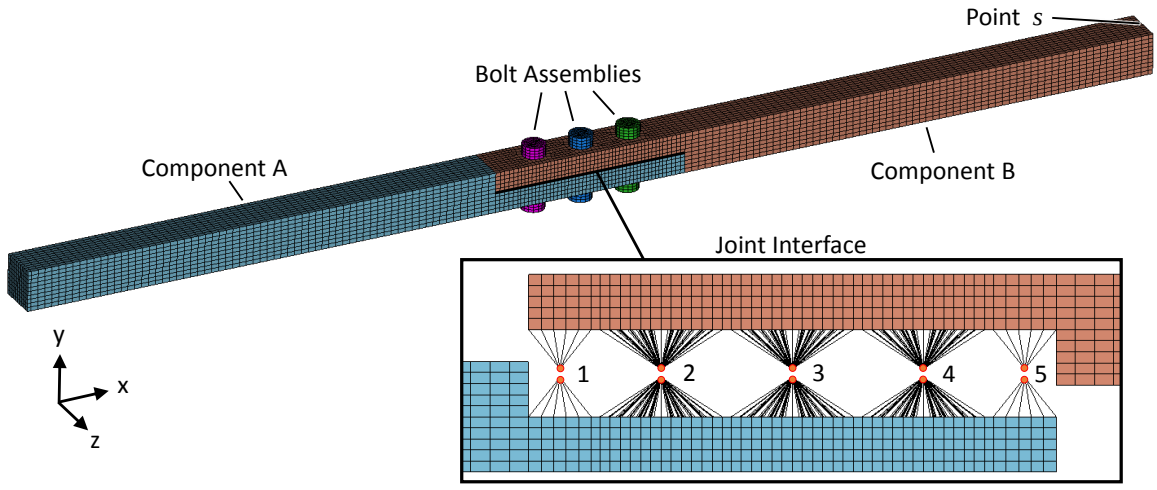

Figure 3.3: *Illustration of the Brake-Reuß beam finite element model with an exploded view of the joint interface representation.*

The whole-joint modeling approach introduced by Segalman [27] was used to represent the joint interface. In effect, the two interfacing surfaces were each divided into five contact patches: three of equal area surrounding each bolt hole, and two of a smaller area on each end of the interface. The nodes within each contact patch were then tied to a virtual node located at the centroid of each patch using an averaging multi-point constraint. That is, the six translation and rotation degrees of freedom (DOF) in each virtual node were constrained to be an average of the bulk motion of the DOF of all nodes within the representative contact patch. The virtual nodes associated with two opposing contact patches were then connected to each end of a "whole-joint model." For simplicity, all five whole-joint models consisted of a linear spring with stiffness 1×10^5 N mm^{-1} connecting the normal (y) direction DOF and a four-parameter Iwan element with parameters $\chi = -0.5$, $R = 2\times10^6$, $\phi_{\max} = 1.5\times10^{-4}$ mm, and $K_T = 1\times10^5$ N mm^{-1} connecting the axial (x) direction DOF. The linear spring represents the stiffness of the interface caused by the bolt pretension, and the Iwan element represents the friction associated with axial motion near each joint.

Prior to adding the linear spring and Iwan element to each of the five joints, the finite element model was reduced using the Craig-Bampton method [48] in order to decrease the computational time for simulation. In this reduction, the translational and rotational DOF belonging to the ten virtual nodes in the joint interface were kept as the "boundary" to create 60 constraint modes, and the rest of the structure was represented with fixed-interface modes. The first 24 fixed-interface modes were kept to include up to the 5th cantilevered bending mode in each beam component. The reduction produced a reduced-order mass matrix and stiffness matrix for the system, which contained 84 DOF total. These matrices were treated as $\hat{\mathbf{M}}$ and $\hat{\mathbf{K}}$ for the unconstrained system in Eq. (3.8). After constraining out the six rigid body modes using the process given in Section 3.2.2, a damping matrix $\mathbf{C}$ was then created through Eq. (3.19) by specifying $\zeta_{0,r} = 1\times10^{-4}$ for all modes.

3.3.2 The Transient Simulations and the Hilbert Transform Method

A set of transient simulations were conducted first on the reduced-order model of the Brake-Reuß beam in order to see how the modal frequency and damping of its modes change with amplitude. The system equations of motion given by Eq. (3.11) were set up to include a velocity and an external forcing term,

$$\mathbf{M}\ddot{\mathbf{u}} + \mathbf{C}\dot{\mathbf{u}} + \mathbf{K}\mathbf{u} + \mathbf{L}^{\mathrm{T}}\mathbf{f}_J(\mathbf{L}\mathbf{u}) = \mathbf{f}_{\mathrm{ext}}. \tag{3.28}$$

Here, the vector $\mathbf{f}_J$ is composed of Iwan element forces computed using the Segalman's discretized constitutive function (Eq. (3.24)), as was done in [57], since a means does not exist of doing so using the backbone force curve given by Eq. (3.25). The mode of interest was excited by defining the external force as an impact distributed over the entire structure in the shape of that mode,

$$\mathbf{f}_{\mathrm{ext}}(t) = \begin{cases} p\mathbf{M}\boldsymbol{\varphi}_r \sin\left(\omega_{0,r}t\right) & t < \pi/\omega_{0,r} \\ \mathbf{0} & t \geq \pi/\omega_{0,r}, \end{cases} \tag{3.29}$$

where p is a scalar multiplier to change the load amplitude. The modes of interest for this study were the first, second, and third xy-plane bending modes. Under the material properties and joint model parameters given in Section 3.3.1, these linear bending modes $\boldsymbol{\varphi}_r$ occur for $r = 1$, 3, and 7, respectively (recall that the rigid body modes were constrained out). Three separate simulations were conducted to excite these modes in turn, with $p = 100$ N for first bending and $p = 1240$ N for second and third bending. These load levels were chosen so as to displace the Iwan elements close to their macroslip limits, $\phi_{\max}$. For each simulation, Eq. (3.28) was integrated numerically using an average-acceleration Newmark method [46]. The velocity free-response of the system was then collected for a simulation period of 10 seconds. In effect, this is simulating the case where the velocity is measured at various points on the beam using a laser vibrometer. The velocity free-response was then mapped onto the mode r

coordinate using $\dot{q}_r(t) = \boldsymbol{\varphi}_r^{\mathrm{T}}\mathbf{M}\dot{\mathbf{u}}(t)$ (an ideal modal filter).

The instantaneous natural frequency and damping of this modal ring-down signal was extracted using the Hilbert transform method outlined in Feldman's "FREEVIB" paper [43]. The method essentially fits $\dot{q}_r(t)$ with a model of the form $\mathrm{Re}\left[A(t)\exp(\mathrm{i}\theta(t))\right]$, where $\mathrm{i} = \sqrt{-1}$, $A(t)$ is the instantaneous modal velocity amplitude, and $\theta(t)$ is the instantaneous phase. Linear vibration theory for free-response signals was then used to extract the equivalent natural frequency $\omega_r(t)$ and damping $\zeta_r(t)$ at each time instant [44], namely

$$\omega_r(t) \triangleq \frac{\mathrm{d}\theta(t)}{\mathrm{d}t}, \tag{3.30}$$

$$\zeta_r(t) \triangleq \frac{\gamma(t)}{\sqrt{\left(\omega_r(t)\right)^2 + \left(\gamma(t)\right)^2}}, \quad \gamma(t) = \tfrac{\mathrm{d}}{\mathrm{d}t}\left(\ln A(t)\right). \tag{3.31}$$

Although $A(t)$ describes modal velocity amplitude, [33] shows that the modal displacement amplitude $Q_r(t)$ can be retrieved through the relationship $A(t) = \omega_r(t)Q_r(t)$. If acceleration had been measured and denoted $A(t)$, then it could be related to modal displacement using $A(t) = \omega_r^2(t)Q_r(t)$. The reader is referred to the works of [32, 33, 57] for more details on various the techniques used to fit $\dot{q}_r(t)$ with the above given model form.

By implicit association, the $\omega_r(t)$ and $\zeta_r(t)$ obtained at each time instant were paired with the corresponding $Q_r(t)$ at the same time instant. This established the amplitude-dependent relationship for frequency and damping that were observed in transient ring-down simulations on the Brake-Reuß beam.

3.3.3 Comparison of Amplitude-Dependent Properties Between the Transient and Quasi-Static Simulations

The instantaneous frequency $\omega_r(t)$ and damping $\zeta_r(t)$ obtained from the transient free-response simulations in Section 3.3.2 were considered the truth properties against which $\hat{\omega}_r(\alpha_j)$ and

$\hat{\zeta}_r(\alpha_j)$ obtained from quasi-static modal analysis were validated. To retrieve $\hat{\omega}_1$ and $\hat{\zeta}_1$ for loading in the shape of the first bending mode $\boldsymbol{\varphi}_1$, the quasi-static response was first sought for each load step in a logarithmic ramp-up loading from $\alpha_1 = 10^{-1}$ to $\alpha_{\max} = 10^{2.2}$ for 50 steps. For each load step, the nonlinear force vector, $\mathbf{f}_J$ in Eq. (3.13), was constructed based on Eq. (3.25) (as explained in Section 3.2.3), and $\mathbf{u}$ was evaluated implicitly using a Newton step method.

After obtaining $\mathbf{u}$ for all load steps, the modal response for first bending was retrieved through $q_1(\alpha) = \boldsymbol{\varphi}_1^{\mathrm{T}}\mathbf{M}\mathbf{u}(\alpha)$. The natural frequency $\hat{\omega}_1(\alpha)$ was then calculated for every load step with Eq. (3.17). To get the damping ratio, $\mathbf{u}$ was first used to determine the deflections of all five Iwan elements at each load step, and those deflections were entered as u_0 in Eq. (3.27) to compute the energy dissipated per cycle for each Iwan element at that amplitude level. The modal dissipation $\hat{D}$ was then defined as the the sum of E_{dis} for all five Iwan elements. With $\zeta_{0,1}$ set as 1×10^{-4} in Section 3.3.2, the damping ratio $\hat{\zeta}_1(\alpha)$ was then computed for each load step using Eq. (3.20). Similarly to that done for the instantaneous modal properties in the transient simulations, $\hat{\omega}_1(\alpha)$ and $\hat{\zeta}_1(\alpha)$ at each load step were paired with $q_1(\alpha)$ of the corresponding load step to establish a relationship between these quasi-static modal properties and the amplitude of modal displacement.

For both the transient ring-down and the quasi-static simulations, the computed natural frequency and damping of the first bending mode are each plotted with respect to displacement amplitude in Fig. 3.4. To better comprehend the size of the modal displacement, the displacement axes in Fig. 3.4a and 3.4b refers to the amplitude of displacement at point s in Fig. 3.3 (the tip end of beam component B) when the Brake-Reuß beam deflects in the shape of first bending mode. Mathematically, This displacement was computed as $\boldsymbol{\Psi}_s\mathbf{L}\boldsymbol{\varphi}_1 q_1(\alpha)$ for the quasi-static response and as $\boldsymbol{\Psi}_s\mathbf{L}\boldsymbol{\varphi}_1 Q_1(t)$ for the instantaneous amplitude in the ring-down response. Here $\boldsymbol{\Psi}_s$ is the row in the Craig-Bampton transformation matrix [48] pertaining to point s. In both Fig. 3.4a and 3.4b, the frequency and damping versus amplitude curves for

the quasi-static response can be seen to agree very well with those of the ring-down response. There is small error towards the higher amplitudes (0.19% error in frequency and -12.6% error in damping at 3.2×10^{-3} mm), which could be attributed to the slight excitation of other modes in the transient simulations. This error can be seen to decrease in the descent to lower amplitudes. This result builds confidence that the method of QSMA produces the same trends in amplitude-dependent natural frequency and damping as seen in a dynamic simulation in the case that a finite element model contains Iwan elements.

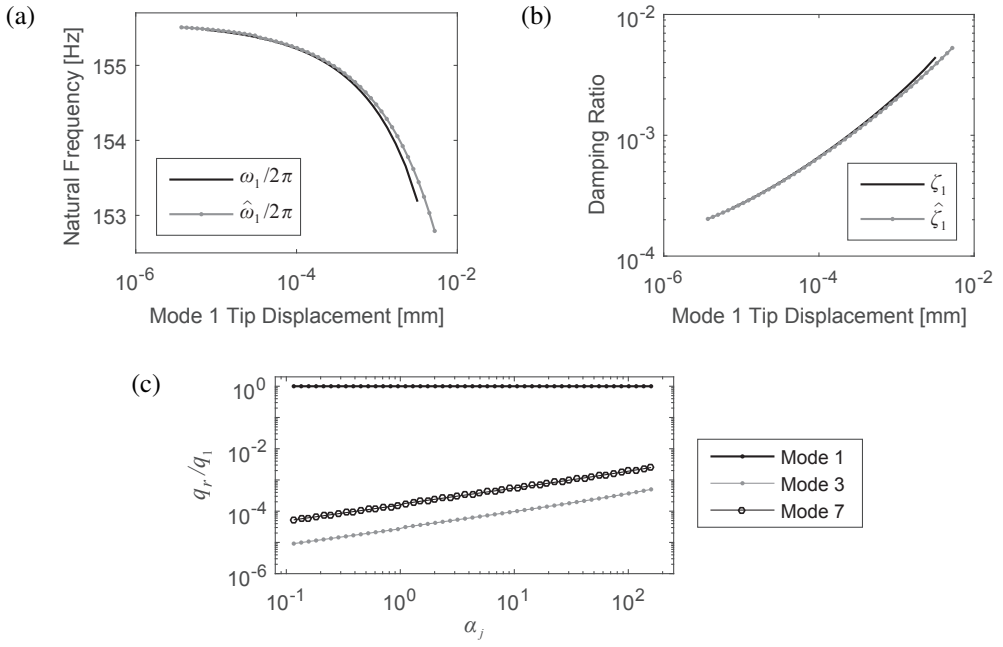

Figure 3.4: *Comparison between the ring-down response and QSMA in (a) natural frequency and (b) damping versus displacement amplitude of the right end of the Brake-Reuss beam undergoing first-bending deflection, and (c) the ratio of q_r/q_1 revealing the relative importance of each mode in the quasi-static response.*

The extent of modal coupling in quasi-static simulations was also examined by observing the relative importance of the other xy-plane bending modes in the response $\mathbf{u}(\alpha)$. This was done by first mapping $\mathbf{u}(\alpha)$ onto the first, second, and third bending modes using the transformation $q_r(\alpha) = \boldsymbol{\varphi}_r^{\mathrm{T}}\mathbf{M}\mathbf{u}(\alpha)$ for r = 1, 3, and 7, and then taking a ratio of q_r/q_1. Figure 3.4c plots these ratios versus the load step. The ratio of q_1/q_1 is shown for consistency, and its value is, of course, always 1. Here it can be seen that the relative importance of the second and third

bending modes gradually increases as the loading approaches the point of macroslip, but even then their displacement coordinates never exceed 3×10^{-3} of that of the first bending mode. Hence, the assumption that the first bending mode remains unchanging (even at higher, more nonlinear amplitudes) is strongly supported for this model.

The curves for frequency and damping versus modal amplitude were similarly obtained for the second and third bending modes by following the process outlined in the first and second paragraphs of this section. These plots are given in Appendix E. The transient and QSMA curves for mode 3 show a similar level of agreement as as those for mode 1. Likewise, the relative importance of modes 1 and 7 during the loading of mode 3 does not exceed 10^{-2}, which validates the unchanging mode assumption. On the other hand, the relative importance of mode 1 during mode 7 loading rises above 10% at the largest amplitude, which calls this assumption into question. Even then, the quasi-static frequency and damping curves for mode 7 still achieve remarkable agreement with those of the ring-down simulations, and this agreement is more important for the analysis in Section 3.4.

Most crucial is the reduction in the computational expense required to produce the natural frequency and damping versus amplitude curves. The transient free-response simulation performed in Section 3.3.2 for the first bending mode required 120 minutes to compute on a desktop machine with a 2.93 GHz processor. This time does not include the additional time spent on post-processing to filter the response into a modal signal and then apply the Hilbert transform method to extract the instantaneous frequency and damping from that modal signal. The Hilbert transform method also required active oversight from the user to ensure a reasonable fit of the amplitude and phase model to the simulated signal. In contrast, The first bending quasi-static simulations were completed *and* post-processed automatically in 0.15 seconds. The bulk of this reduction in time comes from a difference in the number of steps to complete (5 million time steps in transient versus 50 load steps in quasi-static), but this fact alone reflects an efficiency of data usage in the method of QSMA, where one load step by itself determines

the frequency and damping at that load level. The benefit of the massive reduction in the computational cost makes QSMA strongly preferable over the dynamic approach, especially considering that, in the case that Iwan elements are used, QSMA produces essentially the same amplitude-dependent frequency and damping trends as seen in a ring-down simulation.

3.4 Model Updating

As shown in Section 3.3.3, the method of quasi-static modal analysis (QSMA) provides an efficient means of accurately estimating the amplitude-dependent natural frequency and damping of the modes of a finite element model containing Iwan elements. The speed at which these properties can be computed make QSMA highly desirable as a tool for iterative model updating. Such capability is demonstrated in this section by updating the parameters of the five Iwan elements in the Brake-Reuß beam finite element model (FEM) so that the change in the frequency and damping seen in the model matches those of an experimental beam.

With regards to the test data that will serve as the target for comparison, the approach taken here is the experimental counterpart to Section 3.3.2. In essence, the high-level impact response taken of the experimental Brake-Reuß beam is filtered into its component modal signals, and then the Hilbert transform method is applied to retrieve the instantaneous frequency and damping of each mode. Before the response signal can be filtered, however, the mode shapes of the beam must be extracted. Hence the testing was divided into two phases, a low-level response test phase to retrieve mode shapes, and a high-level test phase to obtain amplitude-dependent properties.

3.4.1 The Experimental Measurements

An experimental Brake-Reuß beam was assembled and tested to retrieve data on its modes at low-amplitude in addition to its free response to high-level impacts. The beam was suspended on each end in a free-free configuration and outfitted with twelve accelerometers positioned

along its center axis so as to achieve good observability of its xy-plane bending modes. A more detailed description of the assembly and test setup is given in Appendix F.

The low-amplitude mode shapes of the experimental beam were first extracted through low-level hammer impact tests. In sum, the response signals of the twelve accelerometers were recorded after a 3 N impact force was applied in the y-direction at point s. After three such tests, the acceleration response and input force spectra were processed to form an H1 frequency response function [64], to which a modal model was fitted. Again, more details on the collection and processing of the accelerometer data can be found in Appendix F. Ultimately, the mode shapes for the first (175.04 Hz), second (589.75 Hz), third (1196.2 Hz), and fourth (1661.5 Hz) xy-plane bending modes were discerned. Their mode shapes are illustrated in Fig. 3.5.

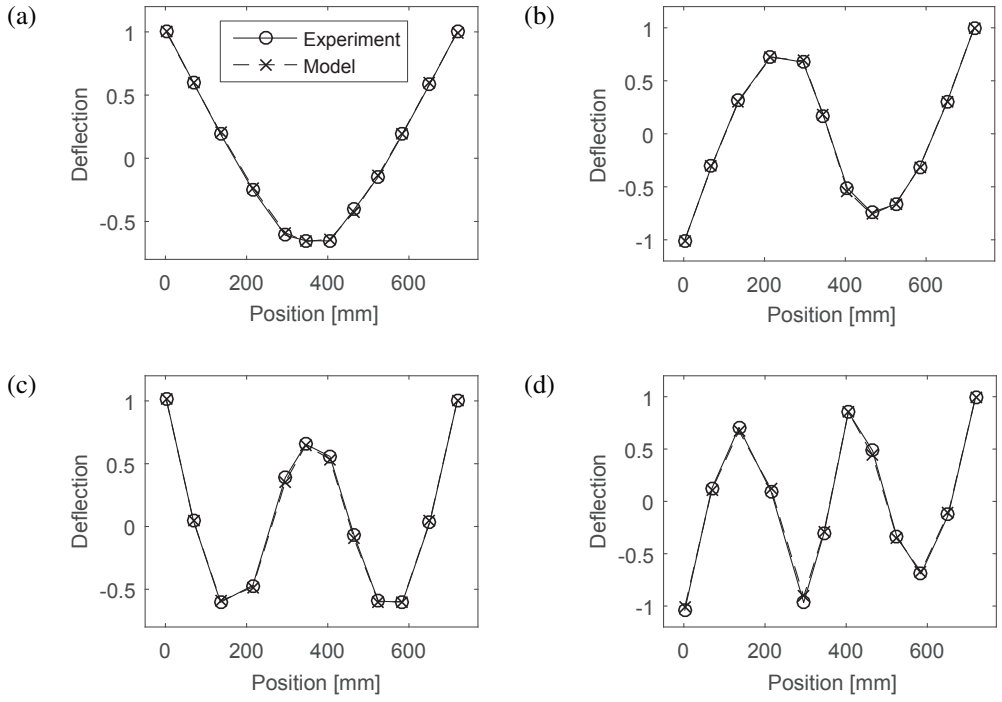

Figure 3.5: *Comparison of the experimentally measured mode shapes, and those the linear finite element model after updating in Section 3.4.2, for the (a) first, (b) second, (c) third, and (d) fourth bending modes. Accelerometer positions are measured relative to the left end of beam component A.*

Following the low-amplitude impact tests, a series of high-amplitude impact tests were

conducted to examine the trends in amplitude-dependent frequency and damping of the four bending modes. To maintain consistency with the method of QSMA and its loading of the structure in the shape of a single mode, the experimental beam was likewise excited so that one mode was dominant in the response. Unlike in simulation, it is difficult to distribute an impact force over the entire test beam in the shape of a mode, so instead the impacts where applied at carefully chosen points on the beam that excite one of the bending modes more significantly than others. The exact points and impact force levels are detailed in Appendix F. After measuring the free response decay, the response was filtered into its component modal signals using the mode shapes acquired from the low-level tests. An amplitude and phase model was then fitted to the dominant modal signal by following the Hilbert transform method outlined in Section 3.3.2. The instantaneous natural frequency and damping of each dominant mode was then extracted.

The experimental curves for the natural frequency and damping versus displacement amplitude are shown in Fig. 3.6. Here, the first, second, third, and fourth bending modes are referred to as modes 1, 3, 7, and 8, respectively, as shorthand and for consistency with the finite element model mode shapes. The data for mode 1 came from impact test case 2 (described in Appendix F), in which the beam was struck at the nodal location that suppresses the excitation of mode 3. The data for modes 3 and 7 come from test case 6, where the beam was struck at the nodal location for mode 1. The mode 1 signal in test case 2 was found to have a greatest amplitude relative to the strengths of other modes. The mode 3 signal in test case 6 is likewise the most dominant. Mode 7, accordingly, is not the most dominant in test 6, but its acceleration signal starts off almost 2 orders of magnitude higher than that for mode 1; this trait cannot be said for any of the other test cases. Unfortunately, mode 8 was so weakly excited in all test cases that noise from other modes was significant enough to contaminate its signal. This resulted in highly distorted frequency and damping versus amplitude curves, as demonstrated in Fig. 3.6g and 3.6h (data from test case 10). The effects of noise can also be seen towards the lower

amplitudes in the curves for the first three modes, too.

Although the method of QSMA provides indirect motivation for assuring that the reference data for comparison consists only of the modal signal in question, some context should be given as to why modal dominance is important in experiment as well. Juxtaposed with the curves from tests 2 and 6 in Fig. 3.6 are the instantaneous frequency and damping from the modal signals in test case 10. In test case 10, the impact was applied at point s, and this resulted in shared dominance of the acceleration signals from modes 1 and 3 with secondary importance of mode 7. It can be seen from the figure that shared dominance (or non-dominance, accordingly) correlates to an apparent decrease in the natural frequency and an increase in the damping as compared to their mode-dominant counterparts.

The discrepancy in frequency and damping was explained in [57] as a consequence of modal coupling; since the flexure of the joint can be considered a superposition of the modal displacements, the stiffness and energy dissipated by the joint is "activated" to a higher amplitude than would be expected from the amplitude of the mode in question by itself. Hence, although a particular mode's amplitude may not change in a response, that mode's frequency and damping can still decrease and increase, respectively, if signals from other modes are added to the response. Thus, to ensure the pairing of the correct frequency and damping with a certain amplitude, the experimental signals should ideally consist of a single mode in order to be consistent with QSMA. With the given data, this criterion is satisfied within reasonable error for modes 1 and 3, but not so for modes 7 and 8. The mode 7 frequency and damping curves that are depicted as "mode-dominant" in Fig. 3.6 are actually just additional examples of non-dominant curves similar to those from test case 10, but they are closer to the true mode-dominant curves.

Even if the modal frequency and damping versus amplitude curves are not mode-dominant, they are still useful. Towards the lower amplitudes, both dominant and non-dominant curves can be seen to approach the same asymptote. Hence, even for modes 7 and 8, the low-amplitude

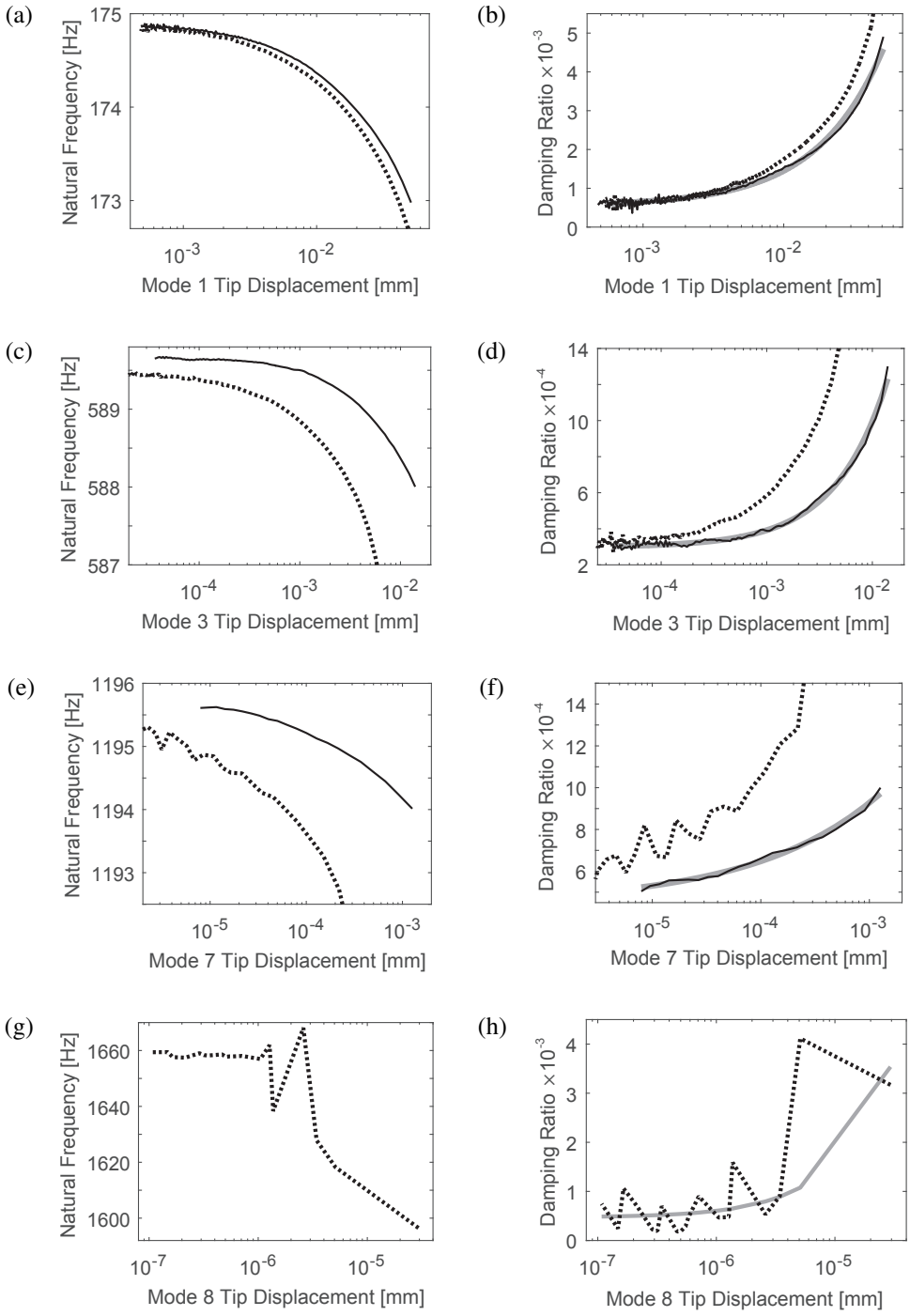

Figure 3.6: *Plots of the experimentally-derived instantaneous (a,c,e,g) natural frequency and (b,d,f,h) damping versus modal displacement amplitude in the (a,b) first, (c,d) second, (e,f) third, and (g,h) fourth bending modes of the Brake-Reuß beam. Solid lines originate from test data in which the mode in question is dominant, and dotted lines are from test case 10 (see Appendix F). The thick gray lines in (b,d,f,h) are power-law fits (Eq. (3.32)) used to estimate the low-amplitude damping ratio.*

natural frequency and damping ratio can be deduced from the amplitude plots given in Fig. 3.6. The measured low-amplitude natural frequencies were the target for the preliminary updating performed on the Brake-Reuß beam finite element model. Furthermore, since the nonlinear model updating (Section 3.4.3) used the mode-dominant data as the target reference, then the response case that exhibited modal coupling (test 10) served as the reference to validate the updated model.

3.4.2 Low-Amplitude Model Updating

Before the parameters of the Iwan elements were tuned to fit the experimental amplitude-dependent damping and frequency, the Brake-Reuß beam model was first updated to ensure that it approached the low-amplitude asymptote in the natural frequencies for all four bending modes. The same finite element model described in Section 3.3.1 was used here, except that all the Iwan elements had been replaced with linear springs. For an Iwan model, this substitution is equivalent to "locking" the Coulomb slider in all elastoplastic elements (i.e. they never slip), so the stiffness exhibited by the model is always its K_T parameter. Thus, after completing this initial updating, the K_T parameter for all Iwan elements was deduced.

Since the model was linear, an industry-standard optimization tool was used to update the natural frequencies and mode shapes of the finite element model. The target natural frequencies and mode shapes were the same as those extracted from the fitting of the mode shapes in the low-amplitude tests. The design variables were the Young's modulus (initially set to 200 GPa), and the stiffness of the x-direction and y-direction springs in all five joints (a total of ten springs all initially set to 1×10^5 N mm^{-1}). Since there were eight target elements (mode shapes and frequencies for four modes) and eleven total design variables, the problem was underdetermined, so some springs were constrained to be the same as others based on the spatial symmetry of the bending modes. Specifically, the x and y springs for joint 5 (refer Fig. 3.3) were constrained to be the same as those for joint 1, and likewise those for joint 4 were

made the same as those for joint 2. This reduced the number of unique design variables to seven, creating an overdetermined problem and, thus, making problem amenable to a least-squares solution.

The updated parameters are listed in Table 3.1, and the model natural frequencies are given in Table 3.2. The model mode shapes are compared with those of experiment in Fig. 3.5. Both the linear natural frequencies and mode shapes from the model achieved superb agreement with those of experiment.

Table 3.1: *Updated linear parameters for the Brake-Reuß beam finite element model.*

Parameter	Value
Young's Modulus	195.40 GPa
Joints 1, 5 y-spring	4.0709×10^6 N mm^{-1}
Joints 1, 5 x-spring	5.7609×10^5 N mm^{-1}
Joints 2, 4 y-spring	5.4855×10^4 N mm^{-1}
Joints 2, 4 x-spring	1.0865×10^5 N mm^{-1}
Joint 3 y-spring	1.1521×10^5 N mm^{-1}
Joint 3 x-spring	3.7345×10^5 N mm^{-1}

Table 3.2: *Comparison between model and experimental natural frequencies. Error values are relative to experiment.*

Mode	Natural Frequency [Hz]		Error
	Experiment	Model	
1	175.04	175.06	0.009%
3	589.75	589.99	0.040%
7	1196.2	1196.0	−0.016%
8	1661.5	1651.6	−0.60%

In preparation for the nonlinear model updating, the low-amplitude, background damping ratios $\zeta_{0,r}$ were deduced from the damping versus amplitude curves of each mode. This was done by fitting to each damping curve a modal power-law model added to a constant, similar to Eq. (3.20). Since Eq. (3.27) shows that the energy dissipated by an Iwan model varies with amplitude to the power of $\chi + 3$, and since Eq. (3.20) reveals that damping is proportional to dissipation divided by the square of amplitude (q_r varies almost linearly with α if modal

stiffness ω_r^2 hardly changes), then an appropriate form to fit modal damping is

$$\bar{\zeta}_r(Q_r) = \bar{c}_1 Q_r^{\bar{\chi}+1} + \bar{\zeta}_{0,r}, \tag{3.32}$$

where the overbar variables denote estimated quantities. Here, $\bar{\zeta}_{0,r}$ is the estimated background damping ratio of mode r. Futhermore, if the same value for $\bar{\chi}$ can be fitted for all modes (or at least modes 1 and 3 with the given data), then it strongly suggests that the χ parameter for all Iwan elements takes on this same value.

A least-squares optimization tool was used to fit Eq. (3.32) to each mode-dominant damping curve (and the test 10 curve for mode 8) in Fig. 3.6. The resulting estimated quantities are listed in Table 3.3, and the fits are illustrated by the gray lines in Fig. 3.6. Unfortunately, the $\bar{\chi}$ parameter for modes 1 and 3 are not similar enough to assume with certainty that all Iwan elements have the same χ value, but the values are close enough to suggest that the χ values may be in the vicinity of -0.10. The values listed in the $\bar{\zeta}_{0,r}$ column were used for $\zeta_{0,r}$ in Eq. (3.20) during the nonlinear model updating described in the next section.

Table 3.3: *Parameter values for the damping power-law model in each mode.*

Mode	$\bar{c}_1$	$\bar{\chi}$	$\bar{\zeta}_{0,r}$
1	0.0621	-0.082	5.37×10^{-4}
3	0.0388	-0.127	2.99×10^{-4}
7	0.0065	-0.623	4.46×10^{-4}
8	47.9	-0.075	4.70×10^{-4}

3.4.3 Updating the Nonlinear Model with QSMA

Having updated the linear finite element model to exhibit the correct natural frequencies and damping ratios at low-amplitude, the Iwan elements were then restored, and their parameters were tuned so as to reproduce the change in natural frequency and damping at higher amplitudes. Here, the method of QSMA fulfills the critical role of quickly producing the natural frequency and damping versus amplitude curves associated with the finite element model so

that they can be compared with those of experiment. Thus, through an iterative process, the parameters of the Iwan elements can be tuned to minimize the discrepancy between the curves from experiment and those of the model. However, past works have found that it is difficult to tune each element individually since the parameters have unintuitive repercussions on the frequency and damping of the structure [2, 57, 34, 65]. Hence, rather than attempt to manually manipulate the parameters, a Monte Carlo study was conducted.

The objective of the Monte Carlo study was to seek a set of parameters that minimizes the error in the frequency and damping curves produced from the model relative to those of experiment. To do this, many trial simulations were conducted in which the parameters of each Iwan element were selected randomly from a plausible parameter space. The quasi-static frequency and damping versus amplitude curves for the first three bending modes were then computed for the sampled parameter set, and their errors relative to the experimental curves were calculated. The best set of sampled parameters would naturally stem from the trial that produces the least error in both frequency and damping for all modes.

Determining the sampling space

Each Iwan element had four parameters, χ, $\phi_{\max}$, R, and K_T, to determine. Similar the linear model, the parameters of the Iwan element from joint 5 (refer Fig. 3.3) were taken to be equivalent to those of joint 1, and likewise for joints 4 and 2, in order to give three unique sets of nonlinear parameters.

From the linear updating in Section 3.4.2, the K_T parameter for each Iwan element was already deduced. This value is given by the stiffness value shown in Table 3.1 by the appropriate x-direction spring that replaced the Iwan element in the linear model.

The rest of the parameters were sampled randomly, but some constraints were applied on the possible values they could take on. The χ parameter was sampled linearly between -1 and 0 as this was the acceptable range originally defined by Segalman for the four-parameter

Iwan model [31]. The $\phi_{\max}$ parameter determines the threshold that the element must displace before macroslip is reached (i.e. when the last slider slips). Since the joints were assumed to remain in microslip, the lower limit of this value was thus determined by the displacement of each Iwan element at the maximum load of interest, $\alpha_{\max}$, for each mode. First, the unknown parameters of all Iwan elements were initially set to χ=$-$0.1, R=1$\times$10^7, and $\phi_{\max}$=1$\times$10^{-2} mm. Then, the range of loading amplitudes α was determined for each mode by iteratively changing the upper and lower bounds, α_1 and $\alpha_{\max}$, until the range of simulated quasi-static modal displacement solutions, $q_r(\alpha_j)$, spanned the range of the experimental displacement amplitudes given by the appropriate mode in Fig. 3.6. The values for the upper and lower bounds of α that were determined for each mode are given in Table 3.4. Afterwards, the quasi-static deflection of each Iwan element was then examined for when the finite element model was loaded in the shape of each mode under $\alpha_{\max}$. Then, to assure that no joint goes into macroslip, the $\phi_{\max}$ parameter for each Iwan element was chosen to be larger than the maximum displacement observed in any of the four bending modes. For joints 1 and 5, the lower bound of $\phi_{\max}$ was found to be 6$\times$10^{-4} mm, and the lower bound was found to be 4$\times$10^{-4} mm for joints 2, 3, and 4.

Table 3.4: *Loading limits on the quasi-static simulations in the Monte Carlo study.*

Mode	α_1	$\alpha_{\max}$
1	$10^{1.25}$	$10^{3.30}$
3	$10^{1.15}$	$10^{3.85}$
7	$10^{1.10}$	$10^{3.40}$

The procedure above provides an estimate of the lower bound on $\phi_{\max}$ for each joint, but to define an upper bound is not so straightforward. The exact threshold for macroslip in each Iwan element is unknown since it is difficult to glean evidence of macroslip from the experimental ring-down response. It could be that the response amplitude was no where near the threshold for macroslip, but it is also possible that the amplitude was at the cusp of macroslip. However, if the value used for $\phi_{\max}$ is too high, the model will behave nearly linearly over the observed

range of amplitudes. Therefore, in the Monte Carlo study, the $\phi_{\max}$ parameter was sampled logarithmically between 1 to 10 times the minimum values given above.

The final parameter R has a maximum value imposed by the dependent parameter S in Segalman's four-parameter formulation given by Eq. (3.23). The parameter S effectively defines the stiffness of the very last slider to slip in the Iwan model, so its value must remain positive. Therefore, according to the relationship between Segalman's four parameters and K_T, as given by Eq. (3.26), the upper limit imposed on R must be

$$R_{\max} = \frac{(\chi+1)K_T}{\phi_{\max}^{\chi+1}}. \tag{3.33}$$

Since χ and $\phi_{\max}$ are sampled randomly, $R_{\max}$ also changes accordingly and must be recomputed with each trial. Parameter R must also remain positive, which makes 0 the lowest limit. However, too low a value for R effectively makes the Iwan element behave linearly, so instead R was sampled logarithmically between $\frac{1}{10}$ and 1 times $R_{\max}$.

The Monte Carlo simulations

A batch of 100,000 randomly-sampled parameter sets were generated for the Monte Carlo analysis. For each parameter set, the method of QSMA given in Section 3.2 was applied to compute the natural frequency, $\hat{\omega}_r$ (Eq. (3.17)), and damping ratio, $\hat{\zeta}_r$ (Eq. (3.20)), as implicit functions of modal displacement amplitude, q_r, in each of the first, second and third bending modes. In other words, three sets of frequency and damping versus amplitude curves were computed pertaining to the first three bending modes of the finite element model. The quasi-static frequency and damping curves were then interpolated linearly to obtain values at the same amplitudes, Q_r, that were obtained for each mode in the mode-dominant measurements shown in Fig. 3.6. In this way the experimental frequency and damping, ω_r and ζ_r, could be readily compared with those of the model at the same amplitude.

The error in frequency and damping between model and experiment was then computed

using a weighted root-mean-square deviation formula. The first bending (r=1), second bending (r=3), and third bending (r=7) frequency and damping curves each consisted of N_r discrete points, and were weighted as W_r, so the root-mean-square deviation was computed as

$$\mathrm{RMSD} = \sqrt{\frac{W_1}{N_1}\sum^{N_1}\left(\hat{y}_1 - y_1\right)^2 + \frac{W_3}{N_3}\sum^{N_3}\left(\hat{y}_3 - y_3\right)^2 + \frac{W_7}{N_7}\sum^{N_7}\left(\hat{y}_7 - y_7\right)^2} \tag{3.34}$$

where y_r is a placeholder for the experimental damping or frequency values, and $\hat{y}_r$ are the corresponding interpolated values from QSMA. Since the experimental frequency and damping curves for the first and second bending modes were derived from response measurements in which their corresponding modal signals were the most dominant (i.e. the "mode-dominant" curves in Fig. 3.6), these modes were given full weighting, $W_1 = w_W = 1$. The same could not be said of the third bending mode; its modal signal shares dominance with other modes in the raw test data, so it was given a weighting of $W_3 = 0.1$.

On the matter of frequency error, given that the amount of frequency shift from low to high amplitude is so small compared to its absolute value at low amplitude (little more than 1% decrease for first bending), there is little gain in using the absolute value of frequency as the measure for error. Furthermore, the error in absolute frequency is mainly dependent on the linear optimization that was performed in Section 3.4.2, and, although a good fit was achieved for this model from that optimization, such a circumstance may not be possible in models of other structures. Any residual error in the absolute value of frequency from linear updating would thus skew the error for this nonlinear updating portion. A more sensible metric is to compute the error in the frequency shift with amplitude, or the amount that the natural frequency changes relative to its value at the lowest amplitude of interest. In this way, the geometry of the frequency versus amplitude curve is maintained (if a good fit is achieved), so the residual frequency error remains constant over all amplitude. Another reason for this rationale is that the error in the linear natural frequency could potentially be a function of

different parameters other than those which affect the frequency shift. Once the nonlinear shift is reproduced, one could presumably find other parameters to change the model so that the linear natural frequency improves. For this work, the RMSD in frequency shift was computed for the 100,000 trials in addition to the RMSD in damping.

After completing all 100,000 trials (a feat that required only 10.7 hours to compute on a desktop machine!), the RMSD in frequency shift for each trial was plotted with respect to the corresponding RMSD in damping ratio in Fig. 3.7. As expected, the vast majority of the trails used a sub-optimal set of parameters, but it is also interesting to note that no trial produced a minimum in both frequency shift and damping. In fact, a Pareto front seems to be present in the lower left quadrant of Fig. 3.7, which would suggest that the model is limited by a trade-off between matching either the frequency shift or the damping, but not both.

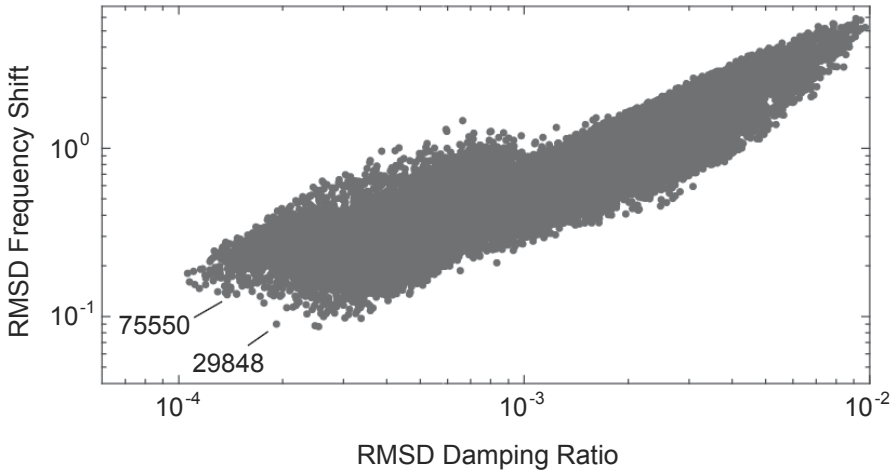

Figure 3.7: *Plot of RMSD frequency shift versus RMSD damping ratio for the 100,000 Iwan element parameter trials. Each dot represents the results of a trial. Trial numbers 29848 and 75550 are marked.*

Fortunately, it was found that the significance of any discrepancy in frequency shift and damping arising from this trade-off is moot for most of these Pareto-optimal trials. The frequency shift and damping versus amplitude results for trial numbers 29848 and 75550 in particular shown in Fig. 3.8. Both of these trials produced results that can be considered to lie on (or close to) the Pareto front, but trial 29848 produced a lower RMSD in frequency shift

whereas a lower RMSD in damping was achieved in trial 75550. Yet, despite the implication of the difference in RMSD values (which in themselves are small to begin with), both of these trials fit the test frequency shift and damping remarkably well except in third bending. Again, the test data for third bending stemmed from response measurements where the third bending modal signal was not the most dominant signal, so the discrepancy seen between the test and trial curves of Fig. 3.8e and 3.8f should not be a matter of concern. In fact, a truly mode-dominant signal would result in a smaller change in both natural frequency and damping with amplitude than given by the test curve, so the curves for both trials would be good candidate mode-dominant curves for third bending.

In absence of other selection criteria or reference data, it would be difficult to decide which of the two trials (or even any of the other Pareto-optimal trials) better captures the experimental data for the third bending mode. For the sake of moving forward to the validation step, the parameters used in trial 29848 were chosen to represent the tuned model because they produced a greater shift in the damping and natural frequency for third bending, which implies that it is easier to excite nonlinearity from the Iwan elements with this parameter set than with those of trial 75550. The parameters used for trial 29848 are listed in Table 3.5.

Table 3.5: *The tuned Iwan element parameters for the nonlinear joint models in the Brake-Reuß beam.*

Joint	χ	$\phi_{\max}$	R	K_T
1, 5	-0.418	8.789×10^{-4}	7.947×10^{6}	5.7609×10^{5}
2, 4	-0.639	4.346×10^{-4}	5.199×10^{5}	1.0865×10^{5}
3	-0.271	6.612×10^{-4}	4.769×10^{7}	3.7345×10^{5}

3.4.4 Model Validation with Modally-Coupled Response Measurements

After deducing a set of parameters for the Iwan elements, the nonlinear model of the Brake-Reuß beam was validated by using it to simulate the response to an excitation that excites more than one mode. Recall from Section 3.4.1 and Fig. 3.6 that, when the response of a struc-

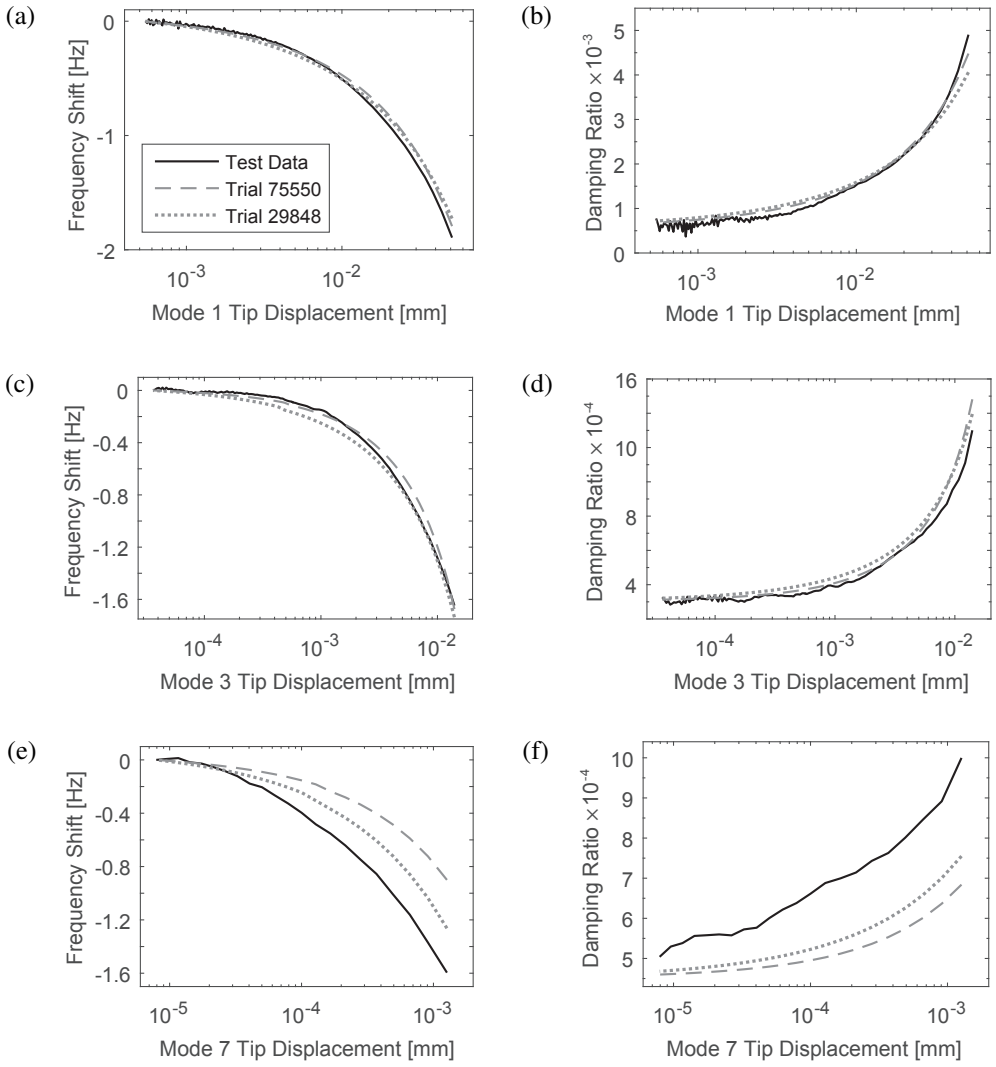

Figure 3.8: *Comparison between test and model of the (a,c,e) natural frequency shift and (b,d,f) damping ratio versus modal displacement amplitude in the (a,b) first, (c,d) second, and (e,f) third bending modes of the Brake-Reuß beam.*

ture is composed of multiple dominant modal signals, modal coupling causes the amplitude-dependent natural frequency and damping curves exhibited for each modal signal to deviate significantly from those where only the appropriate modal signal is dominant. Since the non-linear finite element model was tuned to those single-mode responses, then a good measure of its efficacy is its ability to predict a time response in which modal coupling occurs.

The same test 10 data, from which the frequency and damping curves shown in Fig. 3.6 were derived, were used as the target reference for this validation study. In this test, an impact force peaking at 251.3 N was applied at point s on the beam (refer to Fig. 3.3). The time history of this force, as measured from the PCB piezo-electric hammer, was recorded and supplied to a linear interpolation function to help form the input signal $f_{\text{peak}}(t)$ to be applied on the finite element model at the same location. For the Craig-Bampton-reduced Brake-Reuß beam system, the external force vector in Eq. (3.28) was then defined as

$$\mathbf{f}_{\text{ext}} = \mathbf{L}^{\text{T}} \boldsymbol{\Psi}_s^{\text{T}} f_{\text{peak}}(t). \tag{3.35}$$

The viscous damping matrix $\mathbf{C}$ was defined as in Eq. (3.19) using the fitted low-amplitude damping ratios given in Table 3.3 for the first four bending modes. All other modes were given $\zeta_{0,r}$=4.5$\times 10^{-4}$ based on the trend set by the third and fourth bending modes. The tuned y-direction springs (Table 3.1) and discretized Iwan elements [31] (with parameters given in Table 3.5) were then added for the five joint models. Equation (3.28) was then integrated numerically to simulate the response for a duration of 4 seconds after impact using the same Newmark method discussed in Section 3.3.2.

The simulated response at point s is shown in Fig. 3.9a for the first 0.5 seconds, along with the measured response at the same point. Here it can be seen that, remarkably, the simulated response closely follows the amplitude of the measured response. The signals appear to correlate well with each other during the first 0.03 seconds after impact, but afterwards the simulated acceleration maintains a 30%–40% overestimation of the measured acceleration until around

2 seconds. The peak amplitude difference between the simulated and measured acceleration is negligible at 2 seconds, but the simulated signal gradually begins underestimating the measured signal. At 4 seconds, the simulated signal underestimates the measured signal by only 10%.

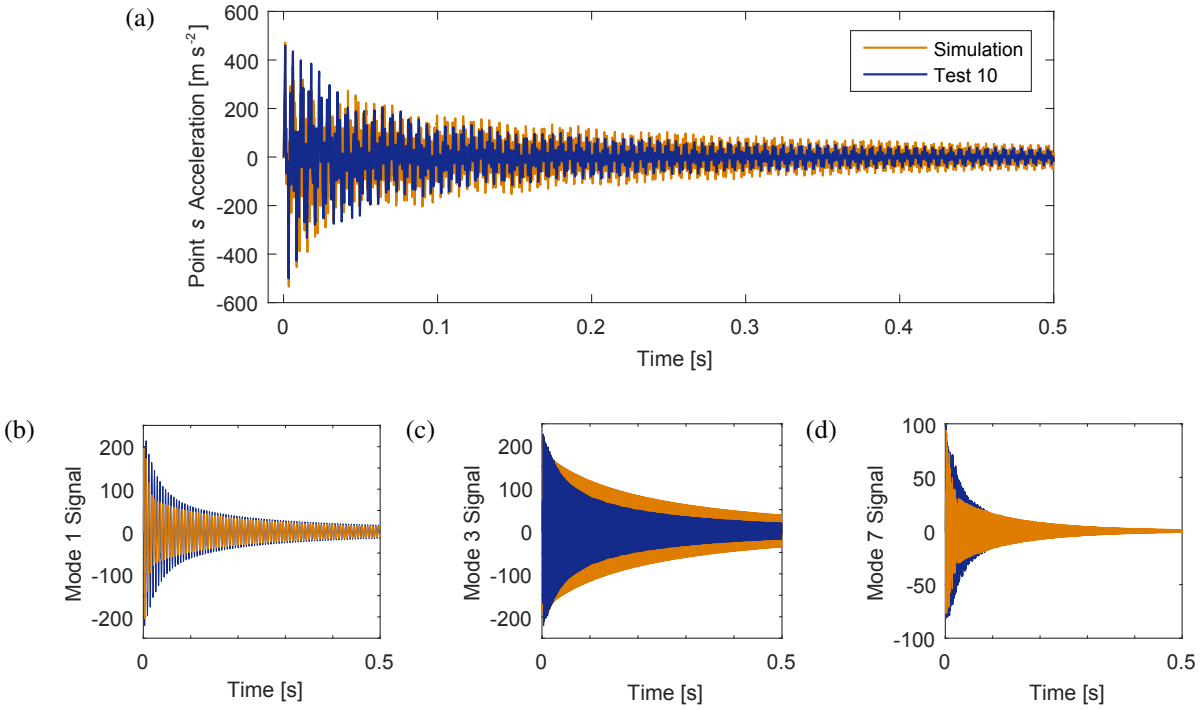

Figure 3.9: *Comparison between the measured acceleration and simulated acceleration at (a) point s of the Brake-Reuß beam, and its component signals for the (b) first bending, (c) second bending, and (d) third bending modes.*

In preparation for computing the instantaneous damping and frequency of each mode, the simulated and measured responses were both filtered into their component modal signals. For the simulated response, the component of the acceleration pertaining to mode r was computed as

$$a_{r,\mathrm{sim}}(t) = \boldsymbol{\Psi}_s \mathbf{L} \boldsymbol{\varphi}_r \boldsymbol{\varphi}_r^{\mathrm{T}} \mathbf{M} \ddot{\mathbf{u}}(t) \tag{3.36}$$

where $\boldsymbol{\varphi}_r$ is the mass-normalized mode shape computed via Eq. (3.4). In contrast, the measured

signal was filtered using an oblique projector,

$$a_{r,\text{test}}(t) = \mathbf{\Phi}_{s,r} \left(\mathbf{\Phi}^{\text{T}} \mathbf{\Phi} \right)^{-1} \mathbf{\Phi}^{\text{T}} \ddot{\mathbf{u}}_{\text{test}}(t). \tag{3.37}$$

Here, $\ddot{\mathbf{u}}_{\text{test}}(t)$ is the measured acceleration at the 12 accelerometer locations, and $\mathbf{\Phi}$ are the experimental mode shapes acquired for Section 3.4.1, with subscript "s, r" referring to the entry for mode r pertaining to the accelerometer on point s. The component signals corresponding to the first, second, and third bending modes are shown in Fig. 3.9b, 3.9c, and 3.9d, respectively.

The first and third bending signals appear to have an initial period where the simulated signal decays faster than the measured signal. After 0.1 seconds, however, the simulated first bending signal consistently underestimates the measured signal by 18%, whereas the third bending signal initially matches the peak amplitude but eventually overestimates by about 70% after 1 second. The third bending amplitude is much smaller than those of the first and second bending modes at 1 second, so this error is negligible in the physical response of point s. On the other hand, the second bending mode sees a slow decay in the response initially until there is a consistent 100% overestimation of the measured signal. The second bending signal is clearly the primary culprit behind the general overestimation of the physical response at point s, and the cause seems to be a lower-than-estimated damping in the first tenth of a second.

To confirm damping trends, the Hilbert transform method described in Section 3.3.2 was used on the three component signals for both the simulated and measured responses. The resulting instantaneous frequency and damping versus amplitude curves are shown in Fig. 3.10. As expected, towards the high amplitudes in the simulated curves (the beginning of the time history), both the first and third bending modes have large damping consistent with their rapid decay in response amplitude. Comparing with results from previous works, this sudden jump in damping at high amplitudes usually indicates that the Iwan elements have entered the macroslip regime [57]. This is not a desirable outcome because the test measurements do not seem to exhibit macroslip, so further tuning efforts would need to reevaluate the lower limit for $\phi_{\max}$ in

the Iwan elements. The second bending mode, on the other hand, does indeed underestimate the measured damping.

Towards the lower amplitudes, both the second and third bending modes converge towards the measured damping, though it can be argued that the damping could be modeled as approximately linear for these modes. For this impact case, most of the simulated nonlinear damping is done by the first bending mode, which correlates well with the measured damping in reproducing almost an order of magnitude in change with amplitude. That the first bending mode exhibits the most nonlinearity in damping indicates that it is the most dominant signal in the response. Although both the first and second bending modes appear to be co-dominant in acceleration, note that the constitutive formulation for the Iwan element (Eq. (3.24)) depends on displacement. A mode 1 acceleration signal that oscillates at A=100 m s^{-2} amplitude would have a displacement amplitude of around A/ω_1^2 =0.084 mm, but the same acceleration amplitude in mode 3 has displacement A/ω_3^2 =0.007 mm. This order of magnitude difference in displacement amplitude shows that the first bending mode is clearly dominant in this signal. This also shows that future efforts in determining modal dominance in structures with bolted joints should focus on the displacement state.

The simulated instantaneous frequency for each mode shows similar levels of agreement with the measurements as their counterparts in damping. The first bending mode shows remarkable agreement both in its low-amplitude value and in capturing the shift in frequency. The shift in frequency is also captured well for third bending, but there is an offset in the low-amplitude value due to the error in tuning the linear model. The second bending mode also has an error in offset, and its frequency shift does not quite match the measured shift.

Despite these errors, the overall agreement between simulation and measurement is impressive considering that the measured frequency and damping for an impact at point s differs significantly from those of impacts at other locations that give stronger signal strengths for each mode (the reader is referred to Fig. 3.6 for a comparison between test case 10, in which point

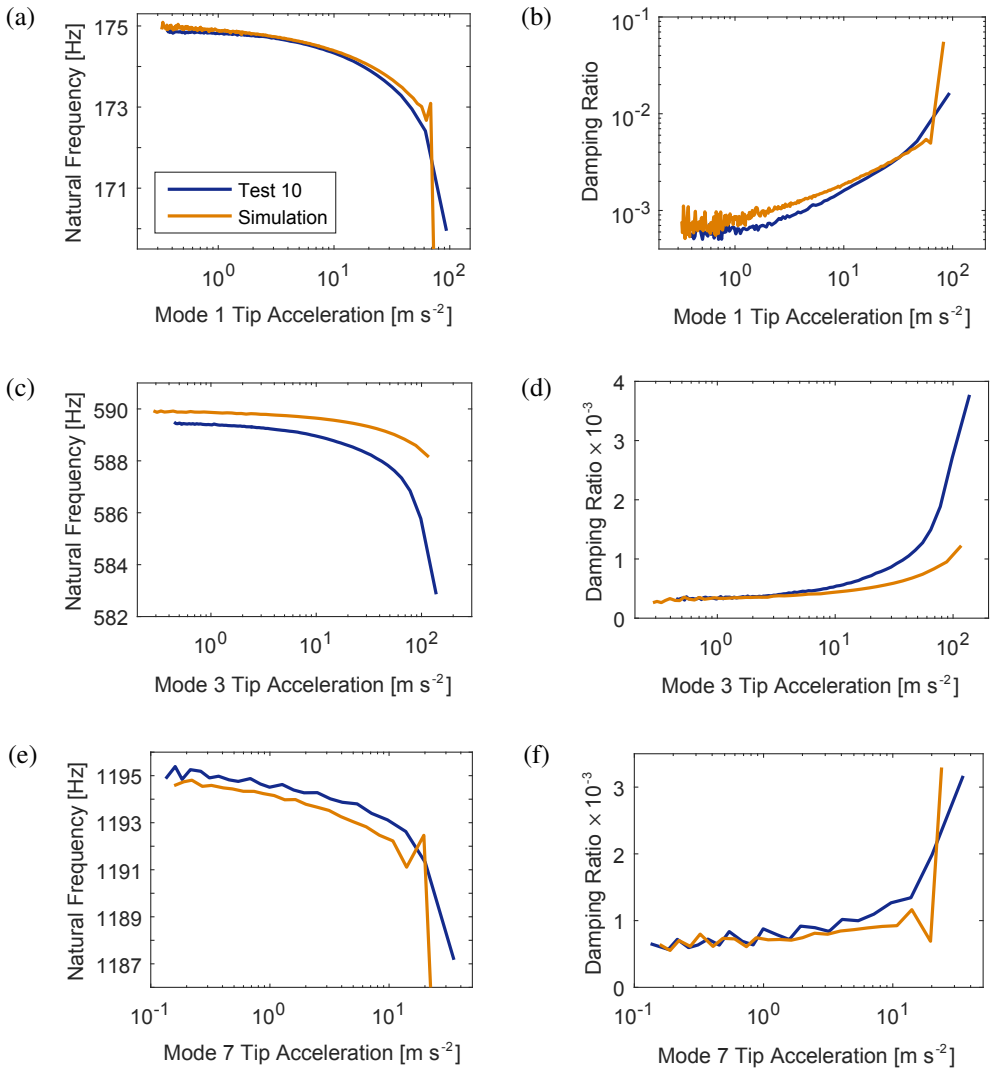

Figure 3.10: *Comparison between the measured and simulated (a,c,e) natural frequency and (b,d,f) damping ratio versus modal displacement amplitude in the (a,b) first, (c,d) second, and (e,f) third bending modes of the Brake-Reuß beam.*

s was impacted, versus the mode dominant cases that were used to tune the model). While further improvements to the model can certainly be made, the current tuned model can capture, with modest accuracy, the modal coupling in amplitude-dependent frequency and damping as seen in measurements. This fact alone gives the modeling techniques presented in this work an advantage over the uncoupled, nonlinear modal models studied in [32, 33, 57]. Even if the change in damping for some modes is small (or even unknown due to lack of measurements), models tuned using QSMA would still allow those modes to exhibit amplitude-dependent behavior that may be close to those of real structures, which is by far an improvement over the traditional linear models that are the standard in industry.

3.5 Conclusion

In this work, the method of quasi-static modal analysis (QSMA) was developed as an efficient tool for extracting the amplitude-dependent natural frequency and damping seen in the vibration modes of weakly nonlinear models of structures containing bolted joints. The premise of QSMA is that these properties can be computed from a modal force-deflection hysteresis, which is constructed by applying Masing's rules on the modal displacement response of the finite element model when subjected to a quasi-static ramp-up load distributed over the entire structure in the shape of a mode. The method is essentially a simplification of the groundwork laid by Festjens et al. [36] where in this work the entire structure is treated nonlinearly (as opposed to just the region around the joint) and the mode shapes are assumed to remain constant with amplitude. The unchanging modes assumption was checked by comparing the relative strength of the modal signals in the quasi-static response of a Brake-Reuß beam model containing Iwan elements. It was found that the mode of interest remains overwhelmingly dominant provided that the Iwan elements stay in the microslip regime. Because the modes could be considered unchanging, the mode-shape updating routine proposed by Festjens et al. could be bypassed for faster computation. In addition, further simplifications could be made

to the method of QSMA when applied to models containing Iwan elements, which obey Masing's rules in themselves. As a result of all of these simplifications, the method of QSMA was then shown to provide a *5-order* magnitude reduction in the time required to compute the amplitude-dependent frequency and damping for one mode in the Brake-Reuß beam model as compared to prior approaches that were based on dynamic simulation. Furthermore, the amplitude trends produced from QSMA are effectively the same as those obtained from the dynamic simulations, which attests to the accuracy of QSMA in the case that Iwan elements are used.

The computational efficiency of the method of QSMA was then capitalized by employing it as an engine for an iterative model updating routine. In essence, tens of thousands of permutations of Iwan element parameters were tested for the Brake-Reuß beam model in a brute-force approach that sought to fit the amplitude-dependent natural frequency and damping of the model with those acquired in experimental measurements. Here, a point was made that because QSMA loads a structure in the shape of a single mode, the natural frequency and damping it produces must likewise be fitted to data in which a single mode is dominant in the experimental response. Such data was acquired for the first, second, and (to a lesser extent) third bending modes of the Brake-Reuß beam, so a fitting was done simultaneously for these three modes. After deducing a viable parameter set for the Iwan elements, the model was validated by performing a dynamic simulation in which multiple modes were excited at a time (by applying at impact at the end of a beam), and comparing the amplitude-dependent frequency and damping trends with those of experiments. The simulated results were found to agree well with the measurements, though some evidence was found that the chosen parameter set is not ideal.

While the final results are not perfect, this work should serve more as a demonstration of a practical method for updating nonlinear models containing discrete joint elements. The structure considered here had only five joints and 84 degrees of freedom, but the method performed efficiently enough to be viable for much more complicated structures. It is hoped that the tech-

niques presented in this paper can pave the way for further improvements that ultimately lead to a new industry standard for fast and efficient updating of structural models with nonlinear joints.

Chapter 4

A Study on the Transient Behavior of the Five-Parameter Iwan-Type Model in Ring-Up and Ring-Down Simulations

Robert M. Lacayo, Matthew S. Allen

4.1 Introduction

The vast majority of aerospace structures are constructed of assembled components held together by lap joints, which are known to provide localized sources of stiffness and damping to the structure. In many cases, these joints are designed such that the surfaces of the two interfacing components hardly move relative to each other, so it is often sufficient to model the joint simply by welding the contacting surfaces or by tying the surfaces to beam elements that represent a bolted connection. However, when such structures are subjected to strong environmental loads, such as during lift-off for rockets or turbulence for aircraft, the friction at the bolted interface can cause the system to behave nonlinearly. A plethora of dynamic response test studies exist which show that, as a bolted structure is excited to higher forcing levels, a significant increase in structural damping and a slight decrease in the resonance frequencies can be measured due to the presence of a lap connection [1, 3, 16, 32, 33, 53, 54, 55].

Although the physics governing the interaction between the two surfaces could be described by a combination of tribological phenomena [10], the above cited works attribute the cause for the amplitude-dependence in damping and frequency predominately to microslip friction [12]. As a bolted joint is loaded in shear, small regions in the interace – typically in areas of low-

pressure away from a bolt hole – break their contact and experience slip. A joint is said to be in microslip when these localized regions of slip occur, yet the joint as a whole remains intact due to the regions near the bolt that remain stuck. As the shear loading continues to increase, the regions of slip grow large, which both reduces the stiffness of the joint and increases the rate of energy dissipation due to friction. When the slip region covers the entire interface, the joint is said to be in macroslip, where the two surfaces experience bulk shear motion relative to one another. Joints are typically designed to stay within the microslip regime, so the modeling of macroslip, which is the focus of [13, 14, 15] for example, is not a concern in this work.

A well-known model for microslip is the parallel-series distributed-element model developed by Iwan [28]. As illustrated in Fig. 4.1, this distributed-element model, also referred to as the Iwan model, consists of a parallel arrangement of a large (ideally infinite) number of Jenkins elements (a spring and Coulomb slider in series), where each Jenkins element is defined with the same spring stiffness and a different slip force threshold. As the Iwan model displaces from equilibrium, each of the sliders begins to slip one after another, similar to how microslip develops in a joint as the loading increases. Iwan formulated the model so that the slip thresholds of each of the Jenkins elements can be defined by a statistical distribution function. Segalman later defined a four-parameter distribution function such that the energy dissipated per cycle by an Iwan model undergoing harmonic motion follows a power-law trend with the loading amplitude [31], as measured from experiments. This four-parameter Iwan model has since been used in several subsequent works in order to model jointed structures that exhibit similar power-law damping behavior in microslip [30, 66, 32, 33, 57, 35, 37, 65].

The drawback of the four-parameter Iwan model is that its formulation strongly couples the stiffness with the dissipation, and this sometimes makes it challenging to fit the model to experimental measurements. In previous works, the Iwan model has been used successfully to reproduce the nonlinear behavior of a single mode of a structure [32, 33, 57]. These are termed “modal Iwan models” because the Iwan element captures the net effect that all joints

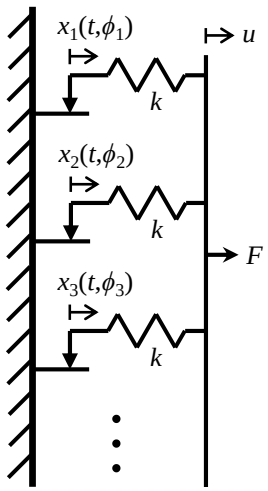

Figure 4.1: *Schematic of an Iwan model. The current state x_i of each slider adjusts when $|u - x_i| > \phi_i$, the static slip threshold.*

have on the mode in question. Four-parameter Iwan elements have worked well when used in the modal domain, but difficulties have arisen when they are used to model a set of physical joints (including their equivalent stiffness, damping, and their location in a structure). For example, a study by [65] demonstrated through an exhaustive analysis of different parameter permutations that, although a set of four-parameter Iwan elements could be fitted to either the measured amplitude-shift in the natural frequency (stiffness) or the damping (energy dissipation) with good accuracy, the fitting of both properties was impossible (see Fig. 4.2). Mignolet [35] investigated this problem, and he proposed allowing each slider to have different static and dynamic friction coefficients. This allows each slider to exhibit stiction: a large static friction force that decreases when the slider begins to slip. Mignolet assigned a fifth parameter to govern this decrease in the friction force, and he used his new five-parameter Iwan-type formulation to derive closed-form expressions for amplitude-dependent stiffness and dissipation during steady-state harmonic motion. With these expressions, he was able to fit his model to the stiffness and dissipation measurements successfully. However, Mignolet never investigated how the five-parameter Iwan-type model could be implemented for transient vibration, so the implications of the fifth parameter on the transient response of an Iwan model has yet to be

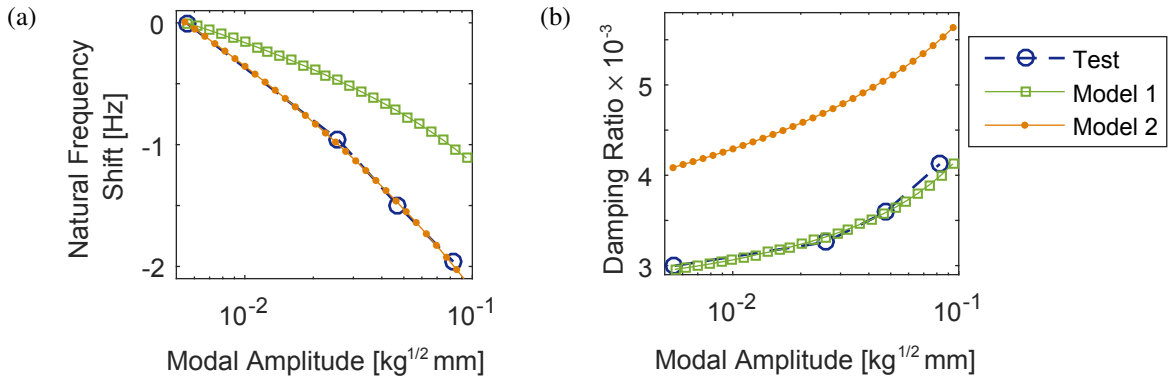

Figure 4.2: *Plots of the measured and simulated (a) natural frequency shift and (b) equivalent damping ratio versus the amplitude of modal displacement for the first bending mode of the beam structure studied in [65]. A comparison is made between a model whose Iwan parameters were tuned to fit the damping (model 1) and a model tuned to fit the natural frequency shift (model 2).*

studied.

This work presents an implementation of the five-parameter Iwan-type model in the form of a computational element that can be used in finite element analysis, and documents an investigation on the amplitude-dependent stiffness and dissipation of that element in more general transient settings, particularly in free-response decay. In Section 4.2, Mignolet's steady-state formulation of five-parameter Iwan-type model is reviewed, and an algorithm for the computational element is presented. In Section 4.3, the hysteresis of the Iwan element was investigated under steady-state, ring-up, and ring-down loading cases, and it was found that stiction causes the Iwan-type model to have a stronger dependence on its displacement history than the original Iwan model. This strong path-dependence is such that Mignolet's expressions for amplitude-dependent stiffness and dissipation no longer hold well when steady-state vibration is reached after a ring-down response. Even so, the ring-down hysteresis was found to exhibit a certain regularity in its shape, which was exploited to develop new expressions for stiffness and dissipation that apply for ring-down (Section 4.4). In Section 4.5, these new expressions were used to predict the amplitude-dependent behavior in the free-response decay of a single-mass oscillator connected to ground with a five-parameter Iwan element. Although superb accuracy

was achieved in the prediction, the Iwan-type model was also found to have certain drawbacks that limit its practicality as a joint model.

4.2 Overview of the Five-Parameter Iwan-Type Model

To understand the transient behavior of a five-parameter Iwan-type model, one must first understand its constitutive formulation and how it relates to the four-parameter model formulation. The following subsections give a brief treatment on the constitutive formulation – offering an interpretation on how Mignolet's fifth parameter helps to weaken the coupling between stiffness and dissipation – followed by an algorithm that implements the model in a computational setting.

4.2.1 The Constitutive Equation

Consider the parallel-series Iwan model illustrated in Fig. 4.1, which is composed of a parallel implementation of Jenkins elements: linear springs in series with a Coulomb slider. The deflection of each spring is a difference between the current displacement u of the Iwan model and the position x of the local Coulomb slider. When the spring deflection reaches a certain threshold ϕ, the slider begins to slip. Since there is no mass connecting the spring to the slider, the slider displaces instantaneously with u when slip occurs (i.e. $\dot{x} = \dot{u}$ until load reversal). When the number of Jenkins elements is taken to infinity, the slip thresholds may be described by a distribution function, $\rho(\phi)$. Using Segalman's constitutive formulation, the evolution of the force exerted by an Iwan element over time is described by a summation of the spring forces over the entire distribution, as in [31]

$$F(t) = \int_0^\infty \Gamma(t, \phi)\rho(\phi)d\phi, \tag{4.1}$$

where

$$\Gamma(t,\phi) = \begin{cases} u(t) - x(t) & \text{for } |u(t) - x(t)| < \phi \text{ (stick)}, \\ \phi & \text{otherwise (slip)}, \end{cases} \tag{4.2}$$

tracks the current deflection of each spring. In Eq. (4.1), Segalman incorporates the spring stiffnesses within the distribution function ρ, which he defines as the four-parameter function[31]

$$\rho(\phi) = R\phi^{\chi}\left[H(\phi) - H(\phi - \phi_{\text{max}})\right] + S\delta(\phi - \phi_{\text{max}}), \tag{4.3}$$

where H is the Heaviside step function, and δ is the Dirac delta function. Here, the $R\phi^{\chi}$ term, with $-1 < \chi < 0$, describes a decaying power law relationship that is truncated after $\phi = \phi_{\text{max}}$ (the threshold for macroslip), and terminated with a Dirac delta having strength S. As explained in Section 4.2.2, this distribution function allows the Iwan element to dissipate energy per vibration cycle at a rate that follows a power-law trend with the deflection amplitude.

Equations (4.1) to (4.3) form the basis for Segalman's four-parameter Iwan model. However, after realizing that this formulation can fail to fit experimental measurements of stiffness and dissipation as functions of amplitude, Mignolet proposed the addition of a fifth parameter that accounts for a difference between the static and dynamic friction coefficients for each Coulomb slider [35]. In his new formulation, Mignolet assumed that, when the slider initiates slip, the force immediately drops to a defined fraction, θ (for $0 < \theta \leq 1$), of the maximum static friction force. This creates a discontinuous jump in the slip condition, which redefines Eq. (4.2) into [35]

$$\Gamma_{\theta}(t,\phi) = \begin{cases} u(t) - x(t) & \text{for } |u(t) - x(t)| < \phi \text{ and } t < t_s \text{ (stick)}, \\ \theta\phi & \text{for } |u(t) - x(t)| = \theta\phi \text{ and } t_s \leq t < t_r \text{ (slip)}, \end{cases} \tag{4.4}$$

where t_s refers to the time at which of slip occurs, and t_r is the occurrence of load reversal. After load reversal, the quantity $|u(t) - x(t)| < \theta\phi < \phi$, so the slider state returns to the stick

condition.

Comparing Eq. (4.4) with Eq. (4.2), it can be seen that the stick condition is unchanged, but the implication of Mignolet's new slip condition is that, for those Jenkins elements that initiate slip, the spring deflections drop immediately from ϕ to $\theta\phi$. In other words, the slider state x experiences an immediate and discontinuous displacement shift so that the dynamic slip condition is satisfied. This represents a fundamental change in the physics represented by Iwan's original distributed-element model. Not only must the computational implementation of the Iwan model be revised to account for this phenomenon, but also many of the assumptions that previous works make with regards to the amplitude-dependent behavior of an Iwan model may not hold for the Iwan-type model. These challenges are addressed in the subsequent sections.

As a final note, Eq. (4.4) reduces to Eq. (4.2) in the case that $\theta = 1$, so the four-parameter Iwan model is considered a special case of the five-parameter Iwan-type model, and it serves as a good reference for comparison in this work.

4.2.2 Secant Stiffness and Energy Dissipation under Harmonic Motion

If the displacement of the five-parameter Iwan-type model is defined with a sinusoidal function, as in $u(t) = u_0 \sin(\Omega t)$, then Mignolet shows that the force exerted by the model in microslip ($u_0 < \phi_{\text{max}}$) reaches a peak value (amplitude) of [35]

$$F_0(u_0) = K_T u_0 - \Lambda u_0^{\chi+2}. \tag{4.5}$$

where

$$K_T = \frac{R\phi_{\text{max}}^{\chi+1}}{(\chi+1)} + S, \quad \Lambda = \frac{R\left[\chi + 2 - \theta(\chi+1)\right]}{(\chi+1)(\chi+2)}. \tag{4.6}$$

From the peak force, the equivalent (secant) stiffness is computed as

$$K(u_0) = \frac{F_0}{u_0} = K_T - \Lambda u_0^{\chi+1}. \tag{4.7}$$

In [31, 35], the quantity K_T is referred as the tangent stiffness that occurs at zero-load equilibrium. The second term Λ serves to decrease K from this tangent stiffness as the vibration amplitude increases.

Lastly, Mignolet's derivation for the energy dissipated per oscillation cycle (also for $u_0 < \phi_{\text{max}}$) yields [35]

$$D(u_0) = \frac{R\left[2\theta(\chi+4) + (1-3\theta^2)(\chi+2)\right]}{(\chi+3)(\chi+2)} u_0^{\chi+3}. \tag{4.8}$$

Note that, under a given a parameter set $[\chi, \phi_{\text{max}}, R, S, \theta]$, both K and D depend only on a power of u_0, the amplitude of oscillation. Mignolet remarks that setting $\theta = 1$ reduces the equations to Segalman's derivations [31] for the same properties:

$$K|_{\theta=1} = K_T - \Lambda|_{\theta=1}\, u_0^{\chi+1} = K_T - \frac{R u_0^{\chi+1}}{(\chi+1)(\chi+2)}, \tag{4.9}$$

$$D|_{\theta=1} = \frac{4R u_0^{\chi+3}}{(\chi+3)(\chi+2)}. \tag{4.10}$$

In comparing Eq. (4.9) and (4.10) with Eq. (4.7) and (4.8), it can be seen that the introduction of the θ parameter provides a means of decoupling the amplitude trends in stiffness and dissipation. Looking specifically at the coefficient multiplying the power of u_0 in $K|_{\theta=1}$ and $D|_{\theta=1}$, both of these coefficients are proportional to R and inversely proportional to a quadratic function of χ. Hence, any change in R or χ that increases the rate that $D|_{\theta=1}$ grows with $u_0^{\chi+3}$ would proportionally increase the rate that $K|_{\theta=1}$ decreases with $u_0^{\chi+1}$. By adding θ as a parameter, the Λ term in K becomes linearly proportional to θ, but the coefficient in D becomes quadratically proportional to θ. Thus θ provides an extra degree of freedom for independently controlling the rates of decay and growth in K and D, respectively.

A comparison of the amplitude-dependence of K and D with their four-parameter counterparts can be made by taking the ratios of Λ to $\Lambda|_{\theta=1}$ and D to $D|_{\theta=1}$. These ratios are

$$\frac{\Lambda}{\Lambda|_{\theta=1}} = \chi + 2 - \theta(\chi + 1), \tag{4.11}$$

$$\frac{D}{D|_{\theta=1}} = \tfrac{1}{2}\theta\left(\chi + 4\right) + \tfrac{1}{4}\left(1 - 3\theta^2\right)\left(\chi + 2\right), \tag{4.12}$$

which are functions of θ and χ only. Line plots for both of these ratios are illustrated in Fig. 4.3.

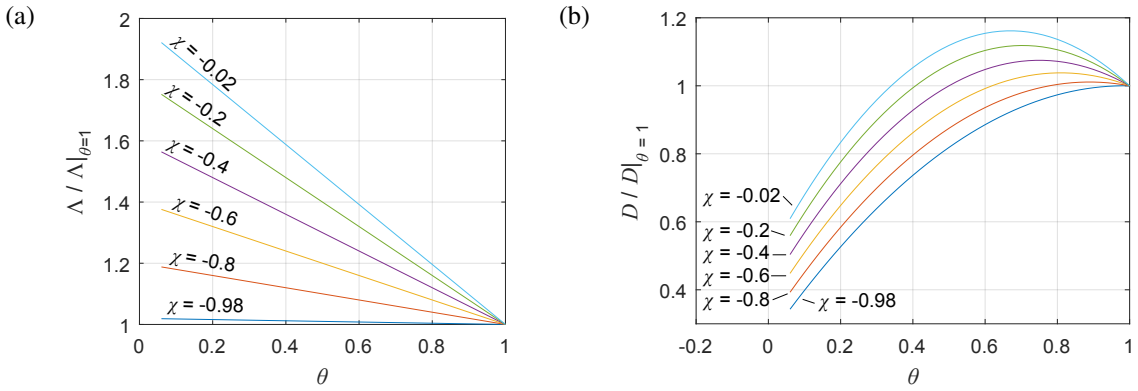

Figure 4.3: *Line plots of the ratio between the five-parameter versus the four-parameter Iwan model of (a) the stiffness decay coefficient and (b) the energy dissipated per cycle.*

Figure 4.3a reveals that any decrease in θ from 1 would always result in an increase in Λ, which, in turn, increases the rate that K decreases from K_T as the amplitude increases. On the other hand, Fig. 4.3b shows that, depending on the values chosen for θ and χ, the energy dissipated per cycle by a five-parameter model could increase or decrease relative to that of the four-parameter model. For example, if a factor of 1.4 increase in the rate of decay in stiffness is desired (the $\Lambda/\Lambda|_{\theta=1} = 1.4$ line), the smallest value of χ that can achieve this is $\chi = -0.6$ when $\theta \approx 0$. The five-parameter model would achieve a 0.4 factor decrease in the dissipation rate from the four-parameter model with these same parameters. On the contrary, the same 40% increase in stiffness decay can be achieved with $\chi = -0.02$ and $\theta = 0.6$, but the

dissipation rate instead increases to a factor of 1.17. Unfortunately, these scalar factors are the limits that exist for the extreme values of χ and θ. There still exists some amount of coupling that prevents the dissipation of the five-parameter model from exceeding a 1.17 factor increase over the four-parameter model, and likewise the lower limit is not much smaller than a 0.4 factor decrease.

Nonetheless, within the range of the extreme values of χ and θ, the fifth parameter allows additional flexibility to fit the five-parameter Iwan-type model to experimental measurements of both the stiffness and the damping exhibited by a joint. This advantage is highly desired for modeling and simulating the transient free-response of a bolted structure, but Mignolet only derived Eq. (4.7) and (4.8) for steady-state, sinusoidal motion. To attribute these expressions to a ring-down response, the behavior of the Iwan-type model must be studied under various loading and unloading scenarios to confirm that it exhibits the same amplitude-dependence in transient response as it does in the steady-state.

4.2.3 Discretization for Computational Modeling

To investigate the transient behavior of a five-parameter Iwan-type model, a computational element embodying its force-constitutive relationship is required. The path-dependent nature of the Iwan model necessitates that some form of memory of Jenkins slider states must be passed from one load step to another. This is difficult to implement for a continuous distribution containing an infinite number of sliders, which thus far lacks a closed-form solution. Hence, the alternative is implemented, where the constitutive model is approximated by using a finite discretization of sliders. The discretization followed here is based on that given in [31], which assigns a stiffness and slip threshold to each Jenkins element in a finite set using the the distribution function given by Eq. (4.3).

Equation (4.3), illustrated in Fig. A.2, is divided into $N-1$ number of intervals in ϕ such that the left boundary of each interval i is $\tilde{\phi}_i$, and the right boundary of the $(N-1)$th interval

terminates at $\phi_{\max}$. The boundaries may be spaced uniformly from 0 to $\phi_{\max}$, or they may be spaced geometrically as in [31], where the length of the ith interval is some factor $\alpha > 1$ larger than the length of the previous interval,

$$\Delta_i = \alpha \Delta_{i-1}, \qquad \Delta_1 = \frac{\alpha - 1}{\alpha^{N-1} - 1} \phi_{\max}. \tag{4.13}$$

Each interval i corresponds to the ith Jenkins element, which has a slip threshold ϕ_i defined as the midpoint of that interval. The spring stiffness k_i for each element can be derived by evaluating Eq. (4.1) within the bounds of the interval. The stiffness turns out simply as the bounded area under the distribution curve,

$$k_i = \frac{R}{\chi + 1} \left(\tilde{\phi}_{i+1}^{\chi+1} - \tilde{\phi}_i^{\chi+1} \right), \qquad i = 1 \,..\, N-1. \tag{4.14}$$

To account for the Dirac delta term, a Nth Jenkins element is added with slip threshold $\phi_N = \phi_{\max}$ and stiffness $k_N = S$.

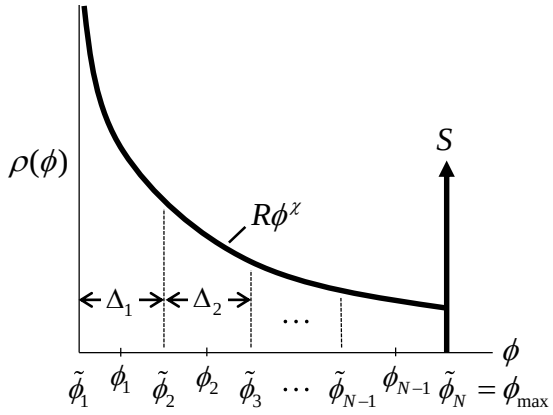

Figure 4.4: *Illustration of Segalman's four-parameter distribution function and its discretization.*

With each Jenkins element now appropriately defined by the distribution function, their states can be tracked over time as the discrete Iwan element flexes. In Segalman's orignal algorithm [31], it was sufficient simply to update and pass only the slider states x_i from one

load step to the next since, in each load step, the quantity $|u - x_i|$ could be checked against ϕ_i to determine whether a slider had reached the slip state (per Eq. (4.2)). In Mignolet's model, however, there are two slip thresholds to check: ϕ_i for while the slider is stuck, and $\theta\phi_i$ during slip. Once a Jenkins element begins to slip, the deflection of its spring immediately drops from ϕ_i to $\theta\phi_i$. If $|u - x_i| < \phi_i$ is always used to check for slip, then the Jenkins element would always appear to be in the stuck state. To correct this, a second "state" variable, n, is added to record the number of sliders that have reached the slip state so that the algorithm knows to switch the slip threshold.

Thus, the new algorithm for computing the force exerted by a five-parameter Iwan-type element during a load step j requires three state inputs: the current displacement $u(j)$ of the element, the state $x_i(j-1)$ of each Jenkins slider from the previous load step, and the number n_{j-1} of those sliders that have reached the slip state in the previous load step. First, the current static and dynamic slip thresholds $\hat{\phi}_i$ are determined based on those sliders that reached the slip state in the previous load step,

$$\hat{\phi}_i = \begin{cases} \theta\phi_i & \text{for } i = 1 \,..\, n_{j-1} \text{ (slip)}, \\ \phi_i & \text{for } i = (n_{j-1}+1) \,..\, N \text{ (stick)}. \end{cases} \tag{4.15}$$

The current spring deflections are then checked against the slip condition,

$$|u(j) - x_i(j-1)| \geq \hat{\phi}_i, \tag{4.16}$$

and the number of sliders that satisfy this condition is n_j for the current load step. The states for those sliders that have slipped are then updated as

$$x_i(j) = \begin{cases} u(j) - \theta\phi_i \text{ sign}[u(j) - x_i(j-1)] & \text{for } i = 1 \,..\, n_j \text{ (slip)}, \\ x_i(j-1) & \text{for } i = (n_j+1) \,..\, N \text{ (stick)}. \end{cases} \tag{4.17}$$

The force exerted by the discrete Iwan-type element,

$$F_J(j) = F_{\text{slip}} + F_{\text{stick}}, \tag{4.18}$$

is then computed as a summation of forces from those Jenkins elements that are currently slipping,

$$F_{\text{slip}} = \sum_{i=1}^{n_j} \theta k_i \phi_i \ \text{sign}[u(j) - x_i(j)], \tag{4.19}$$

and those that are still stuck,

$$F_{\text{stick}} = \sum_{i=n_j+1}^{N} k_i [u(j) - x_i(j)]. \tag{4.20}$$

The tangent stiffness of the discrete Iwan-type element for the current load step is simply a summation of the stiffnesses for those elements that are still stuck,

$$k_{\text{tan}}(j) = \sum_{i=n_j+1}^{N} k_i. \tag{4.21}$$

Following these computations, both $x_i(j)$ and n_j are then passed into the next load step.

4.2.4 The Effect of the Interval Bias Parameter

A preliminary study was conducted on the discrete Iwan-type element to examine appropriate values of α to use. As discussed previously, the parameter α defines the scalar factor increase in the size of successive intervals of ϕ in the discretization of the ρ distribution. It essentially defines a bias in the slip thresholds ϕ_i towards the lower values in order to allow more sliders to slip at lower vibration amplitudes. Since α is purely an artifact of this discretization and not one of the five parameters meant to characterize the force exerted by the Iwan-type element, any effects it has on Eq. (4.18) must be mitigated. For the four-parameter Iwan element, Segalman

remarks that specifying $\alpha = 1.2$ and $N > 50$ allows the element to exhibit "satisfactory" dissipation behavior for displacement amplitudes at least one order of magnitude lower than $\phi_{\max}$, the point of macroslip [31]. The question then arises as to whether these values still hold for the five-parameter element.

For this study, an Iwan-type element with parameters χ=-0.6, $\phi_{\max}$=6×10^{-4}, R=7×10^{5}, S=9×10^{3}, and θ=0.3 was discretized into a set of N=100 Jenkins elements, whose states were initialized to zero. Three bias values, α=1.2, 1.05, and 1 (uniform intervals), were tested for this Iwan element. For each case, the element was subjected to a quasi-static displacement that increases monotonically from $u = 0$ to 5×10^{-4} in 2500 load steps. Equation (4.18) was evaluated at each load step while ensuring that the slider states x_i and the slip count n state were passed successively after each load step. The resulting force-deflection curves for each case are shown in Fig. 4.5a. Here, it can be seen that the force deflection curves have a jagged appearance that seems to increase in magnitude for higher values of α and u.

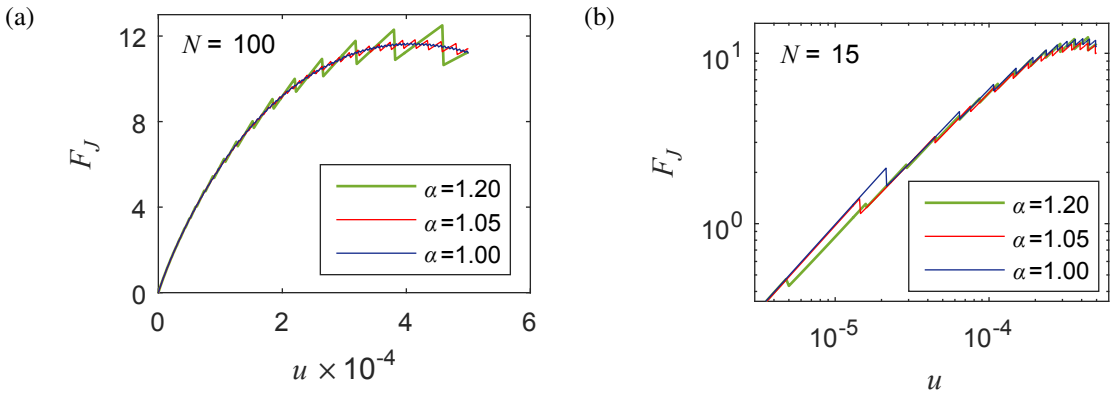

Figure 4.5: *Comparison of the force-deflection plots produced from a five-parameter Iwan-type element that has been discretized using different values of α. Plot (a) uses $N = 100$ Jenkins elements and highlights the discontinuities in F_J near $\phi_{\max}$, and plot (b) uses 15 Jenkins elements to highlight the bias effect of α.*

The jaggedness occurs due to the discontinuous jump from the static to the kinetic friction force as each successive Jenkins element begins to slip, which confirms that the algorithm is implementing stiction correctly. However, as can be seen in the case of $\alpha = 1.2$, a large

interval size between slip thresholds correlates to a similarly large drop in the force once a slider reaches its slip threshold, so an Iwan element with a truly continuous distribution of infinite sliders (infinitesimal interval widths) would not show these discontinuous jumps. The case of α =1 has relatively small interval sizes at higher values of u (due to the unbiased, uniform spacing), so its force-deflection curve is more continuous and closer to the true curve than those of the other cases. One would think to use a uniform sizing of intervals for all applications of the Iwan-type element, but there is a trade-off to arbitrate in doing so.

In application, it is possible that the five-parameter Iwan-type element may be subjected to vibration levels that are a few orders of magnitude smaller than $\phi_{\max}$. If the point of slip, ϕ_1, for the first slider is greater than this vibration amplitude, then none of the sliders in the discrete Iwan-type element would undergo slip, which is far from the case if the Iwan element could be represented with a continuous distribution (infinite number) of sliders. To allow the Iwan element to behave nonlinearly at low amplitudes, the intervals must be arranged such that a sufficient "resolution" of sliders slip at lower values of ϕ. One way to achieve this is to increase the number of intervals N, but this increases the number of slider states to record and, thus, increases computational costs. The alternative is to increase α, which causes a bias in the slip thresholds towards lower amplitudes, as demonstrated in Fig. 4.5b. When the Iwan element defined above contains 15 sliders, the first slider slips at $u = 5\times10^{-6}$ for the case that $\alpha = 1.2$, but this first threshold is 15×10^{-6} for $\alpha = 1.05$ and 21×10^{-6} for uniform intervals.

With higher values of α, one can achieve better resolution of nonlinearity at low amplitudes, but a larger number of sliders would be needed to mitigate the force discontinuities at higher amplitudes. The challenge, then, is to mediate this trade-off when applying the Iwan-type element in a transient simulation.

4.3 The Transient Behavior of the Five-Parameter Iwan-Type Element

The basic behavior of five-parameter Iwan-type element can be understood by examining three displacement waveform cases: steady-state, ring-up, and ring-down. An examination of Eqs. (4.18) to (4.20) reveals that the discrete Iwan model has no explicit time dependence or rate (velocity) dependence, and it only depends on displacement and the history of its slider positions. Hence, the Iwan element does not distinguish a transient response from a quasi-static response; the force it exerts will be the same if it follows the same displacement path in any loading case (with the same initialization of slider states) regardless of how quickly that path was traversed. Thus, to save on computational costs, the three aforementioned waveform cases were studied by statically displacing the Iwan-type element.

4.3.1 Steady-State Behavior After a Monotonically-Increasing Displacement

The steady-state case was examined first in order to gain insight on the phenomenon that enables the Iwan-type element to exhibit stiffness and dissipation behavior that is consistent with Mignolet's amplitude expressions, Eq. (4.7) and (4.8). An Iwan element with the same parameters as specified in Section 4.2.4 was used, but the element was discretized into a set of $N = 10000$ sliders having uniform intervals in ϕ to ensure a smooth F_J output that is close to that of a continuous Iwan-type element. The discrete element was subjected to a sinusoid displacement of the form

$$u(t) = u_0 \sin(2\pi t) \tag{4.22}$$

for one and one-quarter cycles ($t \in [0, 1.25]$) sampled at step size 0.001. The element was displaced to an amplitude $u_0 = 5{\times}10^{-4}$. The slider states were first initialized to zero, and then Eq. (4.18) was evaluated at each time step in succession. The resulting force-displacement curve is plotted in Fig. 4.6. The first quarter cycle creates an initial loading curve up to u_0, and

the remaining full cycle forms the reverse and forward curves of a hysteresis bounded by $\pm u_0$.

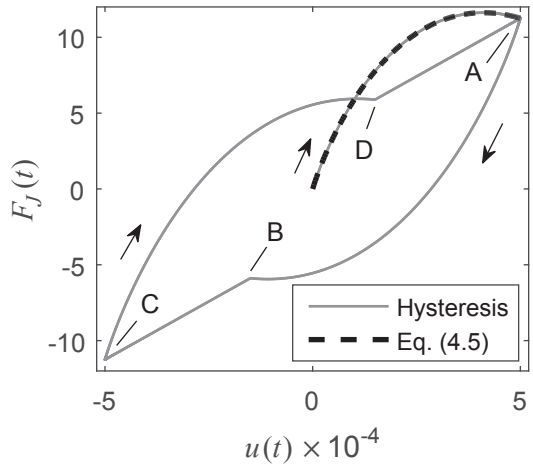

Figure 4.6: *Force-displacement curve for the case of sinusoid displacement on the discrete Iwan-type element.*

Some interesting phenomena are present in Fig. 4.6. Most striking is that the shape of the hysteresis resembles that of a hurricane weather symbol, where the development of the forward (or reverse) curve between points C and D (or A and B) can be described by a gradual decrease in the slope until a switch to a constant-slope regime after point D (or B). Despite the peculiar shape, if one were to compute the slope of the secant line connecting points A and C, its value would be equal to that computed with Eq. (4.7) (equivalent stiffness) for the given u_0. Likewise, the area enclosed by this hysteresis is equal to the value that would be obtained from Eq. (4.8) (dissipation per cycle). Even after u_0 was adjusted to form a smaller or larger hysteresis, these stiffness and dissipation equivalences were upheld (see Appendix G). This shows that if the Iwan-type element is loaded monotonically up to a certain displacement and then undergoes steady-state vibration at that amplitude, then the hysteresis it exhibits is consistent with Mignolet's expressions for amplitude-dependent stiffness and dissipation. A hysteresis that exhibits this property is referred to as a "Mignolet hysteresis" in the rest of this work.

Also important to note from Fig. 4.6 is that the initial loading curve preceding the hysteresis

exactly traces the max-force (backbone) curve produced with Eq. (4.5). This makes sense because any point on the initial loading curve can be a starting point of load reversal, from which begins a hysteresis whose maximum force is defined by that point of load reversal. Hence, it follows that point A (and point C in a negative sense) from a Mignolet hysteresis always lies on this maximum force curve, as exemplified by the three hysteresis cases depicted in Fig. G.1 in Appendix G.

The force and tangent stiffness time histories associated with this hysteresis are depicted in Fig. 4.7. As mentioned before, the period between $t = 0.25$ to 1.25 forms a Mignolet hysteresis, so a continuation of the steady-state would just be a repeat of this cycle. The force history shown in Fig. 4.7a gives an appearance as if multiple different waveforms were cut and then stitched on end over time. Part of this is, of course, due to the jump discontinuity in the tangent stiffness occuring at $t = 0.25$ and 0.75 (points A and C). However, the jump discontinuity in the slope of the force curve seen at around $t = 0.55$ and 1.05 (points B and D) is not consistent with the continuous evolution of the tangent stiffness curve at these points in time. Inspection of Eq. (4.21) and (4.14) reveals that the tangent stiffness is only influenced by the first four parameters of Segalman's formulation, so the slope discontinuity in the force must be a consequence of the θ parameter.

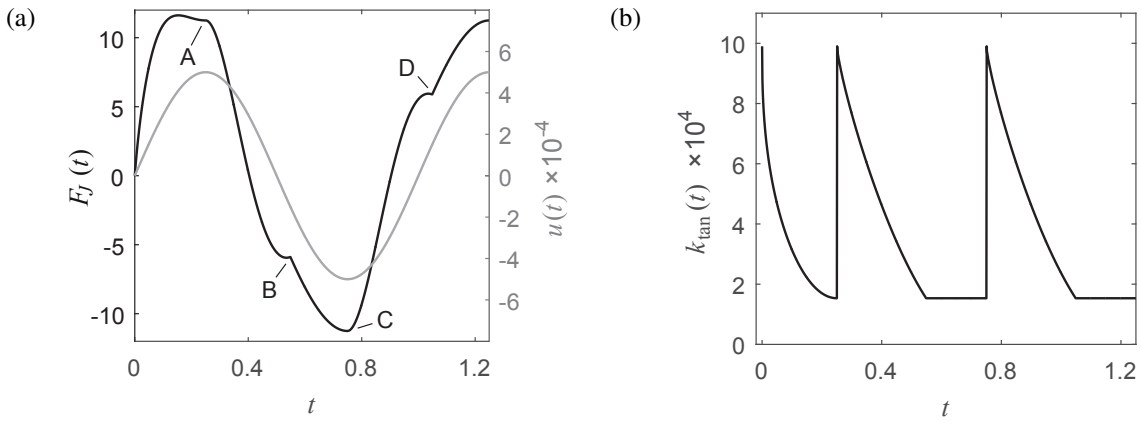

Figure 4.7: *(a) The force history and (c) the tangent stiffness history associated with the force-deflection curve shown in Fig. 4.6.*

In the moments just before points B and D are reached, the force appears to reverse load briefly, as if the force had reached its maximum and was thereafter decreasing towards the other maximum (even though this is far from the case in reality). The apparent lessening in the force is actually due to the drop in force from static friction to kinetic friction in the Jenkins elements, as discussed in Section 4.2.4. Although the force drop occurs continuously (since a growing $u(t)$ initiates slip in the Jenkins elements one after another), the size of the drops (due to the small value of ϕ_i for those elements that slip first) does not overcome the rate that the force increases (due to tangent stiffness of those Jenkins elements that are still stuck) until the u is comparable to $\phi_{\max}$. When u approaches $\phi_{\max}$, the rate at which the force drops overcomes the increase in force from the tangent stiffness of the remaining sliders, so the force decreases with increasing displacement. This behavior is entirely dependent on the value of θ. A θ value closer to 1 may not result in a premature reversing of the load before the displacement reaches its maximum.

The states of the Jenkins elements during this initial loading and hysteresis cycle can be observed to better understand the processes at play. Figure 4.8 shows a series of snapshots on the evolution of the slider states over time. An Iwan element with four sliders was used here to simplify the visualization, but the phenomena shown in Fig. 4.8 apply similarly to Iwan elements with more sliders. The sliders shown are arranged from top to bottom in order of increasing slip threshold (the top sliders slip first).

At time $t = 0$ (Fig. 4.8a), all slider states and u are initialized at zero. All sliders are in a stuck position, so the stiffness of all springs contribute to the tangent stiffness of the Iwan-type element. Moving forward in time, the Iwan-type element displaces to the right, invoking a restoring force from all Jenkins springs. By $t = 0.102$ (Fig. 4.8b), the first slider has already slipped, whereas the second slider is on the cusp of slipping. In the next time instance (Fig. 4.8c), the second slider has slipped, so its position jumps from $u(t) - \phi_2$ to $u(t) - \theta\phi_2$. This in turn decreases the restoring force from the spring down to the kinetic friction force, and the

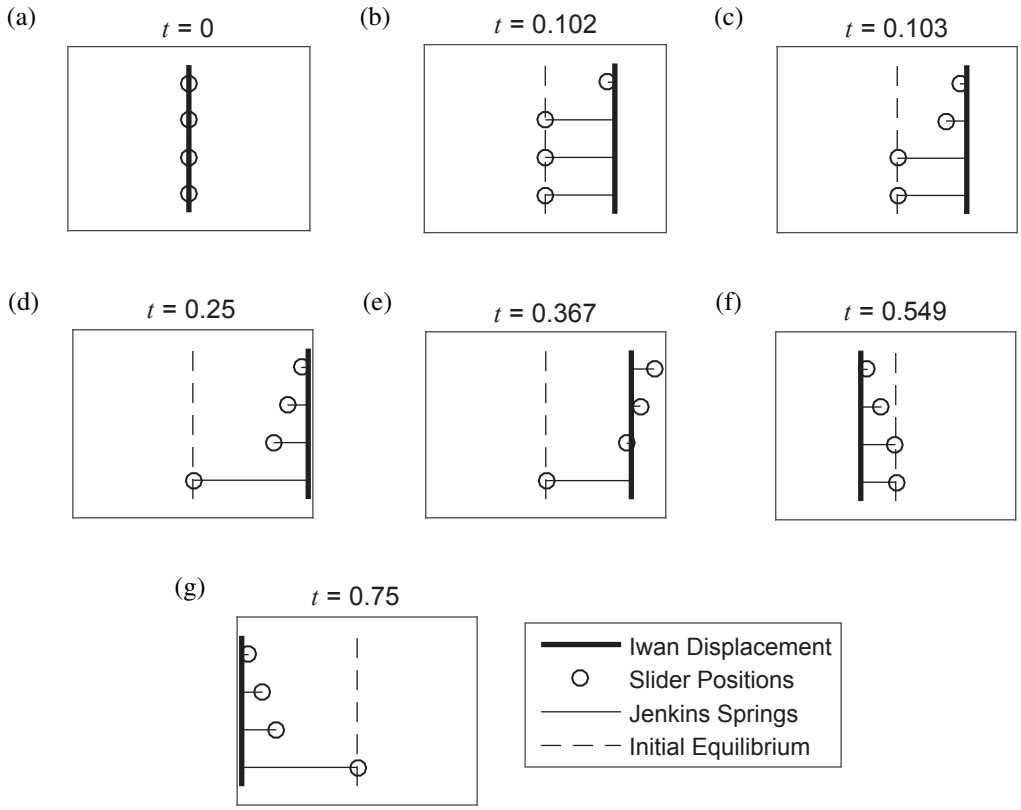

Figure 4.8: *Illustration of the evolution of the slider states over time in a period of initial loading and half a full cycle of steady-state displacement.*

stiffness contribution from that spring is lost in the total stiffness of the Iwan-type element. If $\theta = 1$ (four-parameter Iwan model), this jump in position would not occur, and the second slider would simply begin moving continuously with $u(t)$ from the initial equilibrium position. In an Iwan-type element with many more Jenkins sliders, it can be imagined that the sliders in between the four shown would slip one after another in rapid succession as u progresses towards the maximum displacement point.

By the time the maximum displacement point is reached (Fig. 4.8d), the third slider has slipped while the final slider remains stuck at the original equilibrium position. Figure 4.8d shows that the top three sliders each have increasing spring deflections based on their value of ϕ_i, so it can be imagined that the force drop (due to the jump in deflection from ϕ_i to $\theta\phi_i$) becomes increasingly significant as more sliders initiate slip.

At $t = 0.250$, load reversal occurs, and all sliders switch to the stuck state at their current positions. This leads to another regime of microslip-like behavior that is similar to initial loading, but the force-displacement curve is different because the sliders are now stuck at positions away from the zero equilibrium line. In Fig. 4.8e, the four sliders can still be seen in their stuck positions as $u(t)$ decreases. As $u(t)$ progresses towards the other maximum, the bottom three sliders begin to slip once more, though the Iwan-type element is required to cover a displacement of $\theta\phi_i + \phi_i$ in order to undo the spring deflections and then reengage the springs again in the opposite direction.

At $t = 0.549$, all springs that have slipped before have entered the slip state again. However, it is known from the initial loading cycle that the Iwan-type element never reaches a displacement that initiates slip in the fourth slider (as well as in other sliders below the third shown slider in models with more Jenkins elements). Hence, in the time between $t = 0.549$ and $t = 0.750$, the force only increases linearly with a slope consistent with the residual tangent stiffness, which explains the regime between points B and C (and D and A) in the hysteresis shown in Fig. 4.6. Again, for $\theta = 1$, this regime is virtually nonexistent because the position of the third slider at $t = 0.250$ would be displaced barely off from the initial equilibrium line, and therefore it would not slip again until $u(t)$ just about reaches the other maximum point. At $t = 0.750$, load reversal occurs, and the cycle between $t = 0.250$ and $t = 0.750$ repeats in the reverse direction.

4.3.2 Ring-Up and Ring-Down Behavior

An investigation on the five-parameter Iwan-type element during ring-up and ring-down displacement was conducted to examine any additional behavior that occurs when vibration amplitudes increase or decrease monotonically. Two different sinusoidal displacement signals were generated: one for the ring-up and the other for the ring-down. The ring-up signal was designed so that the amplitude increases linearly from a low boundary $u_L = 2 \times 10^{-4}$ to a high

boundary $u_H = 5.5 \times 10^{-4}$ in two cycles ($T = 2$) and then completes another cycle at the high boundary,

$$u_{\text{up}}(t) = \begin{cases} \left(u_L + (u_H - u_L)\frac{t}{T}\right)\cos\left(2\pi t\right), & 0 \leq t < T, \\ u_H \cos\left(2\pi t\right), & T \leq t \leq T + 1. \end{cases} \tag{4.23}$$

The third cycle is meant to create a complete, steady-state, hysteresis loop for comparison with the Mignolet hysteresis at amplitude u_H. Since the cosine function starts at a point of maximum displacement, the slider states were initialized by displacing the element from zero up to u_L. Similarly, the amplitude of the ring-down signal was designed to change linearly from u_H to u_L in two cycles followed by one cycle at u_L,

$$u_{\text{down}}(t) = \begin{cases} \left(u_H - (u_H - u_L)\frac{t}{T}\right)\cos\left(2\pi t\right), & 0 \leq t < T, \\ u_L \cos\left(2\pi t\right), & T \leq t \leq T + 1. \end{cases} \tag{4.24}$$

Again, the slider states in this case were initialized after displacing the element from zero to u_H.

An Iwan element with 10000 sliders (defined with uniform intervals in ϕ) and parameters $\chi = -0.6$, $\phi_{\text{max}} = 6 \times 10^{-4}$, $R = 7 \times 10^5$, and $S = 9 \times 10^3$ was used for this study. In a first run, θ was set to 1 to gain insight on the expected behavior of Segalman's four-parameter Iwan element in ring-up and ring-down displacement. The resulting force-displacement curves for ring-up and ring-down are shown in Fig. 4.9 along with the maximum force curve (Eq. (4.5)) and the Mignolet hysteresis loop at the final amplitude.

Looking first at the ring-up curve in Fig. 4.9a, The first half-cycle of the force-displacement curve (point A to C) starts on the maximum force curve and then arcs over to point B, the same point of maximum force of the opposite displacement. However, since the amplitude is still increasing, this reverse curve then traces the maximum force curve until load reversal occurs (point C). This tracing of the maximum force curve should make sense when considering the

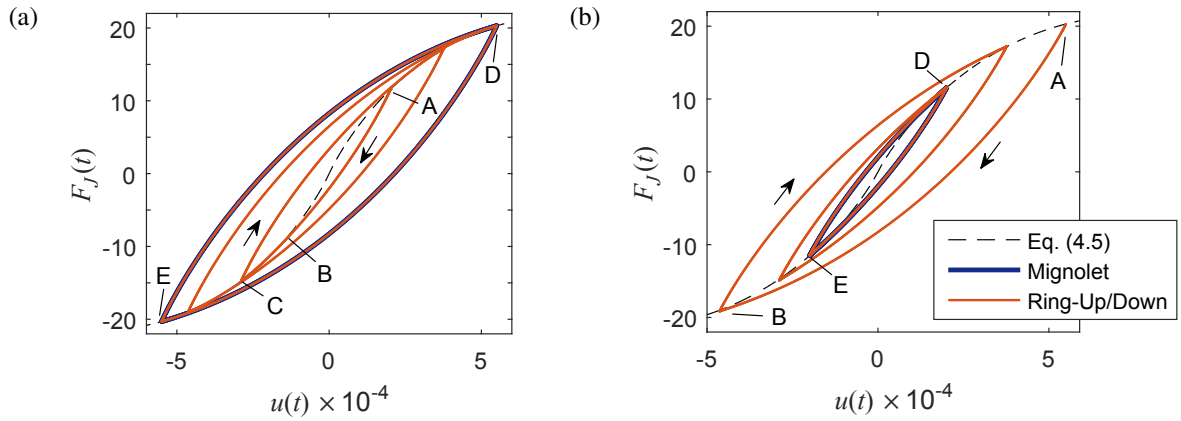

Figure 4.9: *(a) Ring-up and (b) ring-down force-displacement curves for* $\theta = 1$ *(four-parameter Iwan model).*

slider states. After load reversal, the sliders start slipping in a manner similar to that depicted between times $t = 0.25$ and 0.75 in Fig. 4.8, but the point at time $t = 0.75$ (which corresponds to point B in Fig. 4.9a) is no longer the maximum displacement for load reversal. Instead, the displacement of the Iwan element continues to grow, now newly initiating slip for those sliders still stuck on the initial equilibrium line. This behavior is reminiscent of initial loading behavior, the curve for which has been shown in Fig. 4.6 to trace that of Eq. (4.5) precisely.

Each path of forward and reverse loading in Fig. 4.9a can be described in the same manner: first starting from a point of initial loading, then arcing over to the opposite force at the opposite displacement, and finally following initial loading until load reversal. On a final note, in the third cycle of loading, where the displacement amplitude is constant at u_H, the hysteresis between points D and E can be seen to trace the Mignolet hysteresis exactly. This should come as no surprise given that the cycle starts on the initial loading curve.

Now examining the ring-down curve in Fig. 4.9b, the first half-cycle can be seen to start on the max-force curve (point A) and then arcs directly to point B, the point of load reversal that occurs near, but not on, the maximum force curve. This is hard to see in in Fig. 4.9b given the scale of the axes, but the consequence for the successive half-cycles is that each point of load reversal always occurs just shy of the max-force curve. Nonetheless, the close proximity

of these points with the max force curve provides a major advantage for computing the equivalent stiffness and dissipation of the Iwan element as it undergoes lightly-damped, ring-down vibration. Since the load reversal points are close enough so as to be considered *on* the max force curve, then each cycle of the ring-down is a close approximation of a Mignolet hysteresis constructed at an average amplitude level for that cycle. In effect, the free vibration of a four-parameter Iwan element exhibits practically the same amplitude-dependence in stiffness and energy dissipation per cycle as estimated by Segalman's analytical expressions for sinusoidal motion (Eq. (4.9) and (4.10)). This equivalence property, which is demonstrated in Section 4.5.2, validates the approach used in [32, 33, 57] to use those sinusoidal expressions to fit a modal four-parameter Iwan model to transient ring-down measurements on a bolted structure.

To see how well these observations hold up for the five-parameter model, the above analysis was repeated, but with $\theta = 0.3$. The resulting force-deflection curves are shown in Fig. 4.10. The ring-up curve, shown in Fig. 4.10a, displays much of the same fundamental behavior as the four-parameter model. Each forward and reverse path starts on the max-force curve (e.g. point A) and proceeds to the opposite displacement (e.g. point B) by following the same path as the Mignolet hysteresis, and thereafter following the path of initial loading until load reversal (e.g. point C). Again, the third cycle exactly traces the Mignolet hysteresis loop at the highest amplitude.

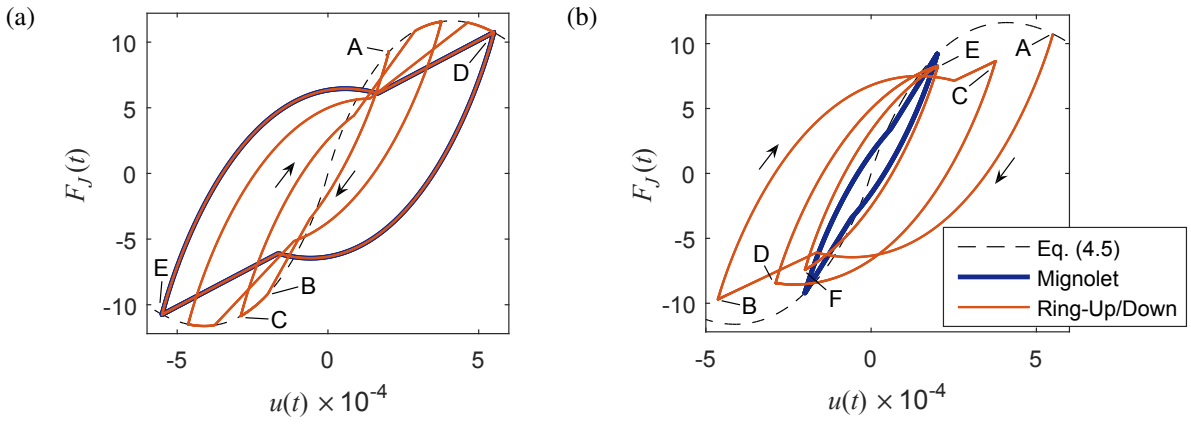

Figure 4.10: *(a) Ring-up and (b) ring-down force-displacement curves for* $\theta = 0.3$.

In stark contrast, the ring-down force-deflection curve (Fig. 4.10b) deviates from the behavior shown for the four-parameter Iwan model. In the first half-cycle (point A to point B), the steady-state hysteresis path is followed as usual, but load reversal occurs well before reaching the max-force curve. The ring-down curve also reverses early after the second half-cycle (point C), but it can also be seen that the regime of linear force versus displacement is shortening. This indicates that the displacement amplitude is reaching the point were the last slider to slip will further remain stuck. This occurs during the third half-cycle, whose reversal (point D) was reached before that last slider slipped. The remaining half-cycles continue this trend. Ultimately, the shape of the hysteresis in the third full-cycle (E to F to E) is completely different from the Mignolet hysteresis associated with the same displacement amplitude. Table 4.1 lists the secant slope (stiffness) and area enclosed (dissipation) by these two hysteresis cycles. The Mignolet hysteresis loop exhibits a higher secant stiffness than that of the ring-down curve, but the area enclosed by the ring down curve implies an energy dissipation rate that is almost twice that of the Mignolet hysteresis. This implies that the apparent stiffness during ring-down is less than that predicted by Mignolet's expression for secant stiffness (Eq. (4.7)), whereas the energy dissipated in ring-down will be higher than predicted by Eq. (4.8).

Table 4.1: *Comparison of Stiffness and Dissipation between the steady-state and ring-down hysteresis curves at* $u_0 = 2 \times 10^{-4}$. *The percent difference is taken with respect to the Mignolet's steady-state values.*

Property	Mignolet	Ring-Down	% Difference
Secant Slope	4.60×10^4	3.92×10^4	-14.8%
Area Enclosed	8.46×10^{-4}	1.60×10^{-3}	90.3%

The above results reveal an important caveat regarding Mignolet's steady-state assumptions for the five-parameter Iwan-type model. By allowing the kinetic friction force to be less than the maximum static friction force, the five-parameter model apparently shows more path-dependence than the four-parameter Iwan model. Whereas each cycle in a ring-down response of the four-parameter model is a good approximation of the hysteresis in the steady-state case,

the ring-down cycles in a general five-parameter model hardly resemble those of the Mignolet hysteresis. Therefore, Mignolet's expressions for steady-state stiffness and dissipation cannot be used to estimate the same properties in a ring-down response. Although the hysteresis loops cannot be matched after a ring-down, the opposite is true for ring-up. A cycle always starts from a state of initial loading during ring-up, so a subsequent switch to the steady state still allows the Iwan element to trace a hysteresis that is consistent with Mignolet's formulation. This demonstrates that Mignolet's steady-state stiffness and dissipation equations implicitly assume that the steady state was reached via a monotonically-increasing displacement amplitude.

4.4 Stiffness and Dissipation for Transient Ring-Down Analysis

Mignolet's steady-state stiffness and dissipation expressions cannot be used to estimate the ring-down behavior of the discrete five-parameter Iwan-type element, and this is a barrier for works similar to [32, 33, 57] that use these expressions to fit and validate the Iwan-type element against free-response decay measurements on a test structure. A new set of expressions must be derived that better captures the the behavior of the Iwan-type element during a ring-down.

Insight was gained by re-examining the ring-down hysteresis shown in Fig. 4.10b. An inspection of the shapes of each forward and reverse path in the hysteresis revealed that they have striking geometric similarity to one another. In fact, if the path from point A to point B was translated so that point A coincides with point C, then the shape of the path from C to D would be seen to align well with that of A to B. It was as if the path from A to B reached load reversal sooner in the path from C to D. A similar result occurs for the path from E to F if point A was made to coincide to point E, as illustrated in Fig. 4.11. Likewise, the paths from B to C, D to E, and F to E are also a translation and rotation transformation of A to B. Such a result gave rise to the hypothesis that if the ring-down was continued into lower amplitudes, then the shape of each half-cycle in the ring-down would continue to be well-approximated by a truncation of path A-B down to the current displacement amplitude. It follows, then, that

a steady-state hysteresis loop – one with the correct shape for the current amplitude after a ring-down response – can be constructed by connecting the truncated ends of the original and rotated A-B curves, as shown in Fig. 4.11.

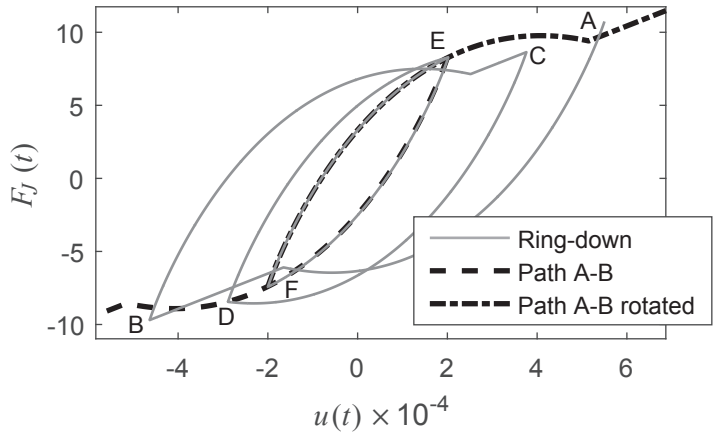

Figure 4.11: *Overlay of path A-B over the force-deflection curves of the third full cycle (E-F-E) of the ring-down.*

Since path A-B starts from a state initial loading, then its path is the same as that of the reverse monotonic loading path in the Mignolet hysteresis, which, in itself, is identical in shape to the forward monotonic loading path except rotated. In Section 4.4.1, a closed-form expression is first obtained for the forward monotonic loading curve of the Mignolet hysteresis. This is the force-deflection path that forms when the Iwan-type element is displaced monotonically from $u{=}{-}u_{\max}$ to $u{=}{+}u_{\max}$. This expression was then transformed mathematically to create a hysteresis loop for any arbitrary amplitude $u_0 < u_{\max}$. The new stiffness and dissipation equations were then derived in Section 4.4.2 by computing, respectively, the slope of the secant line and the area enclosed by this hysteresis.

4.4.1 Derivation of the Equation for the Forward Monotonic Loading Curve from a Mignolet Hysteresis

There exist two viable approaches to derive an equation for the forward curve. The first approach uses the continuous Iwan model formulation in which the constitutive function is evaluated with integrals, as in Eq. (4.1). The second approach uses the discretized formulation of the Iwan element given in Section 4.2.3. The discretized approach is presented here as it is easier to conceptualize the physics, but a simultaneous derivation was conducted for the continuous, integral approach. Additionally, the final force-displacement equation from the discretized approach is readily equatable to that of integral approach, as is shown near the end of this section.

In the discretized formulation, the ρ distribution was divided into N intervals of uniform length $\Delta = \phi_{\text{max}}/N$, as done in Section 4.2.3 except with ϕ_i defined as the right boundary of those intervals such that $\phi_i = i\Delta$. The Jenkins spring stiffness associated with each interval was then approximated as $k_i = \rho(\phi_i)\Delta = R\phi_i^{\chi}\Delta$ for $i = 1..N$, with the Dirac delta term accounted for by $k_{N+1} = S$ and $\phi_{N+1} = \phi_{\text{max}}$. In the continuous formulation, the springs were accounted for by a differential stiffness $\mathrm{d}k = \rho(\phi)\mathrm{d}\phi$.

The displacement of the Iwan element was allowed to increase monotonically from $-u_{\text{max}}$ to u_{max} in N steps (without loss of generalization), so that $u(j) = -u_{\text{max}} + j\epsilon$ where $\epsilon = 2u_{\text{max}}/N$. At the $j = 0$th step, the sliders up to $\phi_i \leq u_{\text{max}}$ were initialized to

$$x_i(j=0) = -u_{\text{max}} + \theta\phi_i \quad \text{for } i \leq \tfrac{u_{\text{max}}}{\phi_{\text{max}}}N, \tag{4.25}$$

while all others were initialized to zero,

$$x_i(j=0) = 0 \quad \text{for } i > \tfrac{u_{\text{max}}}{\phi_{\text{max}}}N. \tag{4.26}$$

Note that $u_{\max}/\phi_{\max}$ is the fraction of sliders whose initial conditions are offset from zero.

To sum up the spring forces that make up F_J in Eq. (4.18), the number of slipped sliders at load step j was determined. This was done by checking the slip condition at the jth step. Equation (4.25) was substituted into Eq. (4.16), ϕ_i was replaced with $i\Delta$, and i was isolated to get

$$i = \frac{u(j) - u_{\max}}{(1+\theta)\phi_{\max}} N = n_j, \tag{4.27}$$

which is the number of sliders that have slipped in the jth step. In other words,

$$\frac{n_j}{N} = \frac{u(j) - u_{\max}}{(1+\theta)\phi_{\max}} \tag{4.28}$$

is the fraction of all sliders that have slipped. This fraction only applies while $u(j) < \theta u_{\max}$, and the number of slipped sliders does not increase further as the displacement is increased beyond $\theta u_{\max}$. Let

$$\Phi(u) = \begin{cases} \dfrac{u - u_{\max}}{(1+\theta)\phi_{\max}} & \text{for } -u_{\max} \le u < \theta u_{\max}, \\ \dfrac{u_{\max}}{\phi_{\max}} & \text{for } \theta u_{\max} \le u \le u_{\max} \end{cases} \tag{4.29}$$

represent the evolution of the fraction of slipped sliders as u increases. Equation (4.29) is valid in both the discretized and continuous formulations.

The force components of F_J were then evaluated in the limit that N goes to infinity. Equation (4.19), becomes

$$F_{\text{slip}} = \lim_{N\to\infty} \sum_{i=1}^{\Phi(u)N} \theta R \phi_i^{\chi+1} \Delta = \int_0^{\Phi(u)\phi_{\max}} \theta R \phi^{\chi+1} \mathrm{d}\phi. \tag{4.30}$$

The stick component, Eq. (4.20), has two parts due to the division of sliders by initial state:

$$F_{\text{stick,1}} = \lim_{N\to\infty} \sum_{i=\Phi(u)N}^{\frac{u_{\max}}{\phi_{\max}}N} R\phi_i^{\chi}\left[u + u_{\max} - \theta\phi_i\right]\Delta = \int_{\Phi(u)\phi_{max}}^{u_{\max}} R\phi^{\chi}\left[u + u_{\max} - \theta\phi\right]\mathrm{d}\phi, \quad (4.31)$$

and

$$F_{\text{stick,2}} = \lim_{N\to\infty} \sum_{i=\frac{u_{\max}}{\phi_{\max}}N}^{N} uR\phi_i^{\chi}\Delta + Su = u\int_{u_{max}}^{\phi_{\max}} R\phi^{\chi}\mathrm{d}\phi + Su. \quad (4.32)$$

The integral forms were evaluated, and all the force components were summed to yield a closed-form expression for $F_J^{(f)}$, the forward monotonic loading curve. For $-u_{\max}\leq u < \theta u_{\max}$,

$$\begin{aligned} F_J^{(f)}(u, u_{\max}) = K_T u + \frac{R\left[\chi + 2 - \theta(\chi+1)\right]}{(\chi+2)(\chi+1)} u_{\max}^{\chi+2} \\ - \frac{R\left[(1-\theta)\chi + 2\right]^{\chi+2}}{(\chi+2)(\chi+1)}\left[\frac{u + u_{\max}}{1+\theta}\right]^{\chi+2}, \end{aligned} \quad (4.33a)$$

and

$$F_J^{(f)}(u, u_{\max}) = \frac{\theta R}{\chi+2} u_{\max}^{\chi+2} + \left(K_T - \frac{R u_{\max}^{\chi+1}}{\chi+1}\right) u \quad (4.33b)$$

for $\theta u_{\max}\leq u \leq u_{\max}$.

In Appendix H, Eq. (4.33) was checked against the force-deflection curve produced by a monotonically-loaded discrete Iwan-type element. They were found to give the same results.

4.4.2 Generalized Steady-State Equations for Stiffness and Energy Dissipation

To simplify the derivation for both the stiffness and the dissipation during a ring-down, the force-displacement curve given by Eq. (4.33) was shifted so that the point of origin lies at

[0,0]. That is, let

$$\tilde{F}(u, u_{\max}) = F_0(u_{\max}) + F_J^{(f)}(u - u_{\max}, u_{\max})$$
$$= \begin{cases} K_T u - \dfrac{R\left[(1-\theta)\chi + 2\right]}{(\chi+2)(\chi+1)} \left(\dfrac{u}{1+\theta}\right)^{\chi+2} & \text{for } u < (1+\theta)u_{\max}, \\ \dfrac{2\theta R}{\chi+2} u_{\max}^{\chi+2} + \left(K_T - \dfrac{R u_{\max}^{\chi+1}}{\chi+1}\right) u & \text{for } u \geq (1+\theta)u_{\max}. \end{cases} \tag{4.34}$$

represent the shifted curve. Then the secant stiffness at the current amplitude u_0 is

$$K_{\text{sec}}(u_0, u_{\max}) = \frac{\tilde{F}(2u_0, u_{\max})}{2u_0}$$
$$= \begin{cases} K_T - \dfrac{R\left[(1-\theta)\chi + 2\right]}{(\chi+2)(\chi+1)(1+\theta)} \left(\dfrac{2u_0}{1+\theta}\right)^{\chi+1} & \text{for } 0 \leq u_0 < \frac{1+\theta}{2} u_{\max} \\ \dfrac{\theta R u_{\max}^{\chi+2}}{(\chi+2)u_0} + K_T - \dfrac{R u_{\max}^{\chi+1}}{\chi+1} & \text{for } \frac{1+\theta}{2} u_{\max} \leq u_0 \leq u_{\max} \end{cases} \tag{4.35}$$

As shown in Fig. 4.12, the secant line connecting point of origin for the forward curve and the point of load reversal at $2u_0$ is characterized with a slope equal to K_{sec}. The reversal point at $2u_0$ then becomes the origin point for the reverse monotonic loading curve, which then terminates at the origin for the forward curve to complete the hysteresis loop. The secant line equally bisects the area enclosed by the forward and reverse curves, which conveniently allows the energy dissipation per cycle to be calculated as

$$E_{\text{dis}}(u_0, u_{\max}) = 2 \int_0^{2u_0} \left[\tilde{F}(u, u_{\max}) - u K_{\text{sec}}(u_0, u_{\max})\right] \mathrm{d}u$$
$$= \begin{cases} \dfrac{R\left[(1-\theta)\chi + 2\right](2u_0)^{\chi+3}}{(\chi+3)(\chi+2)(1+\theta)^{\chi+2}} & \text{for } 0 \leq u_0 < \frac{1+\theta}{2} u_{\max} \\ \dfrac{(1+\theta)(1-3\theta) R u_{\max}^{\chi+3}}{\chi+3} + \dfrac{4\theta R u_{\max}^{\chi+2}}{\chi+2} u_0 & \text{for } \frac{1+\theta}{2} u_{\max} \leq u_0 \leq u_{\max}. \end{cases} \tag{4.36}$$

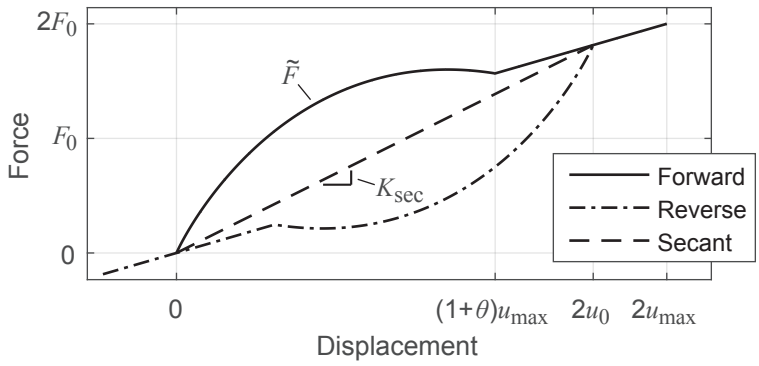

Figure 4.12: *Plot of the shifted forward Mignolet hysteresis curve, the reverse curve with origin at the $2u_0$ load reversal point, and the secant line connecting the load reversal points.*

Equations (4.35) and (4.36) represent the new stiffness and dissipation expressions that characterize the hysteresis of the five-parameter Iwan element during a ring-down response. The distinction is given by $u_{\max}$, the maximum displacement achieved in prior history. During ring-up, $u_{\max}$ is continually updated by the current amplitude u_0, so the shape of Eq. (4.33) changes accordingly. During ring-down, u_0 decreases from $u_{\max}$, and Eq. (4.33) becomes fixed. Accordingly, once $u_{\max}$ has been fixed, then Eqs. (4.35) and (4.36) show that an Iwan-type element will consistently exert the same stiffness and dissipation for any amplitude $u_0 < u_{\max}$, regardless of whether that amplitude was reached via a ring-up or ring-down response.

Note that, when $\theta = 1$, Eq. (4.35) and (4.36) reduce to Eq. (4.9) and (4.10) (Segalman's expressions). Additionally, K_{sec} and E_{dis} reduce to Eq. (4.7) and (4.8) (Mignolet's expressions) for the special case that $u_0 = u_{\max}$ (as in ring-up). It must be emphasized that Eqs. (4.35) and (4.36) are an improvement over Mignolet's expressions because Mignolet does not account for dependence on the past history of sliders in his formulation. The dependency on $u_{\max}$ in the new expressions reflects how further increases in the peak displacement serves to break new sliders free from their initial stuck positions, which in turn changes the behavior of the five-parameter Iwan-type model as Section 4.2.2 details.

4.5 Application to Transient Vibration Analysis

The results of Section 4.3, as well as Eq. (4.35) and (4.36), reveal that the transient behavior 5-parameter Iwan-type model has a stronger dependence on its history of slider states than the four-parameter model. In essence, the hysteresis loop outlined by a 5-parameter model after a ring-down response deviates significantly from the shape expected for the steady state after a ring up. Such behavior undoubtedly has ramifications that would alter the amplitude-dependent natural frequencies and damping ratios in a structural model containing one or more five-parameter Iwan-type elements.

To understand those ramifications on a basic level, the nonlinear dynamic response of a single-degree-of-freedom (SDOF) oscillator was simulated. The oscillator, illustrated in Fig. 4.13, holds unit mass, and is connected to ground with a linear spring of stiffness $k_\infty = 5 \times 10^5$ set in parallel with a discrete Iwan-type element. The equation of motion for the oscillator is

$$\ddot{y}(t) + k_\infty y(t) - F_J(y(t)) = F_{\text{ext}}(t), \tag{4.37}$$

where y and $\ddot{y}$ are, accordingly, the displacement and acceleration of the oscillator, F_{ext} is the applied loading, and F_J is the force exerted by the discrete Iwan element as in Eq. (4.18). The Iwan-type element contained $N = 500$ sliders constructed from a distribution function whose interval lengths increase geometrically in ϕ for $\alpha = 1.05$. The Iwan parameters are χ=$-$0.6, ϕ_{max}=6$\times$10^{-4}, R=7$\times$10^5, and S=9$\times$10^3. The parameter θ is varied in the analysis to follow.

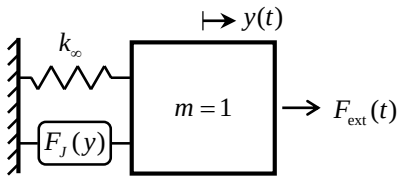

Figure 4.13: *Schematic of a SDOF oscillator with a discrete Iwan element in parallel with a spring.*

Work by the authors in [32, 33, 57] demonstrates that, in steady-state vibration, the Iwan element can be represented equivalently with a linear spring and viscous dashpot having an equivalent stiffness and energy dissipation given by Eq. (4.35) and (4.36) respectively. If $y(t)$ oscillates sinusoidally with amplitude y_0, then the circular natural frequency can be expressed as a function of amplitude with

$$\omega(y_0, y_{\max}) = \sqrt{k_\infty + K_{\text{sec}}(y_0, y_{\max})}, \tag{4.38}$$

where $y_{\max}$ is the maximum displacement amplitude achieved in prior history. The dashpot is then characterized with the damping coefficient of $2\omega(y_0, y_{\max})\zeta(y_0, y_{\max})$, where, for lightly-damped systems, the damping ratio is well-approximated as a ratio of the energy dissipated per cycle by the Iwan element versus the maximum kinetic energy at resonance, [57],

$$\zeta(y_0, y_{\max}) = \frac{E_{\text{dis}}(y_0, y_{\max})}{2\pi \left[\omega(y_0, y_{\max}) y_0\right]^2}. \tag{4.39}$$

Equations (4.38) and (4.39) thus establish the amplitude-dependent relationship of both frequency and damping for the oscillator system undergoing steady-state harmonic motion.

4.5.1 Forced Sinusoidal Response: Ring-Up Versus Ring-Down

Section 4.3 establishes that if the five-parameter Iwan element undergoes steady-state motion at a particular amplitude, then the apparent stiffness and dissipation it exhibits when that amplitude is reached during ring-down would differ from that of ring-up (except when $\theta = 1$). This section reaffirms that distinction by demonstrating its effects on the forced harmonic response of the SDOF oscillator.

Two different external forcing signals were generated: one for the ring-up response, and one for the ring-down response. For the ring-up response, a simple sinusoidal function was used to excite the SDOF system (initialized at rest) at the resonance frequency associated with

a target amplitude of $y_0 = 1 \times 10^{-4}$,

$$F_{\text{ext}}(t) = F_\omega \sin\left(\omega(y_0, y_0)t\right). \tag{4.40}$$

According to linear, harmonic vibration theory, the force required to achieve the target amplitude at resonance must be such that it balances the viscous damping term in the equation of motion,

$$F_\omega = 2\zeta(y_0, y_0)\left[\omega(y_0, y_0)\right]^2 y_0 = \frac{E_{\text{dis}}(y_0, y_0)}{\pi y_0}. \tag{4.41}$$

The input force for ring-down was designed to force the oscillator down to the same driving frequency and forcing amplitude as in Eq. (4.40). This was done to demonstrate that a ring-down loading generally produces a different response than that for ring-up, even if the system is excited with the same force in the steady state. To achieve the ring-down, the SDOF system was first excited with a higher loading amplitude $F_H > F_\omega$, which then ramped down linearly in time to F_ω. The form is

$$F_{\text{ext}}(t) = \begin{cases} \left[F_H - (F_H - F_\omega)\frac{t}{T}\right]\sin\left(\omega(y_0, y_0)t\right) & \text{for } t < T, \\ F_\omega \sin\left(\omega(y_0, y_0)t\right) & \text{for } t \geq T. \end{cases} \tag{4.42}$$

Two sets of ring-up and ring-down simulations were performed. For the first set, the θ parameter in the Iwan element was set to 1 to simulate the response using Segalman's four-parameter model. With $\theta = 1$, the value for the driving frequency is $\omega = 805.4$ and the loading magnitude is $F_\omega = 0.6663$. In the second set, θ was adjusted to 0.5, which gives $\omega = 801.5$ and $F_\omega = 0.6247$. The ring-down amplitude for both cases was initialized at $F_H = 6$ and ramped down to F_ω in a period of $T = 2$. For all loading and θ cases, Eq. (4.37) was integrated numerically using an average-acceleration Newmark method [46] to retrieve the simulated response.

The ring-up and ring-down displacements for $\theta = 1$ are shown in Fig. 4.14. Here it can be

seen that the response of the oscillator converges to the same steady-state behavior, regardless of ring-up or ring-down, under the influence of the four-parameter Iwan element. These results are consistent with the discussion made in Section 4.3.2 regarding Fig. (4.9). Additionally, the steady-state amplitude of both displacement signals achieves the target amplitude $y_0{=}1{\times}10^{-4}$, which reflects the accuracy of selecting the resonance frequency and loading based on the amplitude-dependent stiffness and dissipation in the Iwan element.

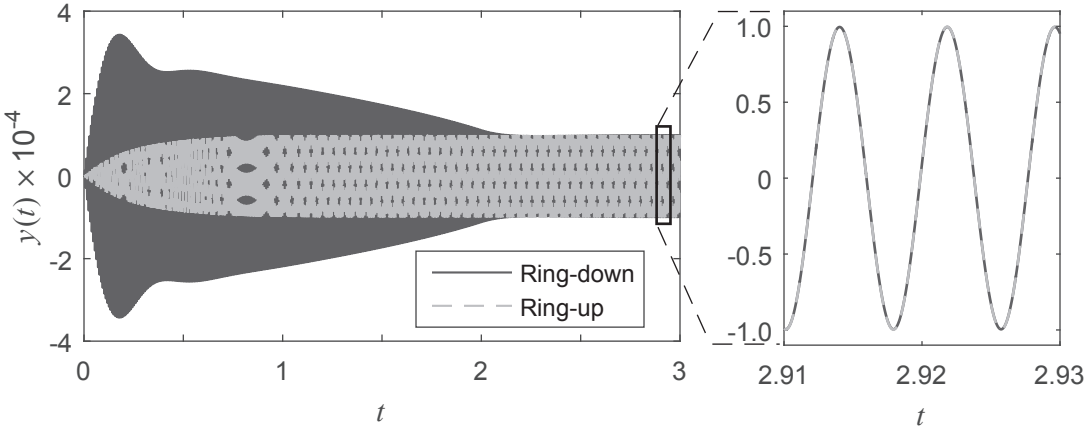

Figure 4.14: *Comparison of ring-up versus ring-down response to sinusoidal excitation in a SDOF oscillator with a four-parameter Iwan model ($\theta = 1$) in parallel with a spring.*

In contrast, Fig. 4.15 shows that a discrepancy appears between the steady-state responses when $\theta = 0.5$. The amplitude of the ring-up response is at $y_0{=}1{\times}10^{-4}$ as expected, but, because the driving frequency and loading were not adjusted for $y_{\max}$, the amplitude of the steady-state response is off target. Not only is the response amplitude lower (which implies more damping than usual), but a slight phase lag with respect to the ring-up response can be seen, indicating that the driving frequency is no longer at the resonant frequency. All of this shows that the steady-state stiffness and dissipation exerted by the Iwan-type element after a ring down cannot be assumed the same as that after a ring up to the same amplitude. Mignolet's stiffness and dissipation equations, which are a special case of Eq. (4.35) and (4.36), only work when the current amplitude is the maximum-achieved amplitude, and therefore they are inadequate for predicting ring-down stiffness and dissipation.

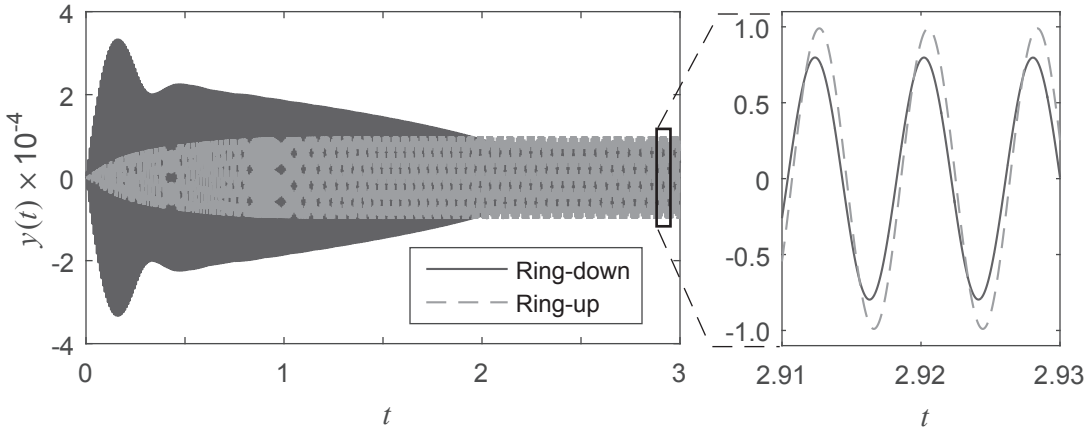

Figure 4.15: *Comparison of ring-up versus ring-down response to sinusoidal excitation in a SDOF oscillator with a five-parameter Iwan model ($\theta = 0.5$) in parallel with a spring.*

4.5.2 Free Response: Instantaneous Natural Frequency and Damping

Although it is possible to conduct a frequency sweep in a forced response simulation on the SDOF oscillator in order to confirm Eq. (4.35) and (4.36) for a wide range of amplitude levels, the execution of such using a numerical integrator would be a time-consuming effort since the frequency sweep must be slow enough to ensure a quasi-steady-state response. Rather, it is far more efficient simply to measure the instantaneous frequency and damping from a simulated free-response decay signal, and then confirm these values against Eq. (4.38) and (4.39). The latter option was studied by the authors in [57], who showed that the instantaneous natural frequency and damping measured from a free-response of the SDOF oscillator was well-approximated by Eq. (4.38) and (4.39) when $\theta = 1$. In this section, a similar procedure is used to verify the equations for more general values of θ.

The free-response of the SDOF oscillator was simulated after exciting the system at rest with an impact in the shape of a half-period sine wave. Specifically,

$$F_{\text{ext}}(t) = \begin{cases} 100\sin(200\pi t) & \text{for } t < \frac{1}{200}, \\ 0 & \text{otherwise.} \end{cases} \tag{4.43}$$

Three different simulations were conducted that define $\theta = 1$, 0.5, and 0.2. For each case, the free-response was obtained by integrating Eq. (4.37) for $t \in [0, 10]$ using the Newmark method. In the resulting simulated responses, peak displacements of $y_{\text{max}} = 2.676 \times 10^{-4}$, 2.704×10^{-4}, and 2.721×10^{-4} were observed, respectively, for each θ case above.

After completing the simulations, the instantaneous frequency and damping was extracted from each free-response signal using Feldman's Hilbert transform method [43, 44]. In this method, a model of the form $y_{\text{fit}} = \exp\left(\psi_r(t) + \mathrm{i}\psi_i(t)\right)$ was fitted to each free-response signal, where $\psi_r(t)$ is the amplitude component, $\psi_i(t)$ is the phase component, and $\mathrm{i} = \sqrt{-1}$. From these component functions, the instantaneous amplitude of the fitted signal can be retrieved through

$$\bar{A}(t) = \exp\left(\psi_r(t)\right), \tag{4.44}$$

the instantaneous natural frequency is

$$\bar{\omega}(t) = \frac{\mathrm{d}\psi_i(t)}{\mathrm{d}t}, \tag{4.45}$$

and the instantaneous damping ratio is

$$\bar{\zeta}(t) = \frac{\gamma(t)}{\sqrt{(\bar{\omega}(t))^2 + (\gamma(t))^2}}, \qquad \gamma(t) = \frac{\mathrm{d}\psi_r(t)}{\mathrm{d}t}. \tag{4.46}$$

This work used the piecewise linear functions discussed in [57] as the form of $\psi_r(t)$ and $\psi_i(t)$, though the reader is referred to the works of [32, 33, 44] for other viable functional forms with which to fit the free-response signals.

As an illustration, Fig. 4.16 shows the amplitude envelope fitted over the velocity response of the $\theta = 1$ simulation, and the instantaneous frequency and damping extracted from that fit. The displacement signal contained an equilibrium offset from zero that became significant at the lower amplitudes. This equilibrium shift distorts the amplitude envelope (and the damping curve by extension) so the velocity signal was used since it oscillates consistently about the zero

equilibrium. Although $\bar{A}(t)$ was fitted over the velocity envelope, the displacement envelope $y_0(t)$ was retrieved using the relation $y_0(t) = \bar{A}(t)/\bar{\omega}(t)$ [57]. In Fig. 4.16, it can be seen that the fitted models result in a smooth representation of the velocity envelope, the natural frequency, and the damping ratio. The instantaneous frequency increases up to an asymptote as the amplitude decreases, and the damping due to the Iwan element also becomes smaller, which are the expected amplitude trends for both properties.

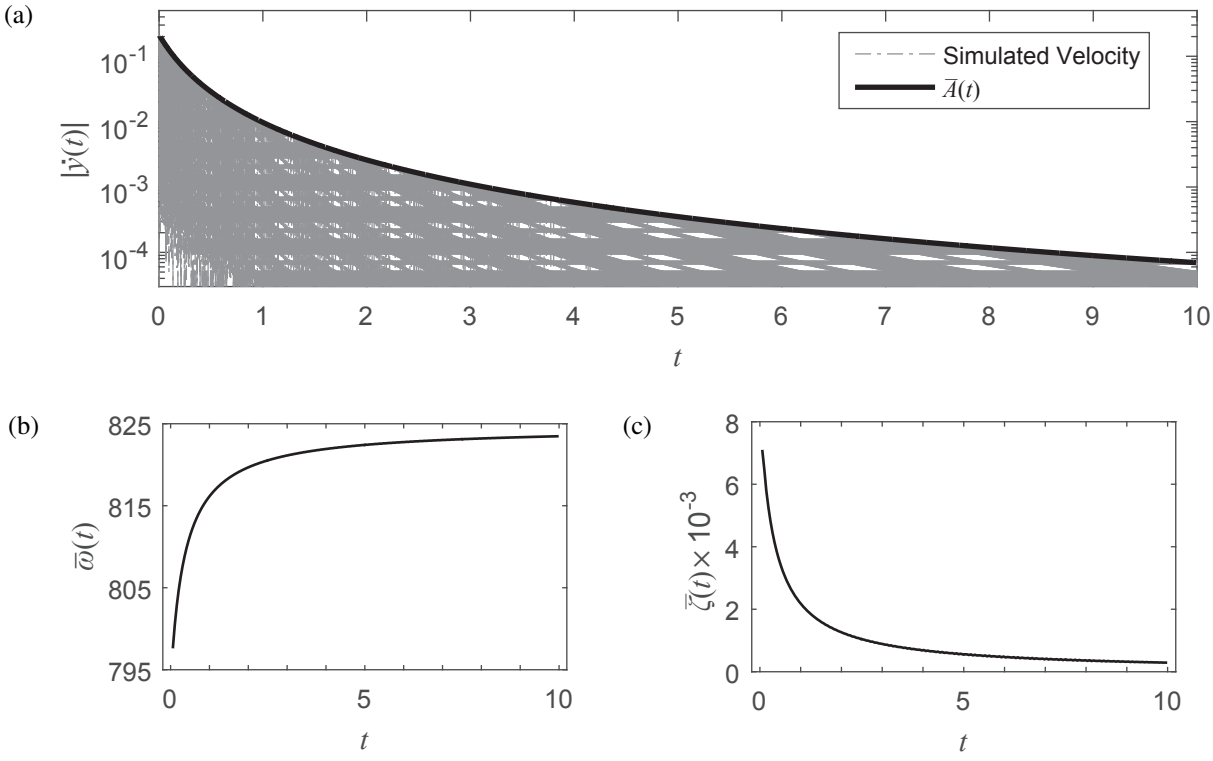

Figure 4.16: *Measurements on the instantaneous (a) velocity amplitude, (b) natural frequency, and (c) damping ratio as obtained from the free-response of the SDOF oscillator using the Hilbert transform method. The velocity signal shown here is from the simulation defining* $\theta = 1$.

Finally, Fig. 4.17 plots $\bar{\omega}(t)$ and $\bar{\zeta}(t)$ versus $y_0(t)$, and compares them to those curves retrieved from Eq. (4.38) and (4.39) with $y_0(t)$ as the input. In comparing the two sets of curves, it can be seen that Eq. (4.38) and (4.39) do well in capturing the amplitude-dependence of frequency and damping during free-response. There is some error in the higher amplitudes (the beginning of the response), with ω overestimating $\bar{\omega}$ by an average of 0.22% and ζ un-

derestimating $\bar{\zeta}$ by an average of 6.2% at $y_0 = 10^{-4}$, but these errors are acceptably small and gradually decrease as the free-response decays into lower amplitudes. Overall, these plots provide a strong argument that the equivalence of amplitude-dependent stiffness and energy dissipation between a ring-down response and the steady state is upheld well for Eq. (4.35) and (4.36).

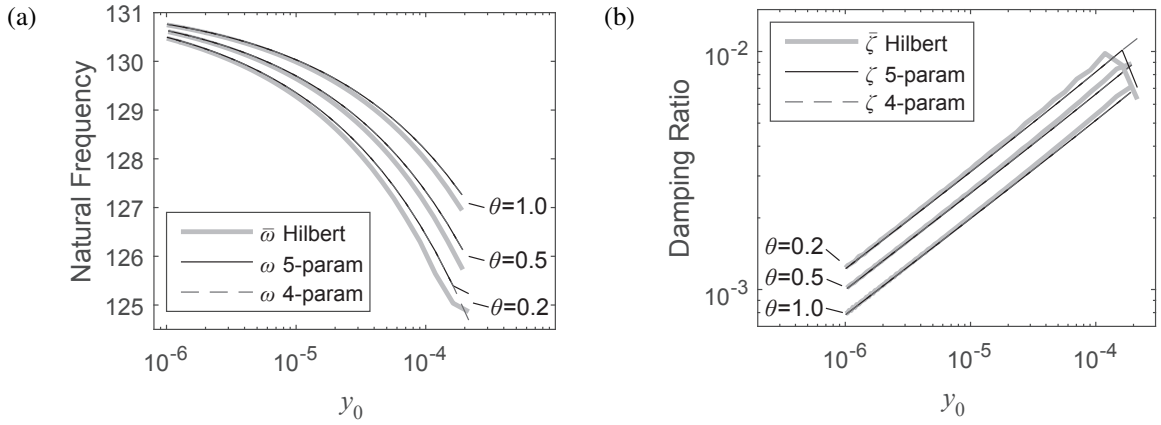

Figure 4.17: *Comparison between Hilbert and the closed-form expressions for amplitude-dependent (a) natural frequency and (b) damping ratio for different values of θ. The lines corresponding to the 4-parameter Iwan model use parameters $\theta = 1$ and $R = \bar{R}$ to show equivalence in frequency and damping with that of the 5-parameter model.*

A peculiar detail to note regarding the $\theta = 0.2$ curves is that both the stiffness and the damping experience a sudden slope change at the highest amplitudes, and this phenomenon has been captured in both the Hilbert fits and the closed-form equations. This slope difference is due to the switch from the $y_0 \geq \frac{1+\theta}{2} y_{\max}$ amplitude domain to the $y_0 < \frac{1+\theta}{2} y_{\max}$ domain, as similarly defined for u in Eq. (4.35) and (4.36). For damping, it can be observed that the regime of $y_0 \geq \frac{1+\theta}{2} y_{\max}$ has negative slope with respect to amplitude; the damping decreases as amplitude increases. This trend is counter to the behavior typically observed from jointed structures in experiments, and this calls into question whether the five-parameter Iwan model is an appropriate joint model at least within this regime.

On the other hand, the frequency and damping are governed by the latter domain ($y_0 < \frac{1+\theta}{2} y_{\max}$) for a great majority of the simulation because the response decays quickly enough

that the former domain is departed swiftly. Even for very small values of θ, the current amplitude would only need to drop to half of the maximum-achieved amplitude in order to switch domains. Hence, it is reasonable to assume that the amplitude-dependent stiffness and dissipation in a transient free-response could be approximated entirely by the $u_0 < \frac{1+\theta}{2} u_{\max}$ domain, which provides the advantage that $u_{\max}$ need not be a requisite parameter in order to compute K_{sec} and E_{dis}.

Unfortunately, the dominance of the $u_0 < \frac{1+\theta}{2} u_{\max}$ domain during free-response also reveals a weakness of the five-parameter Iwan element. The weakness arises from the functional similarity of K_{sec} and E_{dis} within this domain versus Segalman's expressions for stiffness and dissipation for the four-parameter model. Defining

$$\bar{R} = \frac{R\left[(1-\theta)\chi + 2\right] 2^{\chi+1}}{(1+\theta)^{\chi+2}}, \tag{4.47}$$

then, for $0 \leq u_0 < \frac{1+\theta}{2} u_{\max}$, Eq. (4.35) and (4.36) reduce to

$$K_{\text{sec}} = K_T - \frac{\bar{R} u_0^{\chi+1}}{(\chi+2)(\chi+1)}, \tag{4.48}$$

$$E_{\text{dis}} = \frac{4\bar{R} u_0^{\chi+3}}{(\chi+3)(\chi+2)}, \tag{4.49}$$

which have the exact same forms as Eq. (4.9) and (4.10), respectively. For the three parameter cases investigated, $\bar{R}$ takes on values of 1.088×10^6, 8.901×10^5, and 7.000×10^5 for $\theta = 0.2$, 0.5, and 1.0, respectively. If these values of $\bar{R}$ are substituted for R in K_{sec} and E_{dis}, and if Eq. (4.38) and (4.39) are recomputed for $\theta = 1$ (for a four-parameter Iwan model), then Fig. 4.17 shows that the resulting frequency and damping curve overlays exactly on the curve from the corresponding five-parameter model. This demonstrates that, for any parameter set specified for the five-parameter model, the power-law behavior it exhibits when $u_0 < \frac{1+\theta}{2} u_{\max}$ can be captured by an equivalent four-parameter Iwan model having parameter $R = \bar{R}$

Effectively, the intended benefit of introducing the θ parameter is lost when displacement amplitudes drop below the $\frac{1+\theta}{2}u_{\max}$ threshold. Hence, for transient ring-down simulations, and even for forced response simulations whose amplitude drops below that threshold, the five-parameter Iwan element introduces stiffness and damping trends that are no different than those of the simpler four-parameter model.

4.6 Conclusion

This paper presents an investigation on the effects that the stiction parameter in Mignolet's five-parameter Iwan-type model has on the stiffness and energy dissipation that the model exerts in a general transient setting. To facilitate the investigation, a computational element of the five-parameter model was formulated that uses a discretized distribution of Jenkins sliders whose slip behavior embodies the stiction phenomenon. The results of a study on the static and transient behavior of the Iwan-type element revealed that the five-parameter model is much more path-dependent than the four-parameter Iwan model. The effect of stiction alters the physics of the model such that the effective stiffness and dissipation it exhibits in the steady-state after a ring-down loading differs from that after a ring-up. This key finding was overlooked in Mignolet's paper, which only considered a steady state that was reached via a monotonic increase in amplitude.

Using the insight gained in observing the evolution of the force-deflection hysteresis of the Iwan-type element during ring-down displacement, new stiffness and dissipation equations were derived that better account for the path dependence inherent in the five-parameter model. The equations reveal that amplitude-change in stiffness and dissipation is contingent on the maximum displacement achieved in prior history. Higher displacements mean that new Jenkins sliders with higher slip thresholds break contact and, thus, alter the hysteresis of the Iwan-type element.

The new stiffness and dissipation expressions were then used to accurately predict the

amplitude-dependence in the natural frequency and damping of a singe-degree-of-freedom oscillator (connected to ground with an Iwan-type element) undergoing ring-down in response to an impact. Shortly after impact occurs, the Iwan-type element exhibits power-law damping behavior with amplitude: a relationship that can be modeled equivalently with a four-parameter Iwan model. Consequently, the advantage posed by Mignolet's stiction parameter, which is to weaken the coupling between stiffness and dissipation in an Iwan model, vanishes both in a transient ring-down response and in a forced response where the displacement amplitude falls below the maximum achieved in prior history.

Appendices

Appendix A

Overview of the Four-Parameter Iwan Model

In general, an Iwan element [28] is a one-dimensional, parallel arrangement of elastoplastic (Jenkins) elements as seen in Fig. A.1. These elastoplastic elements consist of a spring, all having uniform stiffness, in series with a friction slider having slider displacement x and a certain slip threshold ϕ. If the ϕ for all elastoplastic elements is the same, then all sliders slip at the same Iwan element deflection u, and the Iwan element can be modeled equivalently by a single elastoplastic element. By setting different values of ϕ for each element, then the individual sliders slip one-by-one as u deflects more, causing the Iwan element to lose stiffness in a piecewise manner until macroslip. In the limit that an Iwan element contains an infinite number of elastoplastic elements, the force-deflection curve (and, by extension, the hysteresis) of the Iwan element can be modeled continuously by assigning a population distribution function, $\rho(\phi)$, to define the relative proportion of sliders that slip at ϕ.

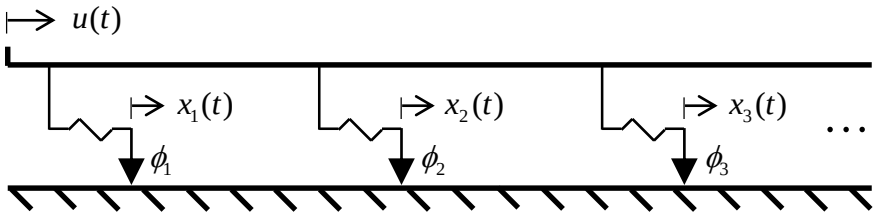

Figure A.1: *Schematic of the parallel-series Iwan model. Individual elastoplatic elements have the same spring stiffness but have a unique displacement threshold ϕ_i at which the contact (shown with a triangle) begins to slide.*

Segalman's formulation defines ρ as a truncated power-law terminated with a Dirac delta

function of strength S at the threshold of macroslip, $\phi_{\max}$,

$$\rho(\phi) = R\phi^{\chi}\left[H(\phi) - H(\phi - \phi_{\max})\right] + S\delta(\phi - \phi_{\max}), \tag{A.1}$$

where $H(\cdot)$ is the Heaviside step function [31]. A graphical representation of this function is shown in Fig. A.2(a). Segalman then derives the force exerted by the Iwan element as

$$F_I(u(t)) = \int_0^{\infty} \rho(\phi)\left[u(t) - x(t,\phi)\right]\mathrm{d}\phi = \int_0^{\phi_{\max}} R\phi^{\chi}\left[u(t) - x(t,\phi)\right]\mathrm{d}\phi + S\left[u(t) - x(t,\phi_{\max})\right]. \tag{A.2}$$

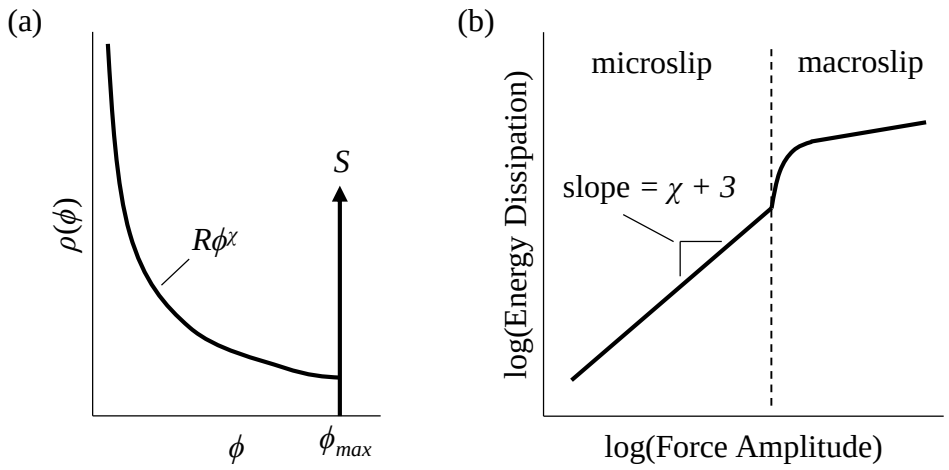

Figure A.2: *(a) The population distribution function of slider strengths associated with the four-parameter Iwan model, and (b) the resulting log-log energy dissipation per cycle for that model.*

Although this constitutive function was formulated using a continuous distribution of an infinite number of elastoplastic sliders, a numerical implementation of Eq. (A.2) is evaluated by tracking x for a finite number of elements. 200 sliders were assigned to all Iwan elements in the simulations in this work to approximate a smooth force-deflection curve.

The four parameters, R, S, $\phi_{\max}$, and χ, can be converted to more physically meaningful parameters, F_S, K_T, χ, and β. Here, F_S refers to the minimum force required to initiate macroslip, K_T is the tangent stiffness of the joint, χ is the exponent of the power-term, and β

is the ratio of the Dirac delta strength (related to macroslip) to the power-law strength [31],

$$F_S = \frac{R\phi_{\max}^{\chi+2}}{\chi+2} + S\phi_{\max}, \tag{A.3}$$

$$K_T = \frac{R\phi_{\max}^{\chi+1}}{\chi+1} + S, \tag{A.4}$$

$$\beta = \frac{S(\chi+1)}{R\phi_{\max}^{\chi+1}}. \tag{A.5}$$

The reader is referred to [31] for a more rigorous treatment of the four-parameter Iwan model, but there are a few important ideas that should be emphasized in this brief treatment. Each elastoplastic element in an Iwan element can be thought of as representing a microscopic region of slip within the joint interface, and the gradual accumulation of sliders that pass the threshold of slip as the Iwan element flexes gives rise to microslip behavior. Equation (A.1) was chosen so as to induce power-law energy dissipation (and power-law damping by extension) with respect to amplitude, a phenomenon that has been observed in several structures with metal-on-metal joints [2, 32, 33]. The parameter χ can be observed directly though this relationship, as Segalman derived a log-log slope of $\chi + 3$ in the microslip regime [31], as seen in Fig. A.2(b).

When all sliders have passed the threshold for slip (that is, when the last slider defined with $\phi_{\max}$ reaches its threshold), then the Iwan element enters macroslip, the model for which is equivalent to Coulomb friction. Experimentally, it is difficult to observe macroslip behavior from the response to an impact on a structure, so the Coulomb model for macroslip in cyclic loading has not yet been verified for impulse-type excitations. Despite this, the finite element models studied in this work all used four-parameter Iwan elements to represent physical joints, so the modal Iwan model was expected to capture their macroslip behavior to a good level of accuracy.

Appendix B

Derivation of Equivalent Modal Damping from Energy Dissipation per Cycle

While previous works focused on energy dissipation, which is a dimensional quantity, the authors found that it is convenient to express the effects of dissipation as an equivalent damping ratio for the mode in question. An expression for equivalent damping can be calculated from energy dissipation per cycle using the approach by Deaner et al. [32], which is explained as follows. Consider the free response of a certain mode and presume that the amplitude decays very little (e.g. very light damping) within one response cycle. Then the velocity coordinate governing a particular mass-normalized mode shape within that cycle can be expressed in an average sense over time t within that single cycle as

$$\dot{q}(t) = |\dot{q}| \sin(\omega_d t + \theta), \tag{B.1}$$

where $|\dot{q}|$ is the modal velocity amplitude, ω_d is the damped natural frequency, and θ is an arbitrary phase. The energy dissipated within one cycle is then

$$D = \int_t^{t+\frac{2\pi}{\omega_d}} F_v(\tau)\dot{q}(\tau)\mathrm{d}\tau, \tag{B.2}$$

If all sources of dissipation for this mode are approximated with an equivalent linear viscous damper, then the viscous damping force is $F_v(t) = C\dot{q}(t) = 2\zeta\omega_n\dot{q}(t)$, where ω_n is the undamped natural frequency and ζ is the equivalent modal damping ratio. Substituting this equa-

tion for F_v in Eq. (B.2) and evaluating the integral gives

$$D = 2\pi\zeta\frac{\omega_n}{\omega_d}|\dot{q}|^2 = 2\pi\frac{\zeta}{\sqrt{1-\zeta^2}}|\dot{q}|^2, \tag{B.3}$$

while noting that the definition $\omega_d = \omega_n\sqrt{1-\zeta^2}$ from linear vibration theory is used. Equation (B.3) is dimensionally correct only when $\dot{q}(t)$ governs a mass-normalized mode shape; the quantity $|\dot{q}|^2$ is scaled correctly as such.

Rearranging Eq. (B.3), and extending the equation for any arbitrary cycle in a free response with instantaneous amplitude $|\dot{q}(t)|$, the effective damping ratio can be expressed over all time as

$$\zeta(t) = \frac{D(t)}{\sqrt{4\pi^2|\dot{q}(t)|^4 + \left(D(t)\right)^2}}. \tag{B.4}$$

For lightly damped modes, the kinetic energy quantity $4\pi^2|\dot{q}(t)|^4 \gg \left(D(t)\right)^2$, so Eq. (B.4) can be simplified to

$$\zeta(t) = \frac{D(t)}{2\pi|\dot{q}(t)|^2}. \tag{B.5}$$

It may be convenient to express $\zeta(t)$ in terms of displacement amplitude $|q(t)|$ or acceleration amplitude $|\ddot{q}(t)|$. Equation (B.1) may be differentiated or anti-differentiated with respect to t to obtain a relationship between these quantities and the velocity amplitude,

$$\omega_d(t)|q(t)| = |\dot{q}(t)| = \frac{|\ddot{q}(t)|}{\omega_d(t)}. \tag{B.6}$$

Appendix C

Amplitude Plots for the Three-Mass System

Figure C.1 originates from the analysis in Section 2.3.1, and it shows the modal Iwan model analytical fits to the simulations that selectively excite modes 1 and 3 each at a time.

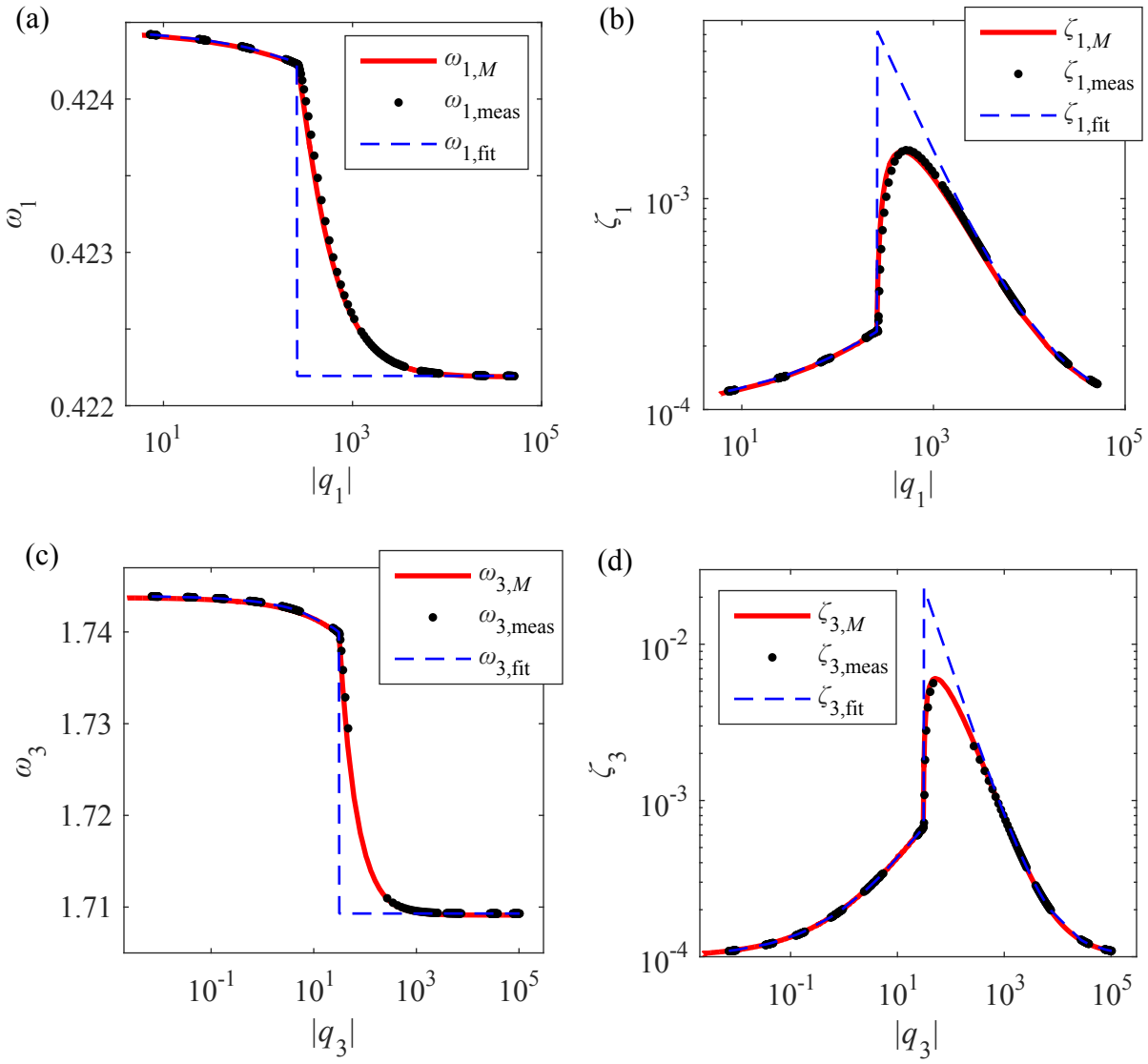

Figure C.1: *(a, c) Natural frequency and (b, d) damping ratio versus displacement amplitude for selective excitation of (a, b) mode 1 and (c, d) mode 3 in the three-mass system.*

Appendix D

Simulation Parameters and Amplitude Plots for the Sumali Beam System

The frequency and damping versus amplitude curves for the modal Iwan models of the seventh and ninth modes in the Sumali beam finite element model are shown below. Table D.1 lists the simulation parameters for the mode shape excitation simulations in Section 2.3.2. The frequency and damping curves for modes 7 and 9 are plotted and fitted in Fig. D.1. Table D.2 lists the parameters for the discrete impulse simulations from Section 2.3.2.

Table D.1: *Parameters for the mode shape excitation simulations of the Sumali beam system. Scalar p and vector $\boldsymbol{\varphi}$ are the force multiplier value and mode shape, respectively, substituted into Eq. (2.27)*

Simulation Number	p [N kg$^{-1/2}$]	$\boldsymbol{\varphi}$	Time Step [s]	Number of Steps
1	3361	$\boldsymbol{\varphi}_{\infty 7}$	1×10^{-5}	200,000
2	1681	$\boldsymbol{\varphi}_{\infty 7}$	5×10^{-6}	200,000
3	1008	$\boldsymbol{\varphi}_{\infty 7}$	5×10^{-6}	200,000
4	336.1	$\boldsymbol{\varphi}_{\infty 7}$	5×10^{-6}	100,000
5	67.23	$\boldsymbol{\varphi}_{\infty 7}$	5×10^{-6}	50,000
6	2.756	$\boldsymbol{\varphi}_{07}$	5×10^{-6}	200,000
7	0.3361	$\boldsymbol{\varphi}_{07}$	3×10^{-5}	133,333
8	0.03361	$\boldsymbol{\varphi}_{07}$	5×10^{-5}	200,000
9	10,080	$\boldsymbol{\varphi}_{\infty 8}$	1×10^{-5}	200,000
10	3361	$\boldsymbol{\varphi}_{\infty 8}$	1×10^{-5}	100,000
11	1681	$\boldsymbol{\varphi}_{\infty 8}$	5×10^{-6}	200,000
12	336.1	$\boldsymbol{\varphi}_{\infty 8}$	5×10^{-6}	68,000
13	67.23	$\boldsymbol{\varphi}_{\infty 8}$	5×10^{-6}	50,000
14	10.08	$\boldsymbol{\varphi}_{08}$	8×10^{-6}	100,000
15	1.681	$\boldsymbol{\varphi}_{08}$	1×10^{-5}	200,000
16	1.008	$\boldsymbol{\varphi}_{08}$	4.7×10^{-5}	106,383
17	0.06723	$\boldsymbol{\varphi}_{08}$	4.7×10^{-5}	212,766
18	26,890	$\boldsymbol{\varphi}_{\infty 9}$	3×10^{-6}	333,333
19	6723	$\boldsymbol{\varphi}_{\infty 9}$	3×10^{-6}	166,666
20	1681	$\boldsymbol{\varphi}_{\infty 9}$	3×10^{-6}	69,333
21	67.23	$\boldsymbol{\varphi}_{\infty 9}$	5×10^{-6}	20,000
22	3.361	$\boldsymbol{\varphi}_{09}$	1×10^{-5}	100,000
23	0.2689	$\boldsymbol{\varphi}_{09}$	1×10^{-5}	100,000
24	0.06723	$\boldsymbol{\varphi}_{09}$	1×10^{-5}	200,000

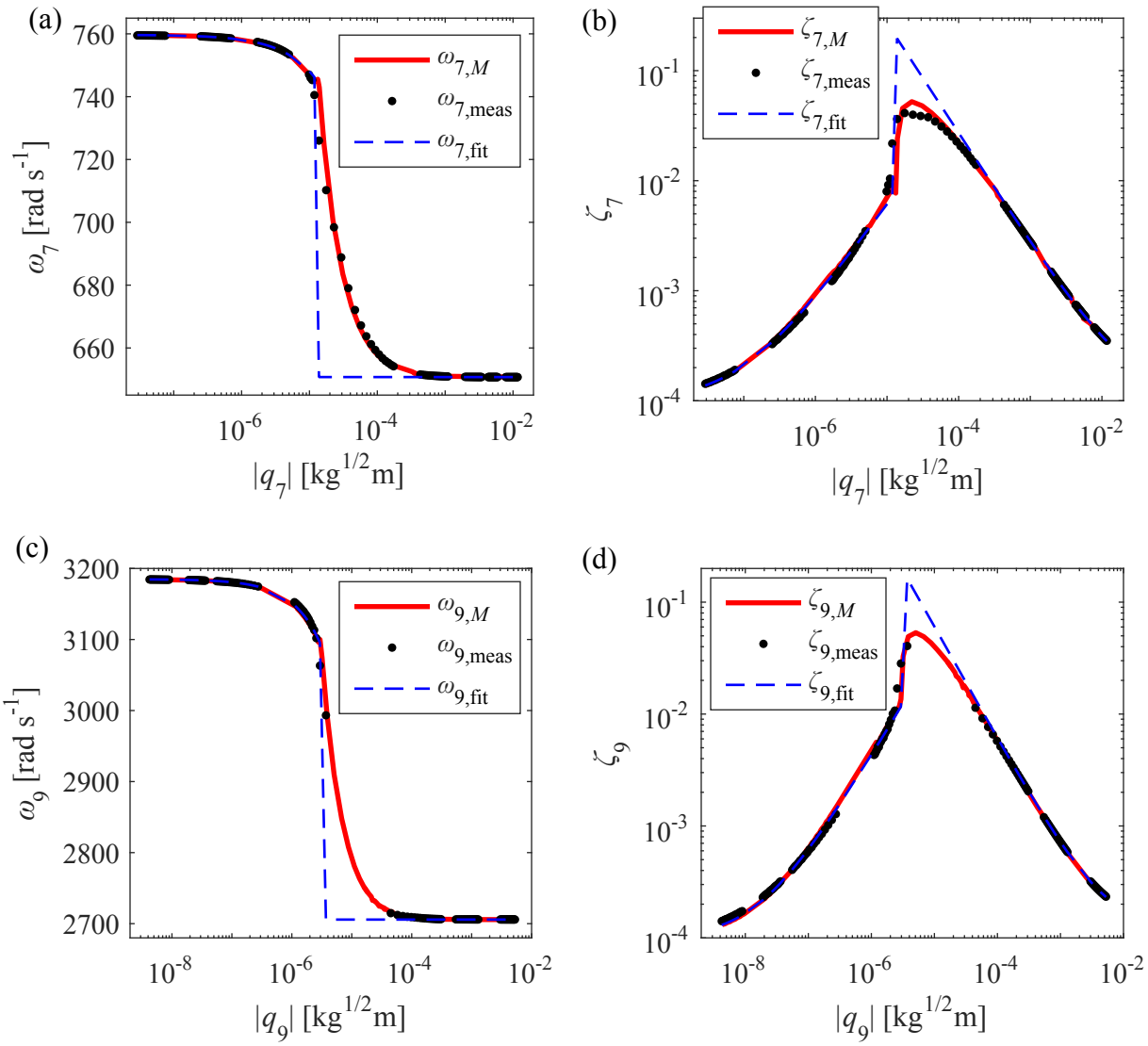

Figure D.1: *(a, c) Natural frequency and (b, d) damping ratio versus modal displacement amplitude for selective excitation of (a, b) mode 7 and (c, d) mode 9 in the Sumali beam system.*

Table D.2: *Parameters for the discrete impulse simulations of the Sumali beam system. The excitation point refers to the location in Fig. 2.9 where the impulse is applied. Scalar p is the force multiplier value input to Eq. (2.29).*

Simulation Number	p [N]	Time Step [s]	Number of Steps	Excitation Point
1	1779	3×10^{-6}	333,333	p_1
2	889.6	3×10^{-6}	333,333	p_1
3	133.5	5×10^{-6}	100,000	p_1
4	8.896	1×10^{-5}	200,000	p_1
5	1.335	1.3×10^{-5}	153,846	p_1
6	0.2669	3×10^{-5}	133,333	p_1
7	0.04448	5×10^{-5}	80,000	p_1
8	0.01335	5×10^{-5}	160,000	p_1
9	3114	5×10^{-6}	200,000	p_2
10	889.6	5×10^{-6}	76,000	p_2
11	133.5	5×10^{-6}	40,000	p_2
12	26.69	5×10^{-6}	100,000	p_2
13	4.448	1×10^{-5}	100,000	p_2
14	1.335	1×10^{-5}	200,000	p_2
15	0.4448	3×10^{-5}	133,333	p_2
16	0.1335	5×10^{-5}	100,000	p_2
17	0.04448	5×10^{-5}	100,000	p_2
18	0.01335	5×10^{-5}	200,000	p_2
19	4003	5×10^{-6}	200,000	p_3
20	1334	5×10^{-6}	100,000	p_3
21	222.4	5×10^{-6}	40,000	p_3
22	22.24	5×10^{-6}	100,000	p_3
23	8.896	1×10^{-5}	100,000	p_3
24	3.559	2×10^{-5}	100,000	p_3
25	0.8896	3×10^{-5}	100,000	p_3
26	0.2224	5×10^{-5}	200,000	p_3

Appendix E

Modal Coupling Checks in QSMA

This appendix shows plots of the natural frequency and damping versus amplitude for selective excitation of the second and third bending modes of Brake-Reuß beam, as computed in the analysis of Section 3.3.3. Figure E.1 compares the second bending modal frequency and damping curves obtained from quasi-static modal analysis (QSMA) with those extracted from the transient ring-down simulations in Section 3.3.2, and Fig. E.2 compares those for the third bending mode. The quasi-static simulation for the second bending mode used $\boldsymbol{\varphi}_3$ for loading and modal filtering, and 50 load steps were computed for α ramping up logarithmically from 10^0 to $10^{3.3}$. The simulation for the third bending mode used $\boldsymbol{\varphi}_7$ and 50 load steps of $\alpha \in [10^1, 10^{3.2}]$ with logarithmic ramp-up.

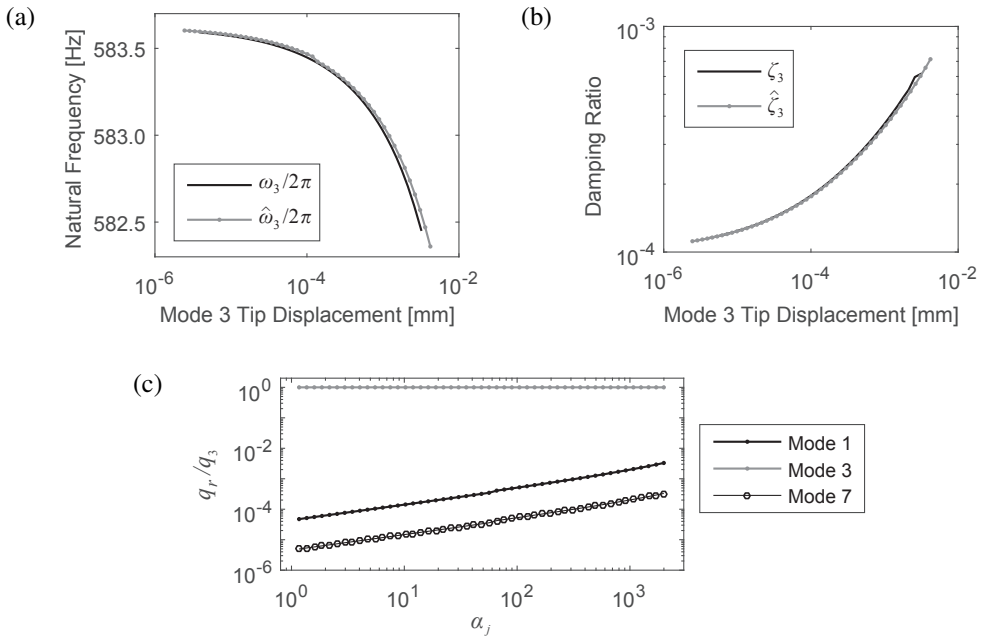

Figure E.1: *Comparison between the ring-down response and QSMA in (a) natural frequency and (b) damping versus displacement amplitude of the right end of the Brake-Reuß beam undergoing second-bending deflection, and (c) the ratio of q_r/q_3 revealing the relative importance of each mode in the quasi-static response.*

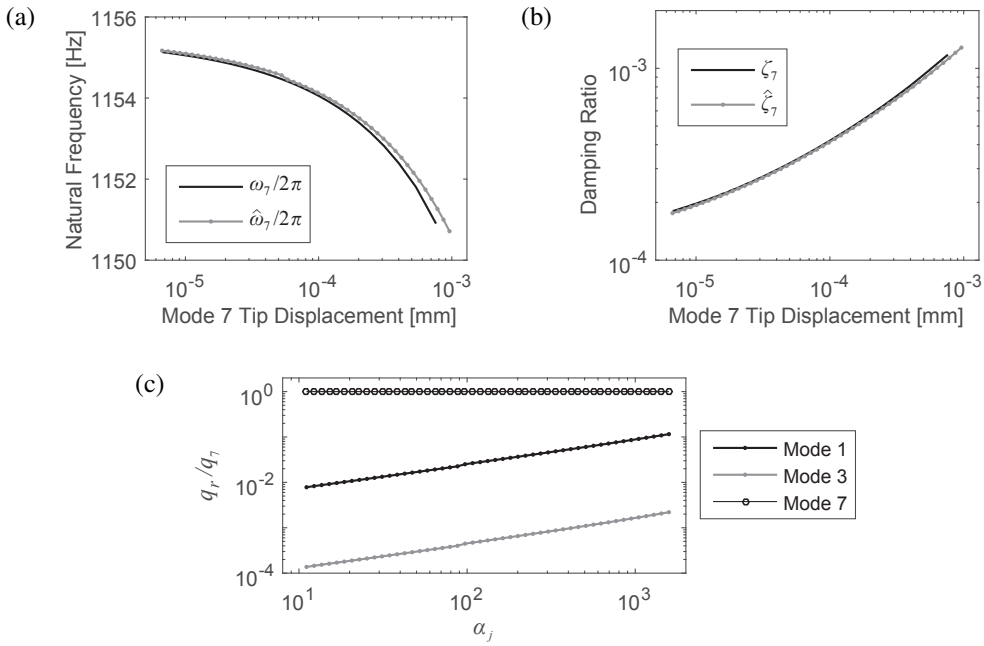

Figure E.2: *Comparison between the ring-down response and QSMA in (a) natural frequency and (b) damping versus displacement amplitude of the right end of the Brake-Reuß beam undergoing third-bending deflection, and (c) the ratio of q_r/q_7 revealing the relative importance of each mode in the quasi-static response.*

Appendix F

Experimental Measurements on the Brake-Reuß Beam

This appendix details the assembly and setup of an experimental Brake-Reuß beam, whose measurements are referenced in Section 3.4.1. The two components, A and B, were identically made with the dimensions given in Fig. F.1. Each component has a material of AISI stainless steel 304, and its interfacing surface was polished to have a surface roughness within 0.8 μm.

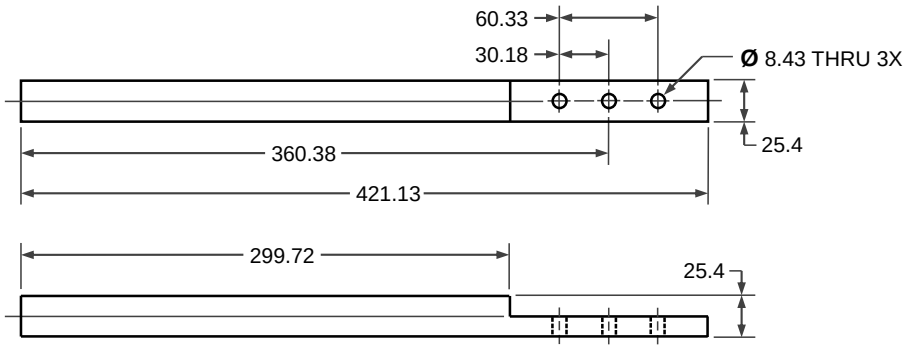

Figure F.1: *Drawing of component A of the Brake-Reuß beam. Components A and B are identical. Length units are in millimeters.*

The two beam components were assembled by lapping the half-height extensions so that their holes aligned. An alignment tool was used to ensure that the outer edges of the two interfacing surfaces remained flush. In addition, a thickness gauge was used to maintain a gap of 0.25 mm between the two half-height surfaces (the vertical surfaces at 299 mm and 421 mm from the left end of the beam) so that these surfaces do not undergo contact during vibration. The interface was bolted using three 5/16-in. diameter, 1.5-in. shaft length SAE grade 8 carbon steel bolt and nut pairs, with two 9/16-in. diameter washers separating the bolt cap and nut each from the beam components. All bolts were oriented so that the bolt caps touch beam

component B. The bolt on the side of component A was tightened first to 14 N-m torque, followed by the tightening of the bolt on the side of component B and then the center bolt to the same torque. All bolts were again tightened in the same order to 27 N-m torque.

The assembled beam was then suspended by a fishing line looped in series with bungee cord, as seen in Fig. F.2. A line was looped a distance of 101 mm from each end of the beam, which were the locations of vibrational nodes for the second bending mode [34]. The beam was rotated so that the bolt axes was aligned parallel to ground. The interface was then made to "settle" by applying 100 N impacts (oriented parallel to the bolt axes) on the ends and the center of the beam using a rubber-tipped hammer.

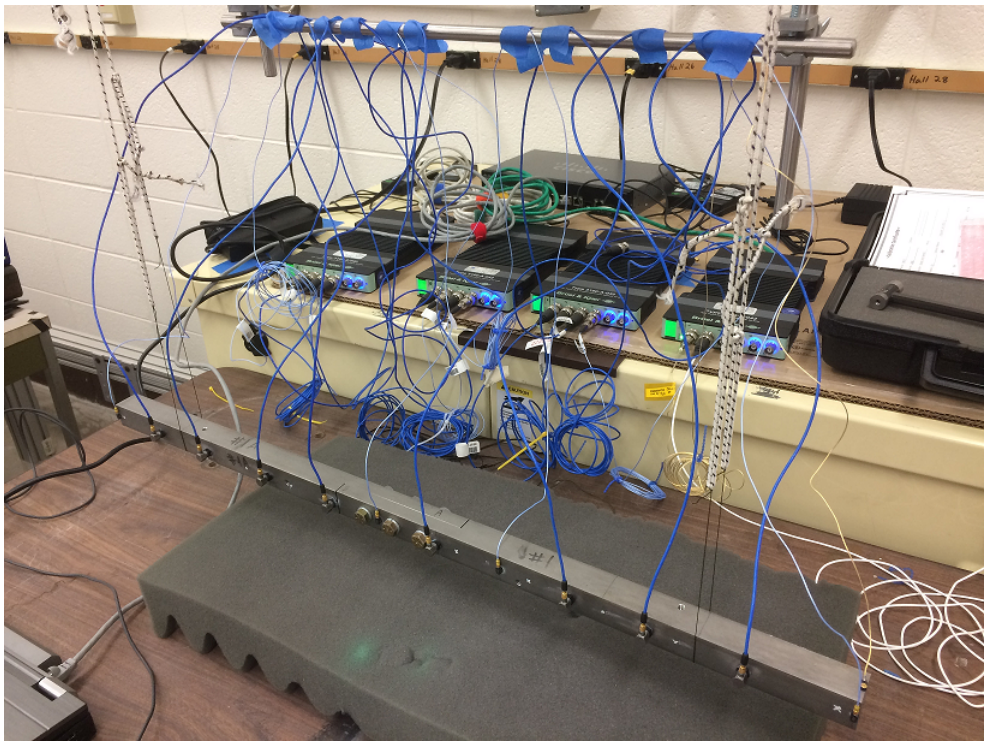

Figure F.2: *A picture of the test setup for the Brake-Reuß beam. The beam component on the left is component A, and component B is on the right.*

The beam was then outfitted with twelve uniaxial PCB accelerometers located along the center axis, as shown in Fig. F.2. These accelerometers measured the response in the y-direction to be consistent with the finite element model shown in Fig. 3.3. The x-position

Table F.1: *Accelerometer model numbers and position on the Brake-Reuß beam relative to the left end of component A.*

Transducer	Position [mm]
PCB 352C23	2.1
PCB 353B15	68.8
PCB 353B11	135.8
PCB 353B15	215.2
PCB 353B15	295.3
PCB 352C23	345.7
PCB 353B11	405.3
PCB 352C23	465.0
PCB 353B15	524.6
PCB 353B11	584.2
PCB 353B11	651.6
PCB 352C23	718.0
Endevco 25B	719.0

of the accelerometers relative to the left edge of beam component A (as viewed in Fig. F.2) are given in Table F.1. A thirteenth uniaxial Endevco accelerometer was placed on the top surface at the right end of the beam to track motion in the lateral (z) direction. This was done to distinguish any modes that were not xy-plane bending. The response at the thirteen accelerometers, and the force from a plastic-tipped PCB 086C01 hammer, were collected through a Brüel & Kjær LAN-XI data acquisition system.

Measuring the low-amplitude mode shapes

The low-amplitude mode shapes of the experimental Brake-Reuß beam were collected first through a series of hammer impact tests. Three such tests were conducted in which the PCB hammer was used to strike point s with an impact having a peak force on the order of 3 N or less. For each strike, the free-response acceleration time histories of the thirteen accelerometers were recorded at a sampling frequency of 16384 Hz for a duration of 8 seconds after impact.

The acceleration and input force signals were then processed to retrieve the frequency response function (FRF). After collecting the time histories, an exponential decay window, with

a time constant of 1.5166 (decay rate for the fundamental mode), was applied on all acceleration signals to minimize the effects of noise. The H1 estimator was then applied on the three impact time histories to estimate the frequency response function [64].

A model of the form of a ratio of polynomials in $i\omega$ was then fitted to the FRF using Allen and Ginsberg's SIMO implementation of the algorithm of mode isolation [67]. Figure F.3 illustrates the composite FRF (average amplitude FRF over all accelerometer points) and its fitted model. Four modes (the first, second, third and fourth bending modes) were clearly identified from the FRF data, though the peak for the fourth bending mode exhibited more noise relative to the other modes. The mode shapes retrieved from these fits are given in Fig. 3.5 in Section 3.4.1.

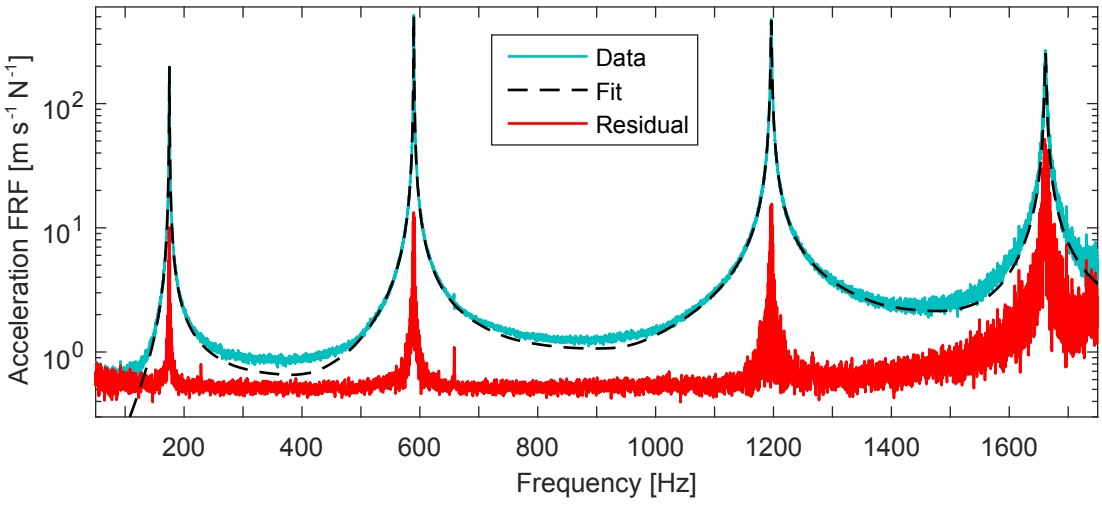

Figure F.3: *Plot of the composite FRF for the low-level hammer impact tests and its fitted model by the algorithm of mode isolation. The residual line shows the composite FRF of the difference between all measured FRFs and their corresponding fitted FRFs.*

High-amplitude impact response tests

After completing the low-amplitude tests, a series of high-amplitude impact tests were conducted to collect the instantaneous modal frequency and damping from the free-response of the Brake-Reuß beam. The PCB rubber-tipped hammer was used to strike the test beam at the

Table F.2: *List of high-level hammer impact tests and their maximum achieved force. Refer to Fig. F.4 for point locations.*

Impact Test #	Point	Max Force [N]
1	p_1	192.3
2	p_1	137.4
3	p_1	171.1
4	p_2	220.0
5	p_2	484.7
6	p_2	398.3
7	p_3	282.3
8	p_3	367.0
9	s	293.6
10	s	251.3
11	s	264.0

point locations illustrated in Fig. F.4. The nodal location for the second bending mode (point p_1) was struck in attempt to excite mostly the first bending mode. Point p_2 is the nodal location for the first bending mode, which was struck in attempt to have the second bending mode dominate the response. Point p_3 (the location of the third accelerometer from the right) was thought to excite mostly the third bending mode since it was located near the nodes for the first and second bending modes and near a peak deflection point for the third bending mode. An impact at point s was meant to excite all bending modes at once. A few impact tests were conducted at each point to verify repeatability. These tests, and their maximum impact force level, are listed in Table F.2. In all tests, the time history from each accelerometer was recorded for a duration of four seconds after impact at a sampling rate of 8192 Hz.

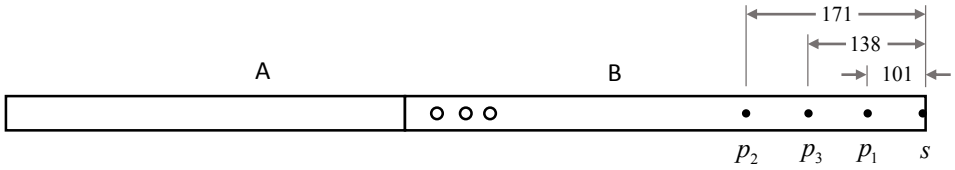

Figure F.4: *Schematic of hammer impact locations, p_1, p_2, p_3, and s, on the Brake-Reuß beam test structure. Length units are mm. Figure is not shown to scale.*

After collecting the time signals, the signals were filtered into their modal components

using the mode shapes acquired from the low-level tests. If $\mathbf{\Phi}$ is defined as the matrix whose columns are the four bending mode shapes, and $\ddot{\mathbf{u}}$ is the physical acceleration vector measured from the accelerometers, then the acceleration signals of the four modes was computed through the left generalized inverse,

$$\ddot{\mathbf{q}} = \left(\mathbf{\Phi}^{\mathrm{T}}\mathbf{\Phi}\right)^{-1}\mathbf{\Phi}^{\mathrm{T}}\ddot{\mathbf{u}}. \tag{F.1}$$

Since the experimental mode shapes were not perfect, each mode had a small contribution from other modes in their signals. Contributions from other signals would distort an amplitude and phase fit from the Hilbert transform method, which only works effectively for signals that contain one dominant frequency. Hence, the four modal signals were passed through a sixth-order Butterworth bandpass filter. Using the frequency response function in Fig. F.3 as a reference, the first bending modal signal was bandpassed between 120 and 220 Hz, second bending between 500 and 700 Hz, third bending between 1150 and 1240 Hz, and fourth bending between 1500 and 1800 Hz. The Hilbert transform method described in Section 3.3.2 was then applied on the four filtered modal signals to retrieve their instantaneous amplitudes, natural frequencies, and damping ratios.

The amplitudes of each test case are plotted versus time in Fig. F.5 to F.8 in order to examine the relative contribution of each mode in the response and to gauge the repeatability of the tests. For impacts at point p_1, Fig. F.5 shows that the first bending mode is the most dominant signal, being one order of magnitude larger than the third bending mode at the beginning of the free response and decaying slowly enough to remain more than two orders of magnitude above the other modal signals at the end of the recorded time history. Figure F.6 shows that, for impacts at point p_2, the second bending mode shares dominance with the third bending mode in the beginning, but then the second bending mode is dominant until the end of the history, where it shares dominance with the first bending mode in tests 4 and 5. The exception is test 6, where it appears that the impact was applied close enough to the first bending nodal point that the first bending modal signal remains at least an order of magnitude less than that of the second

bending mode for all of the recorded history.

In contrast to the excitations at points p_1 and p_2, an impact at point p_3 was not as successful in claiming dominance for the intended target mode: the third bending mode. It can be seen in Fig. F.7 that the first, second, and third bending modes share dominance at the beginning of the history, but because the third bending mode decays rapidly in comparison to the first and second bending modes, the former drops below one order of magnitude less than the latter two after one second passes. Test case 6 was more successful in having the third bending mode remain more dominant than the first bending mode within one second after impact.

A similar outcome occurred for the fourth bending mode. For all test cases, the fourth bending mode received too little energy and decayed far too quickly for it to claim dominance over the first three bending modes. Thus, there was little incentive to consider it as a significant contributer to the nonlinear response of the Brake-Reuß beam in model updating. Hence, the signal for the fourth bending mode was discarded in the updating analysis of Section 3.4. As for the first three bending modes, the method of quasi-static modal analysis helps to fit nonlinear finite element models to data in which the mode under investigation is dominant in the response, so those test cases which most satisfied this criterion were utilized. Specifically, the first bending modal signal from test 2, the second bending signal from test 6, and the third bending signal from test 6 were used for updating in Section 3.4. Afterwards, the four bending modal signals from test 10 were used to validate the updated model against the case when multiple modes are dominant in the experimental response. In Fig. F.8, the amplitude curves for test 10 can be seen to lie in between those curves for Tests 9 and 11, so test 10 was considered an average response for an impact at point s.

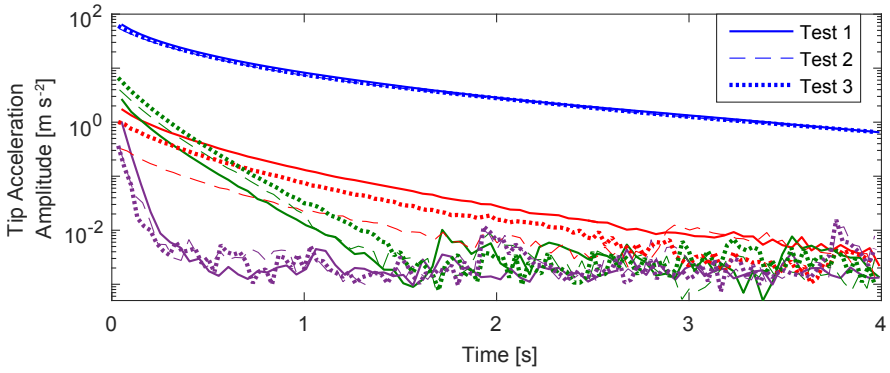

Figure F.5: *Comparison of modal acceleration amplitudes over time in the three tests of an impact force applied at point p_1. The blue lines are the first bending mode, red is second bending, green is third bending, and purple is fourth bending.*

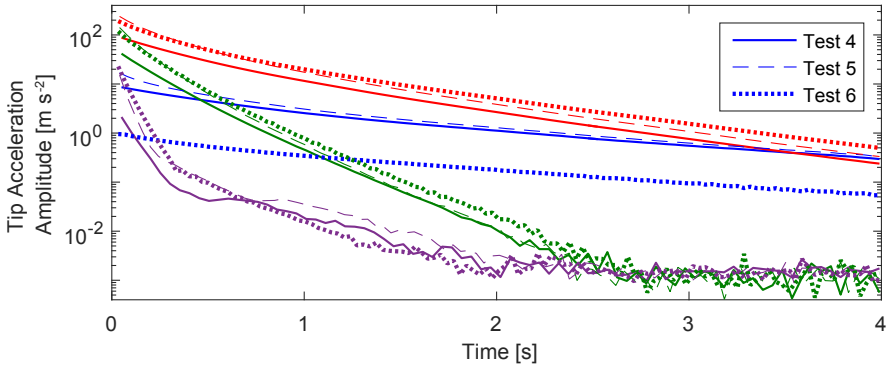

Figure F.6: *Comparison of modal acceleration amplitudes over time in the three tests of an impact force applied at point p_2. The blue lines are the first bending mode, red is second bending, green is third bending, and purple is fourth bending.*

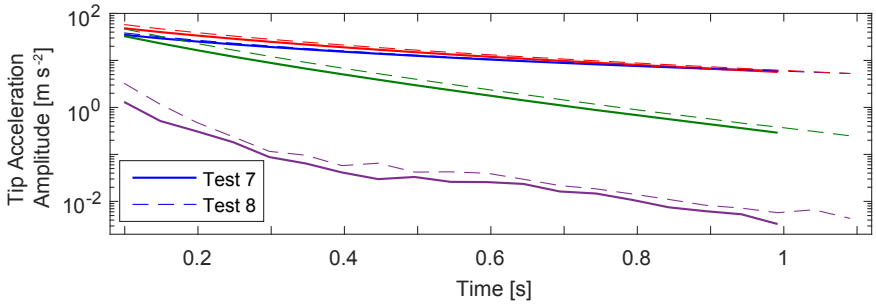

Figure F.7: *Comparison of modal acceleration amplitudes over time in the two tests of an impact force applied at point p_3. The blue lines are the first bending mode, red is second bending, green is third bending, and purple is fourth bending.*

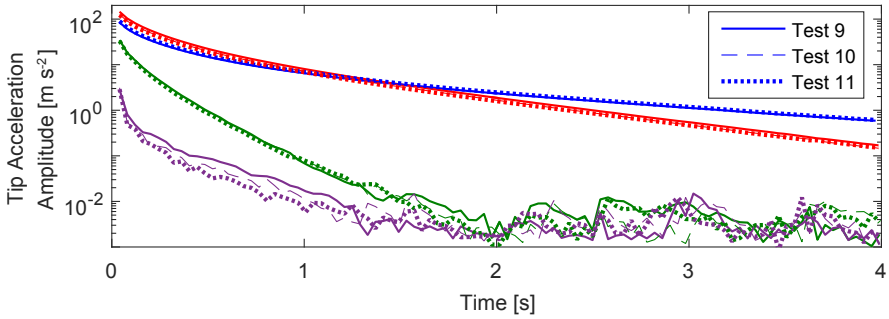

Figure F.8: *Comparison of modal acceleration amplitudes over time in the three tests of an impact force applied at point s. The blue lines are the first bending mode, red is second bending, green is third bending, and purple is fourth bending.*

Appendix G

Verification of the Discrete Five-Parameter Iwan-Type Element with Deflection Tests

The discrete Iwan-type element formulated in Section 4.2.3 was tested against Mignolet's steady-state expressions for stiffness and dissipation to verify that it behaves as expected. For this test, a set of $N = 10000$ Jenkins elements, having uniform intervals in ϕ, was used, with parameters χ=−0.6, $\phi_{\max}$=6×10^{-4}, R=7×10^5, S=9×10^3, and θ=0.3. The Iwan element was subjected to a sinusoid deflection of the same form given by Eq. (4.22) for one and one quarter cycles ($t \in [0, 1.25]$) sampled at step size 0.001. Three different amplitude cases, $u_0 = 1\times10^{-4}$, 3×10^{-4}, and 5×10^{-4}, were examined. The slider states were first initialized to zero, and then Eq. (3.21) ($F_J(t)$) was evaluated at each time step. The resulting force-deflection curves are plotted in Fig. G.1. The first quarter cycle creates an initial loading curve up to u_0, while the remaining full cycle traces the reverse and forward monotonic loading curves of a hysteresis bounded by $\pm u_0$.

The discrete Iwan-type element was verified by comparing the secant slope and area enclosed by the three hysteresis curves shown in Fig. G.1 with those values produced by Mignolet's secant stiffness and energy dissipation expressions. The secant slope, K_{hyst}, was computed as the rise over run between the two tip points of load reversal in the hysteresis, and the area, E_{hyst}, was computed using numerical integration of the difference between the forward and reverse curves. Mignolet's corresponding stiffness and dissipation values were obtained by evaluating Eq. (4.7) and (4.8) appropriately for $u_0 = 2.0$, 3.5, and 5.0 with the given parameter set. The results, listed in Table G.1, show that the three hysteresis curves produce stiffness and

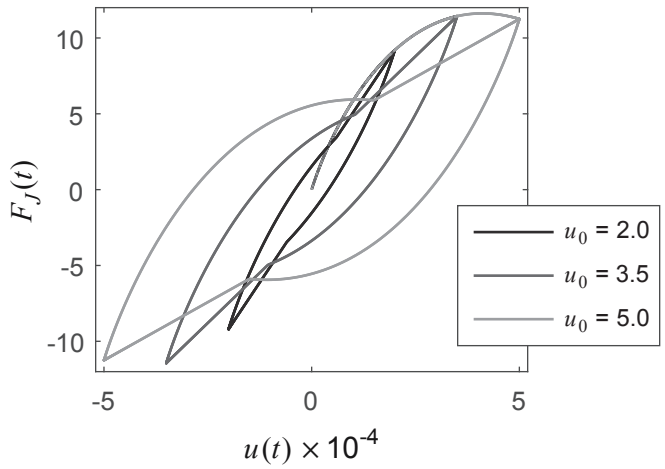

Figure G.1: *Force-deflection curves for the three amplitude cases of sinusoid displacement on the discrete Iwan element.*

dissipation that accurately match those of Mignolet's expressions (within acceptable computational error due to the discretization of both the Iwan element and the time histories).

Table G.1: *Comparison of stiffness and dissipation values between the discrete Iwan element undergoing sinusoidal displacement and Mignolet's closed-from expressions. Percent errors are computed with respect to Mignolet's equations.*

u_0	K_{hyst}	Eq. (4.7)	Error	E_{hyst}	Eq. (B.3)	Error
2.0×10^{-4}	4.598×10^{4}	4.598×10^{4}	0.000%	8.457×10^{-4}	8.457×10^{-4}	-0.001%
3.5×10^{-4}	3.268×10^{4}	3.268×10^{4}	-0.003%	3.240×10^{-4}	3.240×10^{-3}	0.006%
5.0×10^{-4}	2.250×10^{4}	2.250×10^{4}	0.000%	7.627×10^{-4}	7.626×10^{-4}	0.008%

Appendix H

Verification of Equation (4.33)

Equation (4.33) was tested against the force-displacement curve produced by the discrete Iwan element when subjected to a ramp-up loading from $-u_{\max}$ to $u_{\max}$ for $u_{\max} = 5.5 \times 10^{-4}$, $\chi = -0.6$, $\phi_{\max} = 6 \times 10^{-4}$, $R = 7 \times 10^5$, $S = 9 \times 10^3$, and $\theta = 0.3$. Figure H.1 shows that the two curves correlate well with each other.

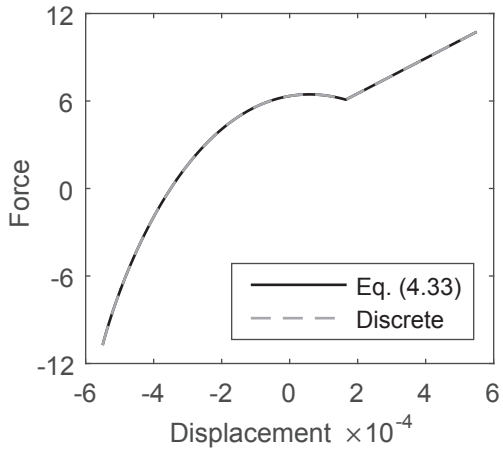

Figure H.1: *Comparison of force-displacement curve produced from the discrete five-parameter Iwan element versus that of Eq. (4.33).*

References

[1] L. Gaul, J. Lenz, Nonlinear dynamics of structures assembled by bolted joints, Acta Mechanica 125 (1) (1997) 169–181.

[2] D. J. Segalman, D. L. Gregory, M. J. Starr, B. R. Resor, M. D. Jew, J. P. Lauffer, N. M. Ames, Handbook on dynamics of jointed structures, Tech. Rep. SAND2009-4164, Sandia National Laboratories, Albuquerque, New Mexico (2009).

[3] C. J. Hartwigsen, Y. Song, D. M. McFarland, L. A. Bergman, A. F. Vakakis, Experimental study of non-linear effects in a typical shear lap joint configuration, Journal of Sound and Vibration 277 (1–2) (2004) 327–351.

[4] E. E. Ungar, The status of engineering knowledge concerning the damping of built-up structures, Journal of Sound and Vibration 26 (1) (1973) 141–154.

[5] A. A. Ferri, Friction damping and isolation systems, Journal of Mechanical Design 117 (1995) 196–206.

[6] L. Gaul, R. Nitsche, The role of friction in mechanical joints, Applied Mechanics Reviews 54 (2) (2001) 93–106.

[7] E. T. Turgut, An analysis of the effect of non-payload weight on fuel consumption for a wide-bodied aircraft, Anadolu University Journal of Science and Technology A – Applied Sciences and Engineering 18 (1) (2017) 59–68.

[8] Air carriers: T-100 domestic segment (u.s. carriers), Tech. rep., Bureau of Transportation Statistics, U.S. DOT, Washington, DC (2017).
URL `https://www.transtats.bts.gov/Oneway.asp`

[9] State energy data system (seds): 2015, Tech. rep., U.S. Energy Information Administration, U.S. DOE, Washington, DC (2016).

[10] B. Bhushan, Concepts and Applications of Tribology, 2nd Edition, Wiley, 2013.

[11] E. J. Berger, Friction modeling for dynamic system simulation, Applied Mechanics Reviews 55 (6) (2002) 535–577.

[12] M. Groper, Microslip and macroslip in bolted joints, Experimental Mechanics 25 (2) (1985) 171–174.

[13] Y. F. Liu, J. Li, Z. M. Zhang, X. H. Hu, W. J. Zhang, Experimental comparison of five friction models on the same test-bed of the micro stick-slip motion system, Mechanical Sciences 6 (1) (2015) 15–28.

[14] E. Pennestri, V. Rossi, P. Salvini, P. P. Valentini, Review and comparison of dry friction force models, Nonlinear Dynamics 83 (4) (2016) 1785–1801.

[15] Y.-H. Sun, T. Chen, C. Q. Wu, C. Shafai, Comparison of four friction models: feature prediction, Journal of Computational and Nonlinear Dynamics 11 (3) (2016) 031009.

[16] C. W. Schwingshackl, D. Di Maio, I. Sever, J. S. Green, Modeling and validation of the nonlinear dynamic behavior of bolted flange joints, Journal of Engineering for Gas Turbines and Power 135 (12) (2013) 122504.

[17] R. E. Goodman, R. L. Taylor, T. L. Brekke, A model for the mechanics of jointed rock, Journal of the Soil Mechanics and Foundations Division 94 (SM3) (1968) 637–659.

[18] V. N. Kaliakin, J. Li, Insight into deficiencies associated with commonly used zero-thickness interface elements, Computers and Geotechnics 17 (2) (1995) 225–252.

[19] D. Süß, K. Willner, Investigation of a jointed friction oscillator using the multiharmonic balance method, Mechanical Systems and Signal Processing 52–53 (2015) 73–87.

[20] C. S. Desai, M. M. Zaman, J. G. Lightner, H. J. Siriwardene, Thin-layer element for interfaces and joints, International Journal for Numerical and Analytical Methods in Geomechanics 8 (1) (1984) 19–43.

[21] M. H. Mayer, L. Gaul, Segment-to-segment contact elements for modelling joint interfaces in finite element analysis, Mechanical Systems and Signal Processing 21 (2) (2007) 724–734.

[22] K. G. Sharma, C. S. Desai, Analysis and implementation of thin-layer element for interfaces and joints, Journal of Engineering Mechanics 118 (12) (1992) 2442–2462.

[23] E. A. Jewell, M. S. Allen, R. Lacayo, Predicting damping of a cantilever beam with a bolted joint using quasi-static modal analysis, in: Proceedings of the ASME 2017 International Design and Engineering Technical Conference & 13th International Conference on Multibody Systems, Nonlinear Dynamics, and Control (IDETC/MSNDC 2017), Cleveland, OH, 2017.

[24] R. R. Craig, A. J. Kurdila, Fundamentals of Structural Dynamics, 2nd Edition, Wiley, Hoboken, NJ, 2006.

[25] E. P. Petrov, D. J. Ewins, Analytical formulation of friction interface elements for analysis of nonlinear multi-harmonic vibrations of bladed disks, Journal of Turbomachinery 125 (2) (2003) 364–371.

[26] S. Bograd, P. Reuss, A. Schmidt, L. Gaul, M. Mayer, Modeling the dynamics of mechanical joints, Mechanical Systems and Signal Processing 25 (8) (2011) 2801–2826.

[27] D. J. Segalman, Modelling joint friction in structural dynamics, Structural Control and Health Monitoring 13 (1) (2006) 430–453.

[28] W. D. Iwan, A distributed-element model for hysteresis and its steady-state dynamic response, Journal of Applied Mechanics 33 (4) (1966) 893–900.

[29] M. Ismail, F. Ikhouane, J. Rodellar, The hysteresis Bouc-Wen model, a survey, Archives of Computational Methods in Engineering 16 (2) (2009) 161–188.

[30] D. J. Segalman, A modal approach to modeling spatially distributed vibration energy dissipation, Tech. Rep. SAND2010-4763, Sandia National Laboratories, Albuquerque, New Mexico (2010).

[31] D. J. Segalman, A four-parameter Iwan model for lap-type joints, Journal of Applied Mechanics 72 (5) (2005) 752–760.

[32] B. J. Deaner, M. S. Allen, M. J. Starr, D. J. Segalman, H. Sumali, Application of viscous and Iwan modal damping models to experimental measurements from bolted structures, Journal of Vibration and Acoustics 137 (2) (2015) 021012.

[33] D. R. Roettgen, M. S. Allen, Nonlinear characterization of a bolted, industrial structure using a modal framework, Mechanical Systems and Signal Processing 84, Part B (2017) 152–170.

[34] D. Roettgen, M. S. Allen, D. Kammer, R. L. Mayes, Substructuring of a nonlinear beam using a modal Iwan framework, part I: nonlinear modal model identification, in: M. Allen, R. Mayes, D. Rixen (Eds.), Dynamics of Coupled Structures 4, Conference Proceedings of the Society of Experimental Mechanics Series, Springer, 2017, pp. 165–178.

[35] M. P. Mignolet, P. Song, X. Q. Wang, A stochastic Iwan-type model for joint behavior variability modeling, Journal of Sound and Vibration 349 (2015) 289–298.

[36] H. Festjens, G. Chevallier, J. L. Dion, A numerical tool for the design of assembled structures under dynamic loads, International Journal of Mechanical Sciences 75 (2013) 170–177.

[37] R. J. Kuether, D. A. Najera, Parameter estimation of joint models using global optimization, Dynamics of Coupled Structures, 4, Conference Proceedings of the Society of Experimental Mechanics Series, Springer, 2017, pp. 29–39.

[38] K. L. Johnson, Contact Mechanics, 4th Edition, Cambridge University Press, Cambridge, United Kingdom, 1985.

[39] D. J. Segalman, An initial overview of Iwan modeling for mechanical joints, Tech. Rep. SAND2001-0811, Sandia National Laboratories, Albuquerque, New Mexico (2001).

[40] M. Feldman, Hilbert transform in vibration analysis, Mechanical Systems and Signal Processing 25 (3) (2011) 735–802.

[41] M. Eriten, M. Kurt, G. Luo, M. McFarland, L. A. Bergman, A. Vakakis, Nonlinear system identification of frictional effects in a beam with a bolted joint connection, Mechanical Systems and Signal Processing 39 (1–2) (2013) 245–264.

[42] H. Festjens, G. Chevallier, J. L. Dion, Nonlinear model order reduction of jointed structures for dynamic analysis, Journal of Sound and Vibration 333 (7) (2014) 2100–2113.

[43] M. Feldman, Non-linear system vibration analysis using Hilbert transform–I. free vibration analysis method "FREEVIB", Mechanical Systems and Signal Processing 8 (2) (1994) 119–127.

[44] H. Sumali, R. A. Kellogg, Calculating damping from ring-down using Hilbert transform and curve fitting, in: 4th International Operational Modal Analysis Conference (IOMAC), Istanbul, Turkey, 2011.

[45] M. S. Allen, H. Sumali, D. S. Epp, Piecewise-linear restoring force surfaces for semi-nonparametric identification of nonlinear systems, Nonlinear Dynamics 54 (1) (2008) 123–135.

[46] R. D. Cook, D. S. Malkus, M. E. Plesha, R. J. Witt, Concepts and Applications of Finite Element Analysis, 4th Edition, John Wiley & Sons, New York, 2002.

[47] Sierra Structural Dynamics Development Team, Sierra structural dynamics–user's notes, Tech. Rep. SAND2015-9132, Sandia National Laboratories, Albuquerque, New Mexico (2015).

[48] R. R. Craig, M. C. C. Bampton, Coupling of substructures for dynamic analyses, AIAA Journal 6 (7) (1968) 1313–1319.

[49] M. R. Brake, The Mechanics of Jointed Structures: Recent Research and Open Challenges for Developing Predictive Models for Structural Dynamics, 1st Edition, Springer, 2018.

[50] Abaqus analysis user's guide, User Manual, Simulia (2014).

[51] H. Jalali, A. Hedayati, H. Ahmadian, Modelling mechanical interfaces experiencing micro-slip/slap, Inverse Problems in Science and Engineering 19 (6) (2011) 751–764.

[52] D. Di Maio, C. Schwingshackl, I. A. Sever, Development of a test planning methodology for performing experimental model validation of bolted flanges, Nonlinear Dynamics 83 (2016) 983–1002.

[53] D. O. Smallwood, D. L. Gregory, R. G. Coleman, Damping investigations of a simplified frictional shear joint, in: 71st Shock and Vibration Symposium, Arlington, Virginia, 2000.

[54] J. Abad, J. M. Franco, R. Celorrio, L. Lezáun, Design of experiments and energy dissipation analysis for a contact mechanics 3d model of frictional bolted lap joints, Advances in Engineering Software 45 (1) (2012) 42–53.

[55] T. Dossogne, T. W. Jerome, D. P. T. Lancereau, S. A. Smith, M. R. W. Brake, B. Pacini, P. Reuß, C. W. Schwingshackl, Experimental assessment of the influence of interface geometries on structural dynamic response, in: M. Allen, R. Mayes, D. Rixen (Eds.), Dynamics of Coupled Structures 4, Conference Proceedings of the Society of Experimental Mechanics Series, Springer, 2017, pp. 255–261.

[56] Y. Song, C. Hartwigsen, D. McFarland, A. Vakakis, L. Bergman, Simulation of dynamics of beam structures with bolted joints using adjusted Iwan beam elements, Journal of Sound and Vibration 273 (2004) 249–276.

[57] R. M. Lacayo, B. J. Deaner, M. S. Allen, A numerical study on the limitations of modal Iwan models for impulsive excitations, Journal of Sound and Vibration 390 (2017) 118–140.

[58] J. Gross, J. Armand, R. M. Lacayo, P. Reuß, L. Salles, C. W. Schwingshackl, M. R. W. Brake, R. J. Kuether, A numerical round robin for the prediction of the dynamics of jointed structures, in: M. Allen, R. Mayes, D. Rixen (Eds.), Dynamics of Coupled Structures 4, Conference Proceedings of the Society of Experimental Mechanics Series, Springer, 2016, pp. 195–211.

[59] W. Chen, X. Deng, Structural damping caused by micro-slip along frictional interfaces, International Journal of Mechanical Sciences 47 (8) (2005) 1191–1211.

[60] J. D. Reid, N. R. Hiser, Detailed modeling of bolted joints with slippage, Finite Elements in Analysis and Design 41 (6) (2005) 547–562.

[61] P. J. Gray, C. T. McCarthy, A global bolted joint model for finite element analysis of load distributions in multi-bolt composite joints, Composites Part B: Engineering 41 (4) (2010) 317–325.

[62] P. Jayakumar, Modeling and identification in structural dynamics, Tech. Rep. EERL 87-01, California Institute of Technology, Pasadena, California (1987).

[63] G. Masing, Eigenspannungen und verfestigung beim messing (self stretching and hardening for brass), in: Proceedings of the Second International Congress for Applied Mechanics, Zurich, Switzerland, 1926, pp. 332–335.

[64] R. Pintelton, J. Schoukens, System Identification: A Frequency Domain Approach, IEEE Press, Piscataway, NJ, 2001.

[65] R. Lacayo, L. Pesaresi, J. Gross, D. Fochler, J. Armand, L. Salles, M. Brake, C. Schwingshackl, Validation and comparison of a time domain approach and a frequency domain approach for nonlinear modeling of structures with bolted joints, submitted to Mechanical Systems and Signal Processing, 2017.

[66] M. S. Allen, R. M. Lacayo, M. R. Brake, Quasi-static modal analysis based on implicit condensation for structures with nonlinear joints, in: ISMA 2016, An International Conference on Noise and Vibration Engineering, Leuven, Belgium, 2016.

[67] M. S. Allen, J. H. Ginsberg, A global, single-input-multi-output (SIMO) implementation of the algorithm of mode isolation and application to analytical and experimental data, Mechanical Systems and Signal Processing 20 (5) (2006) 1090–1111.